2014

A Lab-Scale Experimental Framework for Studying the Phenomenon of Autorotation

Sigitas Rimkus
University of Central Florida

A LAB-SCALE EXPERIMENTAL FRAMEWORK FOR STUDYING THE PHENOMENON OF AUTOROTATION

by

SIGITAS RIMKUS
B.S. Rochester Institute of Technology, 2011

A thesis submitted in partial fulfilment of the requirements
for the degree of Master of Science
in the Department of Mechanical and Aerospace Engineering
in the College of Engineering and Computer Science
at the University of Central Florida
Orlando, Florida

Spring Term
2014

Major Professor: Tuhin Das

ABSTRACT

While wind energy has emerged as a popular source of renewable energy, the traditional wind turbine has an inherent limitation, namely that it only generates power in the presence of sufficiently high and consistent wind speeds. As a result, wind farms are typically built in areas with a high probability of the required wind speeds, which are geographically sparse. One way of overcoming this drawback is to tap into the energy available in winds at high altitudes which are not only consistent and of high magnitude, but also globally pervasive. An airborne wind energy device based upon the phenomenon of autorotation could potentially be used to exploit the abundance of wind of energy present at high altitudes.

The work in this thesis first presents our study of a tethered-airfoil system as a candidate airborne wind energy (AWE) system. A mathematical model was used to show the feasibility of energy capture and the stability of the device in a wind field. Subsequently, the research identified the principle of autorotation to be better suited for high altitude energy harvesting. To this end, the thesis first presents a theoretical basis of the principle of autorotation, which is developed from existing models in literature. The model was adapted to predict aerodynamic conditions when used for harvesting energy. Encouraging simulation results prompted the main emphasis of this thesis, namely design of an experimental framework to corroborate the theory. Several experiments were devised to determine basic performance characteristics of an autogyro rotor and the data from each experiment is presented. A lab-scale experimental setup was developed as part of this thesis. The setup, consisting of a flapping-blade autogyro rotor and sensors, was used to acquire preliminary aerodynamic performance data. It is envisioned that refinements to this setup will ultimately provide a means of directly comparing analytical and experimental data. In this regard, we provide conclusions and make comments on improvements for future experiments.

To my family, my friends, my loved ones, and all those who supported me in this endeavor.

Without your encouragement, love, and support, none of this would have been possible.

ACKNOWLEDGMENTS

The author would like to acknowledge the following undergraduate students of the University of Central Florida's Mechanical and Aerospace Engineering department for their enthusiastic participation in the senior design projects stemming from the research which led to the creation of this thesis: Caleb Campbell, Steven Holz, Kevin Marshall, Nathan People, John-Michael Rouhana, Christopher Vis, Jordan Proulx, Keller Cogswell, Eric Fredrick, and Randall Yant. The author would also like to acknowledge Richard Carrillo of the University of Central Florida's Mechanical and Aerospace Engineering department. His assistance in designing experiments, gathering data, and technical advice is invaluable. Finally, the author would like to thank Tim Windler and the supporting staff of the University of Central Florida machine shop. His expertise and guidance in the manufacturing of various experimental test fixtures used in the research presented within this thesis is greatly appreciated.

TABLE OF CONTENTS

LIST OF FIGURES

LIST OF TABLES

CHAPTER 1: BACKGROUND AND INTRODUCTION

Background on Wind Energy Reserves

With a growing global energy demand and a need to decrease greenhouse gas emissions, renewable energy systems are poised to assume a larger and larger part of energy generation. Consequently, considerable emphasis has been placed on alternative energy technologies and researchers are actively examining new ways of harvesting energy from sources found in nature. Wind energy has experienced the most rapid growth of all the renewable energy sources, though it only accounts for 4% of the renewable energy used in the United States, according to 2007 data [18]. Figure 1.1 shows a map of the wind energy distribution for the United States near the surface [10].

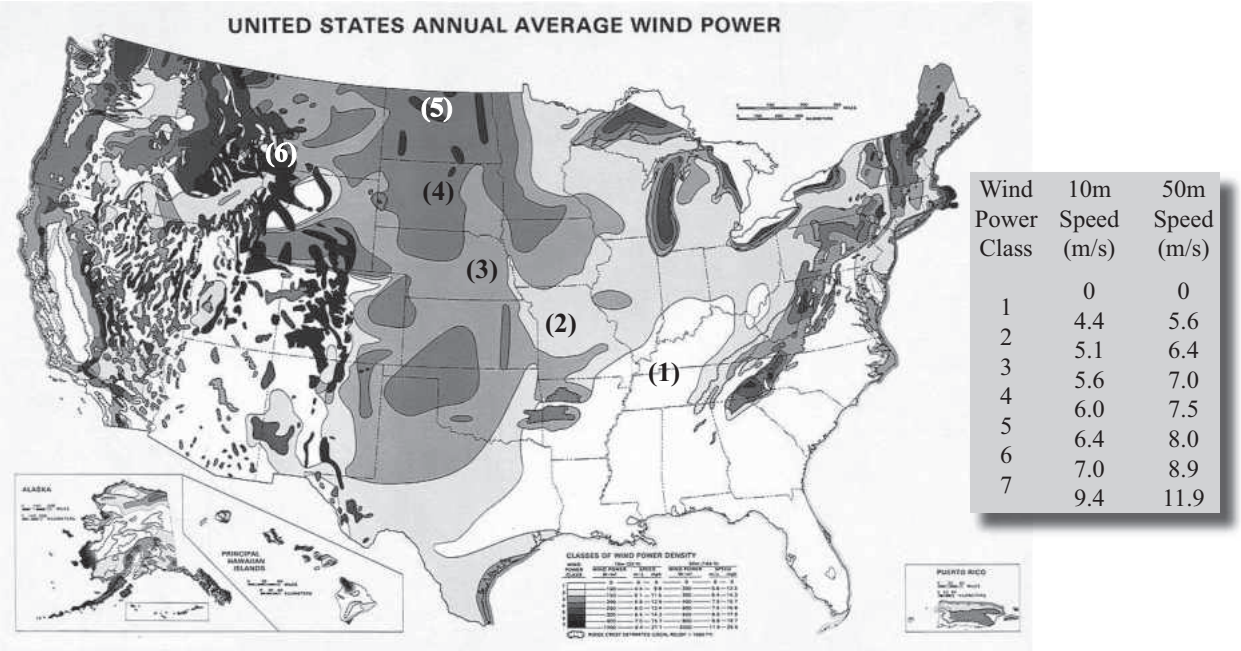

Figure 1.1: United States average annual wind energy distribution map

The majority of wind farms in the United States are built in the higher wind power class zones due to the abundance of relatively high speed winds at these locations. In fact, the three largest (by installed capacity in megawatts) wind farms in the United States, the Alta Wind Energy Center (wind power class 6) in California [34], the Shepherds Flat Wind Farm (wind power class 5) in Oregon [32], and the Roscoe Wind Center (wind power class 3) in Texas [35], are all built in areas where high speed winds are prevalent.

However, Figure 1.1 leaves out important information about the wind at the Earth's surface, namely the ever changing direction and speeds of the wind stream. This variability can be attributed mostly to the local geography and weather patterns. Wind data at higher altitudes paints a much different picture in terms of wind power available and its distribution across the United States. A recent study [4] gave a first glance at the immense amount of wind power available at altitudes of 7-16km. The total wind energy available at these altitudes is estimated to be roughly 100 times that of the global energy demand, and is attributed primarily to the existence of jet streams [38].

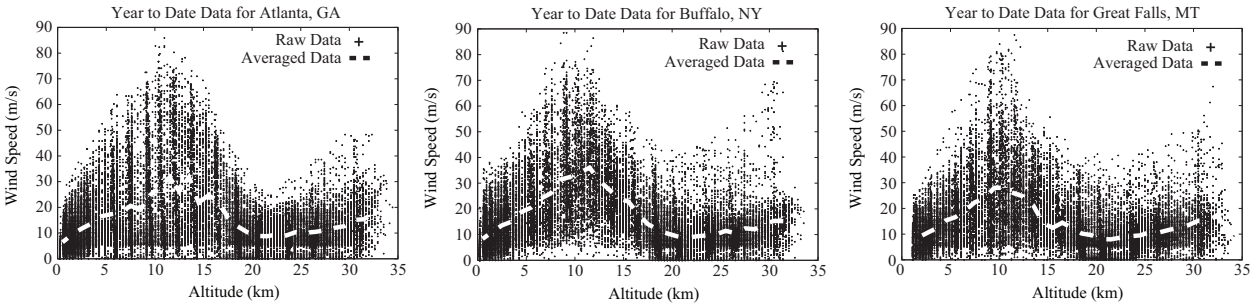

Figure 1.2: Wind speed variation with altitude

The annual wind speed data at higher altitudes is shown for three locations in the United States in Figure 1.2. The data for Figure 1.2 were obtained from the Integrated Global Radiosonde Archive (IGRA) [9]. The locations were chosen such that they covered a wide range of average surface wind speeds. Referring to Figure 1.1, we see that Atlanta, GA is categorized as a wind power

class 1 location, whereas Great Falls, MT is categorized as class 3. Likewise, Buffalo, NY falls in class 4. In contrast to the surface wind speeds shown in Figure 1.1, the data presented in Figure 1.2 shows a wind speed variation with altitude that is similar for the three chosen locations. This prompts us to investigate the viability of exracting wind energy from high altitudes.

Wind Energy Devices

Ground-based wind turbines

The horizontal axis wind turbine (HAWT) is perhaps the most widely used WED. HAWTs are typically deployed in the form of large wind farms [34, 32, 35] in order to take advantage of corridors of high average surface wind speeds. A simplified schematic of a single HAWT and its basic components is shown in Figure 1.3.

The rotor is used to capture energy from the oncoming wind, and the gearbox and generator are used for energy conversion. The nacelle is used primarily to shield the inner workings of the wind turbine from damage. In order to harvest energy from an oncoming wind stream, the wind passes through the rotor disc of the turbine, which induces an aerodynamic torque. This torque is the converted to a rotational energy at the rotor shaft. Typically, since the aerodynamic torque is very large, a gearbox is used in order to reduce the torque at the generator, as well as increase the rotational speed of the generator shaft. After the gearbox, the rotational energy is converted from a mechanical energy to an electrical energy by means of a generator.

However effective HAWTs may be, they are dependent upon the availablility of wind. While wind farms are built predominantly in high wind power class zones, Figure 1.1, due to the transient nature of wind the wind farm could go offline if sufficient wind is not present. This thesis is focused on airborne wind energy and hence we limit our discussions on traditional wind turbines.

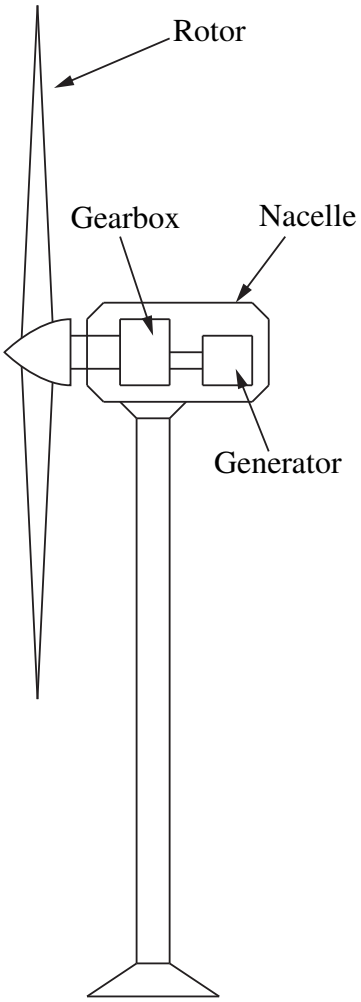

Figure 1.3: A horizontal axis wind turbine

Airborne wind energy devices

Airborne wind energy devices in the form of flying windmills were first proposed in the first half of the 1900s. Originally conceived to power communications aerostats, windmills were placed on the aircraft and were used to generate the power needed to run the onboard communications equipment [27]. Aerostats are typically low to medium altitude aircraft. This is due to two reasons. First, they are primarily used for communications, so their altitude is naturally limited in order to reduce

any loss in communications signal strength as altitude increases. Second, aerostats are generally lightly built, and are held aloft by using a stable, low density gas, such as helium. As altitude increases, the chance of a catastrophic rupture in the skin of the aerostat also increases due to the growing difference in pressure between the inside of the aircraft, where the gas is stored, and the surrounding atmosphere.

Figure 1.4: A modern communications aerostat used for military applications

In contrast to low altitudes, wind energy is more abundant and consistent at higher altitudes, as discussed earlier. However, in order to access higher altitudes, a different aerodynamic platform needs to be used. Tethered airfoils can potentially be used to tap into the energy available in the jet stream. In [37, 8], the authors describe a kite-like tethered airfoil system as shown in Figure 1.5. By "reeling" the kite in and out from a stationary base point O, and adjusting the angle of attack in a particular way, the system can generate useful power. However, with the 10-12km tether lengths needed to reach higher altitudes, a reeling action or a mobile base would subject the system to large time delays and uncertainties between the base and the kite which would in turn result is numerous issues from a control and stability standpoint. Another kite based AWED is Ockels' [30] "Laddermill" concept, a device consisting a long string or loop of kites and a ground-based

generator, as shown in Figure 1.6. The loop of kites would be launched into the air by the lifting force of the kites until is is fully unfurled.

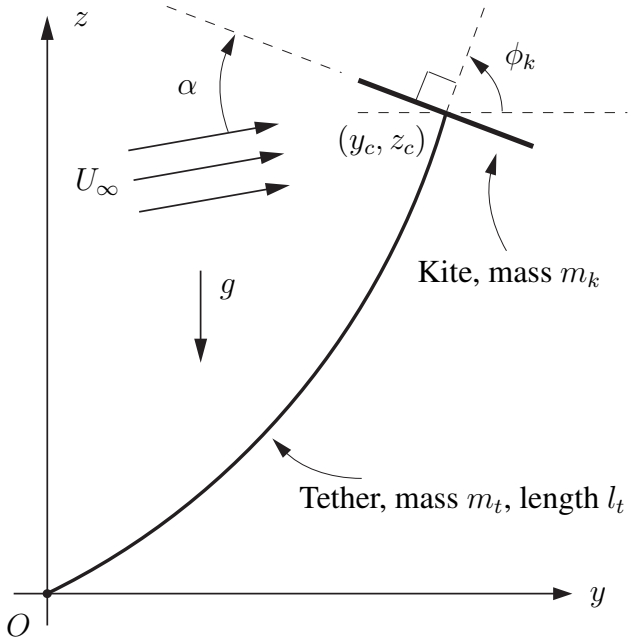

Figure 1.5: A tethered airfoil system

The angles of attack of each individual kite would then be adjusted in such a way that the loop of kites turns a generator on the ground. Current AWED designs are summarized in Table 1.1 [14].

Table 1.1: Categorization of AWEDs

Altitude	**Generator Position**	**Device Weight**	**Aerodynamics**
Low	On ground	Lighter than air (LTA)	Helicopter type
Medium	On board	Higher than air (HTA)	Airfoil type
> 600m			Aerostat type

In all of these categories, most of the recent and ongoing research is essentially in the low and

medium altitude range, typically less than 1km. However, there are obvious advantages of operating at considerably higher altitudes, owing to a better quality wind field.

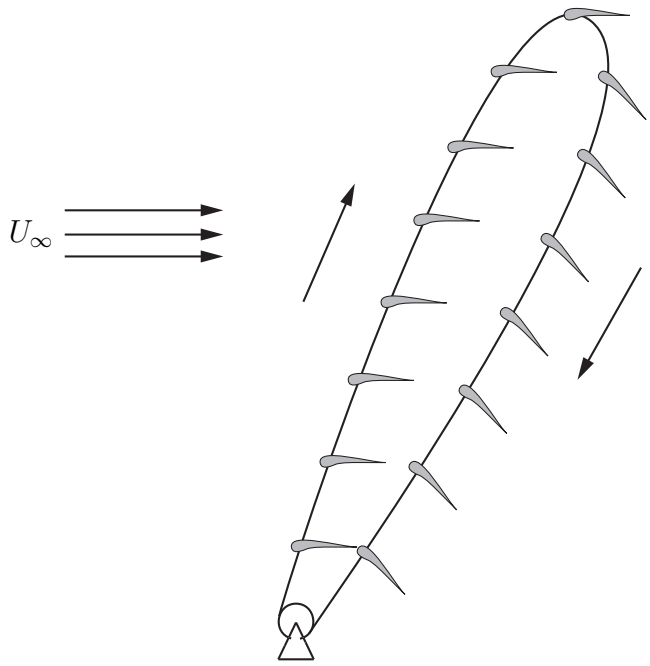

Figure 1.6: The "Laddermill" concept

The concept of a rotorcraft placed permanently in the upper atmosphere was proposed by Fletcher and others [12, 28, 27]. The rotors of the aircraft were designed in such a way that they simultaneously generated sufficient lift to maintain flight as well as electricity. Stability analysis of the proposed system showed the need for an active control system in order to maintain flight. In [38, 36] the authors discussed a power generator based on the concept of the autogyro. In principle, an autogyro, also called a gyroplane, uses an unpowered rotor in a state of autorotation to develop lift. Autorotation is a flight state where the rotor is being turned by oncoming air moving through the rotor disc. In [36] the authors revisted the theory of the autogyro that was first fomally developed in the mid-1920s [17, 25] and then expanded upon in the mid-1940s [40].

The purpose of this work was to lay down a mathematical foundation for using an autogyro for the purposes of energy harvesting.

Motivation

Due to the abundance of pervasive and consistenly high wind speeds in the upper atmosphere, a large amount of energy can be harvested using a suitably designed AWED. Among various AWED designs, an autogyro based AWED looks like a promising framework on which a practical device can be built. The motivation behind using the autogyro principle for energy harvesting is primarily derived from the autogyro rotor being able to spin freely in wind fields and being able to provide a substantial amount of lift and torque. Since wind speeds at high altitudes are very large, an autogyro could potentially generate electricity while the lift is used to support the weight of the complete system. Furthermore, if the configuration of the AWED is properly designed, the hypothetical aircraft could serve a dual purpose in that it could potentially generate power and perform maneuvers. An extended application of an autogyro based AWED could be in UAV technology. Specifically, an increased flight time could be achieved using strong wind fields. Implications of this could include temporary and inexpensive aerial communications networks, as well as loitering surveillance drones.

A concept of such a device is shown in Figure 1.7. The quadrotor design was chosen since many models of its flight dynamics and applicable control algorithms already exist in literature. Therefore, the conversion of an existing quadrotor design to that of an autogyro based AWED in envisioned be relatively simple. However, before considering the technical challenges that come with building such an aircraft, such as airframe design and derivation of the control laws used to maintain flight, it is necessary to first explore the aerodynamic properties of the autogyro rotor itself. It is the aim of the research presented in this thesis to establish a foundation of analytical and exper-

imental knowledge pertaining to the autogyro's aerodynamic properties, as well as to establish a direction for future experimentation and development.

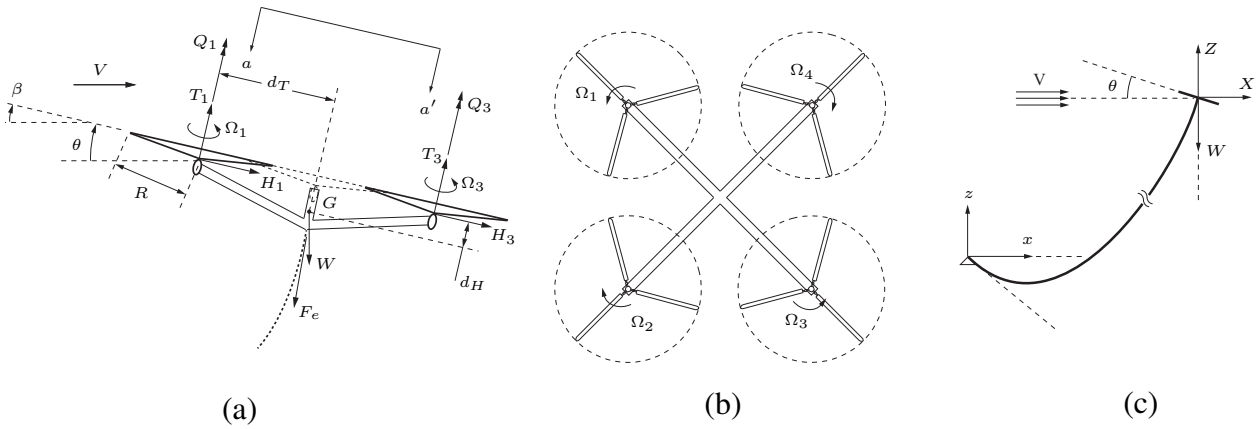

Figure 1.7: Concept of an autogyro-based quadrotor for energy harvesting: (a) forces on a tethered autogyro quadrotor, (b) view of the quadrotor from plan aa', (c) global view of a simplified autogyro-based AWED

Document outline

This document is divided into three main components: (1) a theoretical background, which discusses the theory behind the tethered airfoil and the autogyro, (2) the experimental methodology and results, and (3) the conclusions. Additionally, there is an extensive appendix containing the MATLAB code used in data processing and nomenclature used in the theoretical development of this work.

We start out by discussing prior work which has led to the formation of the research presented within this thesis. With respect to theoretical background, we present work on tethered airfoil to extract energy from wind. Specifically, we discuss the stability of such a system. Next, we present the theoretical basis for using an autogyro based AWED.

The theoretical background leading up to the primary content of this work encompass chapters 2 and 3. In chapters 4 and 5, we present the experimental aspect of this work. First, the theoretical and practical basis, along with the motivation for each experiment performed, are presented. This chapter not only outlines certain considerations taken in the design of each experiment, but also provides detailed experimental procedures for each experiment performed with references to any MATLAB code used (code is available in Appendix A). The subsequent chapter presents the experimental data gathered from each experiment and provides comments on each. Space permitting, the experimental data is also presented in the text for clarity and ease of interpretation.

The final chapter is devoted to concluding remarks. In this chapter, we summarize the results obtained and make connections to results which exist in literature. Furthermore, we presented comments and possible future avenues for experimentation and research on the autogyro based AWED problem.

CHAPTER 2: NON-TRADITIONAL WEDs: THE TETHERED AIRFOIL SYSTEM

Introduction

Due to their potential advantages, many airborne wind energy device designs have been proposed. Machines like Ockels' "Laddermill" [31] and tether-airfoil design discussed in [44] have been described in literature. A small-scale test of a tethered airfoil system was described by Canale et al. [5] that further validated the theory with experimental data. Work by Loyd [26] found that a kite of comparable size to a large airliner could produce more than 3 MW of power in a 10 m/s wind, a figure similar to that produced by a large wind turbine.

In [7], a simple model of a two-dimensional tether-airfoil system mounted on a base capable of linear horizontal motion was presented. By oscillating the base in a particular manner and changing the angle of attack synchronously, useful power was generated. The authors also briefly presented an empirical method of determining the stability of the tether-airfoil system. By injecting small perturbations into the system in the form of step changes in wind velocity and intial conditions, the authors were able to show that the system tajectories converged to equilibrium. We present a brief overview of this prior work and describe a stability problem that was studied as part of this thesis research.

With the objective of analyzing the stability of a tethered airfoil in a wind field, we consider two cases, a straight tether case, and a catenary tether case. The straight tether case is a good approximation of the tether shape for small tether lengths and high wind speed operating conditions where aerodynamic forces acting on the airfoil result in large tension forces in the tether. The catenary case is more realistic and is valid for lesser wind speeds. We first provide an overview outlining

various assumptions and general aerodynamic equations which will allow for the derivation of the equations of motion for the straight tether and catenary geometry. Next, we derive the equations of motion and linearize them about the equilibrium point. Then, we provide the results of several simulations. Finally, we make concluding remarks.

System Description and Model Development

Assumptions

We assume a tether-airfoil system as shown in Figure2.1. For modeling the system, we make the following assumptions:

A1. The tether-airfoil system moves entirely within the yz-plane.

A2. The airfoil is a square, flat plate, and its instantaneous angle of attack α is sufficiently small that the the foil is not in a stalled condition.

A3. The tether is negligibly thin, inextensible, and is not subject to aerodynamic loads.

A4. The velocity of the oncoming wind has time-steady magnitude and direction.

A5. A control system is used to maintain a constant inclination ϕ_k of the airfoil, i.e. $\dot{\phi}_k = 0$.

A6. The tether is connected to a stationary base O.

Dynamic model: Lagrangian formulation

In this section, a mathematical model of the tether-airfoil system, shown in Figure 2.2, is derived. A discretized tether with $n + 1$ tether elements is modeled.

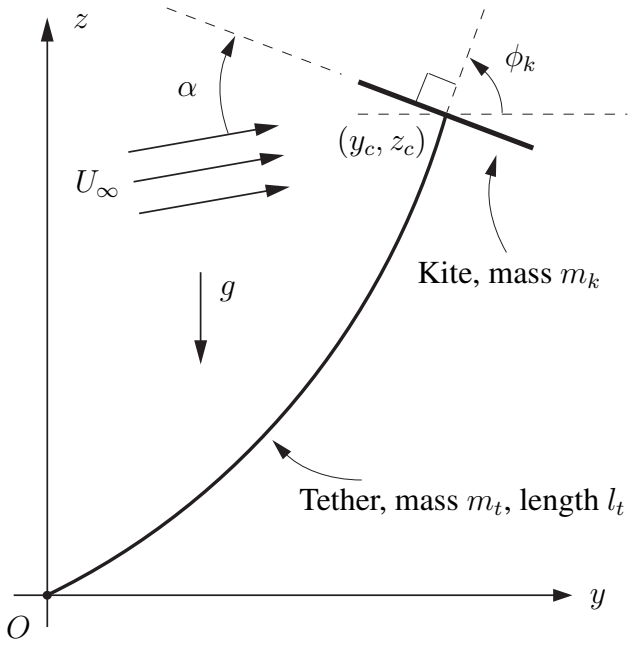

Figure 2.1: Schematic of tether-airfoil system

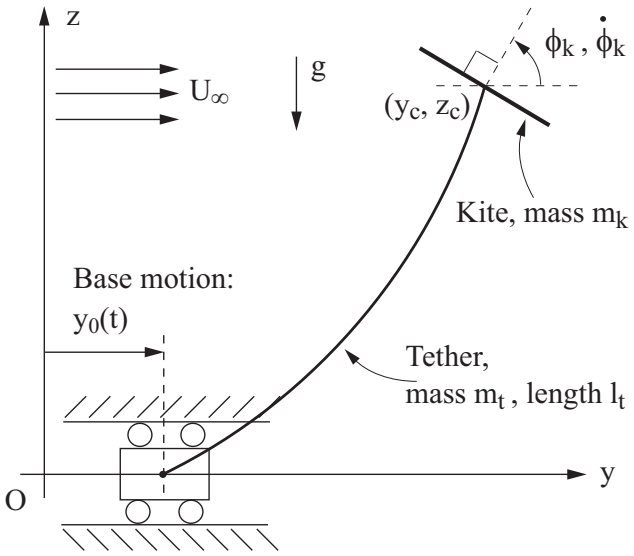

Figure 2.2: Schematic of tether-airfoil system

A single tether element is shown in Figure 2.3. Each element of the tether has a length $l_e = l_t/(n+1)$. The first n point masses having mass $m_e = m_t/(n+1)$ and the $(n+1)^{\text{th}}$ point mass has a mass of $m_{n+1} = m_e + m_k$. Consider a single, discrete tether element as shown in Figure 2.3.

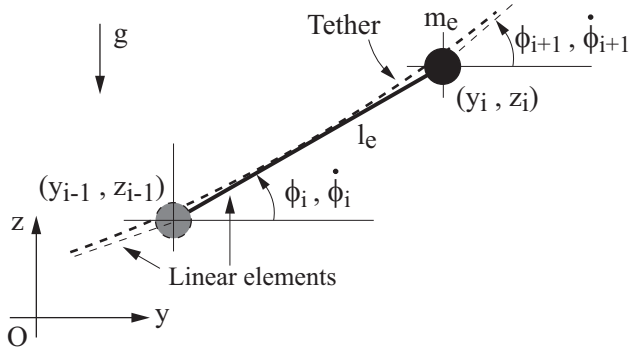

Figure 2.3: Spatial orientation of a single tether element

The position of the i^{th} point mass relative to the absolute co-ordinate axes can be written as

$$y_i = l_e \sum_{j=1}^{i} \cos\phi_j + y_0, \quad z_i = l_e \sum_{j=1}^{i} \sin\phi_j \qquad i = 1, 2, \ldots, (n+1) \tag{2.1}$$

from which the velocity equations follow directly as

$$\dot{y}_i = -l_e \sum_{j=1}^{i} \dot{\phi}_j \sin\phi_j + \dot{y}_0, \quad \dot{z}_i = l_e \sum_{j=1}^{i} \dot{\phi}_j \cos\phi_j \qquad i = 1, 2, \ldots, (n+1) \tag{2.2}$$

Define $\phi_i, \;\; i = 1, 2, \ldots, (n+1)$, y_0 and ϕ_k as the generalized co-ordinates for deriving the equations of motion. Also define the Lagrangian $\mathcal{L} = T - V$. Then, the Lagrange's equation for the

generalized co-ordinate ϕ_i is written as

$$\frac{d}{dt}\left(\frac{\partial \mathcal{L}}{\partial \dot{\phi}_i}\right) - \frac{\partial \mathcal{L}}{\partial \phi_i} = \tau_i, \quad i = 1, 2, \ldots, (n+1) \tag{2.3}$$

while that for the generalized co-ordinates y_0 and ϕ_k are

$$\frac{d}{dt}\left(\frac{\partial \mathcal{L}}{\partial \dot{y}_0}\right) - \frac{\partial \mathcal{L}}{\partial y_0} = F_b, \quad \frac{d}{dt}\left(\frac{\partial \mathcal{L}}{\partial \dot{\phi}_k}\right) - \frac{\partial \mathcal{L}}{\partial \phi_k} = \tau_k \tag{2.4}$$

The net kinetic energy of the tether-airfoil system is

$$T = \frac{1}{2} m_e \left[\sum\nolimits_{i=1}^{n} (\dot{y}_i^2 + \dot{z}_i^2) \right] + \frac{1}{2} m_{n+1} \left(\dot{y}_{n+1}^2 + \dot{z}_{n+1}^2 \right) + \frac{1}{2} I \dot{\phi}_k^2 \tag{2.5}$$

where $\dot{y}_i$ and $\dot{z}_i$ are defined in Eq. (2.2). Similarly the net potential energy of the tether-airfoil system is

$$V = m_e g \sum\nolimits_{i=1}^{n} z_i + m_{n+1}\, g\, z_{n+1} \tag{2.6}$$

where z_i is defined in Eq. (2.1). From Eqs. (2.3), (2.5) and (2.6), we have the following equation of motion of the generalized co-ordinates ϕ_i

$$\begin{aligned}
& m_e l_e^2 (n-i+1) \sum\nolimits_{j=1}^{i} \sin(\phi_i - \phi_j) \dot{\phi}_j^2 + m_e l_e^2 \sum\nolimits_{j=i+1}^{n} \left[\sin(\phi_i - \phi_j) \dot{\phi}_j^2 (n-j+1) \right] \\
& + m_e l_e^2 (n-i+1) \sum\nolimits_{j=1}^{i} \cos(\phi_i - \phi_j) \ddot{\phi}_j + m_e l_e^2 \sum\nolimits_{j=i+1}^{n} \left[\cos(\phi_i - \phi_j) \ddot{\phi}_j (n-j+1) \right] \\
& + (m_e + m_k) l_e^2 \sum\nolimits_{j=1}^{n+1} \cos(\phi_i - \phi_j) \ddot{\phi}_j + (m_e + m_k) l_e^2 \sum\nolimits_{j=1}^{n+1} \sin(\phi_i - \phi_j) \dot{\phi}_j^2 \\
& + m_e g l_e (n-i+1) \cos\phi_i + (m_e + m_k) g l_e \cos\phi_i \\
& - l_e \sin\phi_i \ddot{y}_0 \left[m_e (n-i+1) + m_e + m_k \right] = \tau_i \\
& \quad i = 1, 2, \ldots, (n+1)
\end{aligned} \tag{2.7}$$

Additionally, we have from Eq. (2.4), (2.5) and (2.6), the following equations of motion of the generalized co-ordinates y_0 and ϕ_k

$$\begin{aligned} m_e \sum_{i=1}^{n} \ddot{y}_i + (m_e + m_k)\, \ddot{y}_{n+1} + [m_e(n+1) + m_k]\, \ddot{y}_0 = F_b, \\ I\ddot{\phi}_k = \tau_k \end{aligned} \tag{2.8}$$

Next, in order to determine the generalized torques τ_i, τ_k and the generalized force F_b, we apply the *Principle of Virtual Work* [29]. First, the external non-potential forces and torques are identified from free-body diagrams of the airfoil and the base shown in Figsures 2.5 and 2.4. The non-potential forces and torques are L, D, F_a, M_a, F_r and F_t.

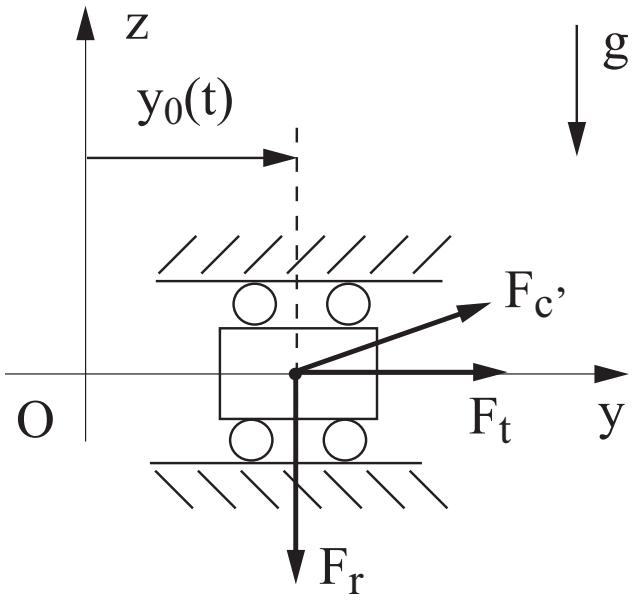

Figure 2.4: Free-body diagram of the base

Defining force $\vec{F}$ as

$$\vec{F} = (D\cos\beta - L\sin\beta)\,\hat{j} + (D\sin\beta + L\cos\beta)\,\hat{k} \tag{2.9}$$

we can write the following expression of virtual work done by non-potential forces and torques

$$\delta W = \vec{F} \cdot \left(\delta y_c \, \hat{j} + \delta z_c \, \hat{k} \right) + F_t \, \delta y_0 + (2F_a d - M_a) \, \delta \phi_k \tag{2.10}$$

where, from Eq. (2.1),

$$y_c = l_e \sum_{j=1}^{n+1} \cos \phi_j + y_0, \quad z_c = l_e \sum_{j=1}^{n+1} \sin \phi_j. \tag{2.11}$$

The virtual displacements δy_c and δz_c are expressed in terms of virtual displacements of generalized coordinates using Eq. (2.1), as follows

$$\delta y_c = -l_e \sum_{i=1}^{n+1} \sin \phi_i \delta \phi_i + \delta y_0, \quad \delta z_c = l_e \sum_{i=1}^{n+1} \cos \phi_i \delta \phi_i \tag{2.12}$$

Carrying out the dot product in Eq. (2.10) and extracting the co-efficient of $\delta \phi_i$, we get the following expression for τ_i

$$\tau_i = -l_e [(D \cos \beta - L \sin \beta) \, \sin \phi_i - (D \sin \beta + L \cos \beta) \, \cos \phi_i] \tag{2.13}$$

Similarly, since the generalized force F_b is associated with the generalized coordinate y_0, extracting the coefficient of δy_0 from Eq. (2.10), we have

$$F_b = D \cos \beta - L \sin \beta + F_t \tag{2.14}$$

Finally, the generalized torque τ_k of Eq. (2.8) is obtained by extracting the coefficient of $\delta \phi_k$

$$\tau_k = 2F_a d - M_a \tag{2.15}$$

It is worth noting here that the cable tension is not included in the calculation of the generalized

forces and torques since it is an internal force for the tether airfoil system. Eqs. (2.7), (2.8), (2.13), (2.14) and (2.15), the equation of motion of the tether-airfoil model is completely defined.

Forces on the airfoil: lift and drag formulation

A free body diagram of the airfoil is shown in Figure 2.5. For the sake of conciseness, the net moment on the airfoil due to external forces is not shown since it assumed that $\dot{\phi}_k = 0$ through an active control, assumption A5.

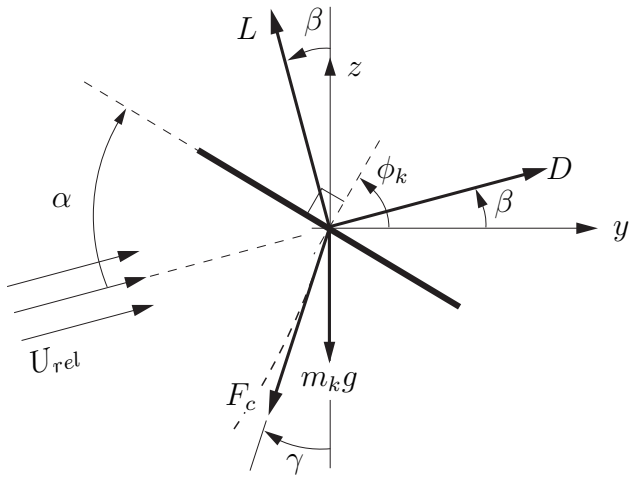

Figure 2.5: Free-body diagram of airfoil

The lift and drag forces acting on the airfoil are

$$L = \frac{1}{2}\rho C_L A||\vec{U}_{rel}||^2, \quad D = \frac{1}{2}\rho C_L A||\vec{U}_{rel}||^2 \tag{2.16}$$

where

$$||\vec{U}_{rel}||^2 = U_{rel,y}^2 + U_{rel,z}^2, \quad \tan\beta = U_{rel,z}/U_{rel,y}$$

The calculation of C_L and C_D are described in detail in [7], which are based on *thin airfoil theory* discussed in [2, 3]. The lift coefficient is modeled as

$$C_L(\alpha) = \frac{dC_L}{d\alpha}(\alpha - \alpha_{L,0}),\ \frac{dC_L}{d\alpha} = \frac{2\pi}{1 + \frac{2}{\epsilon AR}},\ AR = \frac{b^2}{s} \tag{2.17}$$

where ϵ is obtained from experimental data, and with typical values in the range $0.8 \leq \epsilon \leq 1$. The drag coefficients is modeled as

$$C_D = C_d(\alpha) + \frac{C_L^2(\alpha)}{\pi \epsilon AR} \tag{2.18}$$

Stability Analysis

Location of static equilibrium point

At static equilibrium, the forces on the tether are shown in Figure 2.6.

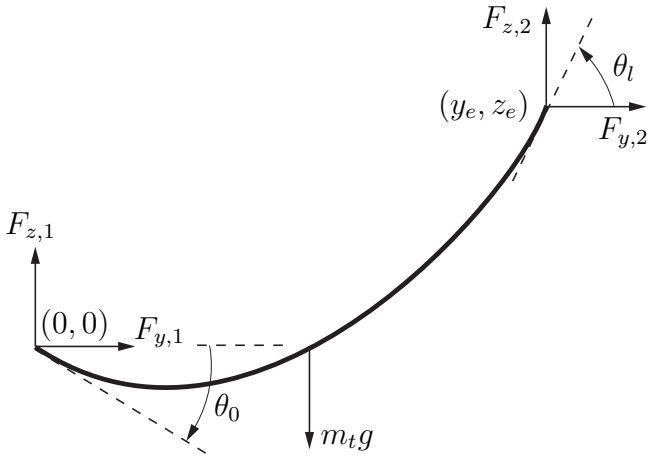

Figure 2.6: Tether with forces at equilibrium

From Figures 2.5 and 2.6, and using subscript e to represent equilibrium condition, we have

$$D_e \cos\beta_e - L_e \sin\beta_e = F_{y,2} \tag{2.19}$$

$$D_e \sin\beta_e + L_e \sin\beta_e - m_k g = F_{z,2}. \tag{2.20}$$

where (y_e, z_e) is the static equilibrium position of the center of mass of the airfoil. From force balance at equilibrium configuration of the tether, we obtain

$$F_{y,1} = -F_{y,2}, \quad F_{z,1} = m_t g - F_{z,2} \tag{2.21}$$

At equilibrium, the tether takes the shape of a *catenary*, with equation

$$z = a\cosh\left(\frac{y-q}{a}\right) + h \tag{2.22}$$

where h, q and a are constant parameters of the catenary. The length of the tether is constant and from Eq.(2.22)

$$\begin{aligned} l_t &= \int_0^{y_e} \sqrt{1+\left(\tfrac{dz}{dy}\right)^2}\, dy \\ &= a\left(\sinh\left(\tfrac{y_e-q}{a}\right) - \sinh\left(-\tfrac{q}{a}\right)\right). \end{aligned} \tag{2.23}$$

We also note in Figure2.6, that the tension at any point of the catenary is directed tangential to the catenary. Hence,

$$\begin{aligned} -\tfrac{dz}{dy}|_{(0,0)} = \tan\theta_0 &= \sinh\left(-\tfrac{q}{a}\right) = \tfrac{-F_{z,1}}{F_{y,1}} \\ \tfrac{dz}{dy}|_{(y_e,z_e)} = \tan\theta_l &= \sinh\left(\tfrac{y_e-q}{a}\right) = \tfrac{F_{z,2}}{F_{y,2}} \end{aligned} \tag{2.24}$$

Noting that L_e and D_e can be calculated for a steady operating condition and noting that $\tan\beta_e = U_{\infty,z}/U_{\infty,z}$, the above equations can be solved to calculate the static equilibrium position (y_e, z_e).

Stability analysis with straight tether assumption

The straight tether assumption can be valid at high wind speeds when the tether tension is high. We apply this assumption to derive simple analytical conditions for stability. The assumption also reduces the tether-airfoil to a 1DOF system.

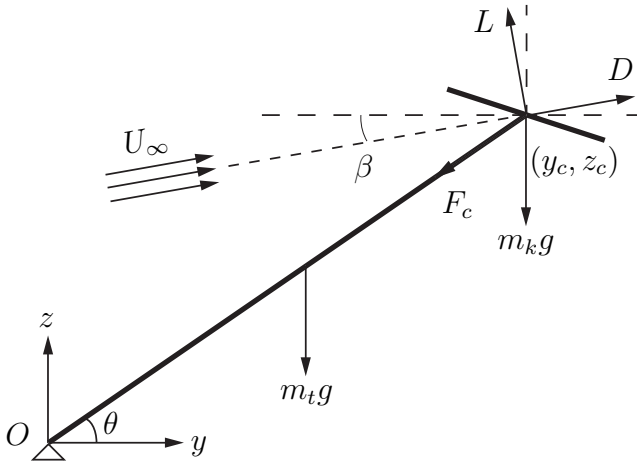

Figure 2.7: Straight tether-airfoil with external forces

For a straight tether, $y_c = l_t \cos\theta$ and $z_c = l_t \sin\theta$, and the equation of motion in θ can be written as

$$I_O\ddot{\theta} = l_t L\cos(\theta-\beta) - l_t D\sin(\theta-\beta) \tag{2.25}$$

$$- \left(m_k + \frac{m_t}{2}\right) g l_t \cos\theta,\; I_O = \left(\frac{1}{3}m_t + m_k\right) l_t^2 \tag{2.26}$$

The formulations of the lift force L and drag force D are

$$L = \frac{1}{2}\rho C_L A\left[2U_\infty^2 + 2U_\infty l_t\dot{\theta}(\sin\theta - \cos\theta) + l_t^2\dot{\theta}^2\right]$$

$$D = \frac{1}{2}\rho C_D A\left[2U_\infty^2 + 2U_\infty l_t\dot{\theta}(\sin\theta - \cos\theta) + l_t^2\dot{\theta}^2\right] \tag{2.27}$$

respectively, where β is

$$\beta = \arctan\left(\frac{U_{\infty,z} - \dot{z}}{U_{\infty,y} - \dot{y}}\right) = \arctan\left(\frac{U_{\infty,z} - l_t\dot{\theta}\cos\theta}{U_{\infty,y} + l_t\dot{\theta}\sin\theta}\right) \tag{2.28}$$

In order to investigate the stability of the static equilibrium, we linearize Eq.(2.26) about the equilibrium angle θ_e

$$I_O\ddot{\delta} = f(\theta_e, 0) + \left.\frac{\partial f}{\partial\theta}\right|_{\theta_e,0}\delta + \left.\frac{\partial f}{\partial\dot{\theta}}\right|_{\theta_e,0}\dot{\delta} \tag{2.29}$$

where $\delta = \theta - \theta_e$, and $f(\theta_e, \dot{\theta_e})$ is the right-hand side of Eq.(2.26). Carrying out the derivatives and grouping like terms yields the linearized equation of motion

$$I_O\ddot{\delta} + c\dot{\delta} + k\delta = 0 \tag{2.30}$$

where

$$\begin{aligned} c = &\left[\frac{1}{2}\rho A l_t^2 C_D U_\infty \left(1 + \sin^2(\theta_e - \beta_e)\right)\right. \\ &\left.-\frac{1}{2}\rho A l_t^2 C_L U_\infty \cos(\theta_e - \beta_e)\sin(\theta_e - \beta_e)\right] \end{aligned} \tag{2.31}$$

$$\begin{aligned} k = &\left[\frac{1}{2}\rho A l_t C_D U_\infty^2 \cos(\theta_e - \beta_e) - \left(m_k + \frac{m_t}{2}\right) g l_t \sin\theta_e\right. \\ &\left.-\frac{1}{2}\rho A l_t C_L U_\infty^2 \sin(\theta_e - \beta_e)\right] \end{aligned} \tag{2.32}$$

For the above second order linear system, the necessary and sufficient conditions for stable equilibrium at $\theta = \theta_e$ are $I_O > 0$, $c > 0$, and $k > 0$. The inertia I_O is always positive, so the inequality conditions for the coefficients c and k determine stability. Evaluating the inequality condition for

c yields

$$\frac{C_D}{C_L} > \frac{\cos(\theta_e - \beta_e)\sin(\theta_e - \beta_e)}{1 + \sin^2(\theta_e - \beta_e)} \tag{2.33}$$

Similarly, evaluating the inequality condition for k yields

$$C_D \cos(\theta_e - \beta_e) - C_L \sin(\theta_e - \beta_e) > \frac{(2m_k + m_t)g}{\rho A U_\infty^2} \sin\theta_e \tag{2.34}$$

Stability analysis with catenary tether

In this section, we will relax the straight tether assumption and instead consider the tether to retain the catenary shape for small perturbations about the equilibrium. This amounts to using a statics based model for the catenary while studying the dynamic behavior of the tether-airfoil system close to equilibrium. Now we have a 2DOF system since y_c and z_c can change independently as long as the tether length l_t remains unchanged.

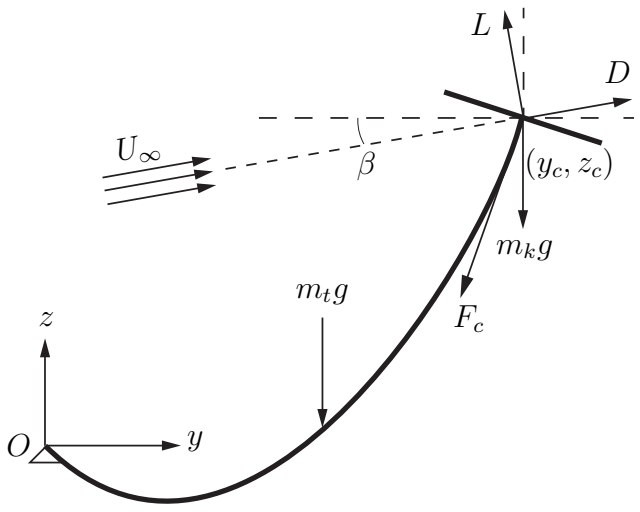

Figure 2.8: Catenary tether-airfoil with external forces

The equations of motion are

$$m_k \ddot{y}_c = D\cos\beta - L\sin\beta - F_{c,y} \tag{2.35}$$

$$m_k \ddot{z}_c = D\sin\beta + L\cos\beta - F_{c,z} - m_k g \tag{2.36}$$

We linearize the equations of motion about the equilibrium point (y_e, z_e)

$$\begin{aligned} m_k \delta\ddot{y} = &\left.\frac{\partial D\cos\beta}{\partial \dot{y}}\right|_e \delta\dot{y} + \left.\frac{\partial D\cos\beta}{\partial \dot{z}}\right|_e \delta\dot{z} - \left.\frac{\partial L\sin\beta}{\partial \dot{y}}\right|_e \delta\dot{y} \cdots \\ &- \left.\frac{\partial L\sin\beta}{\partial \dot{z}}\right|_e \delta\dot{z} - \left.\frac{\partial F_{c,y}}{\partial y}\right|_e \delta y - \left.\frac{\partial F_{c,y}}{\partial z}\right|_e \delta z \end{aligned} \tag{2.37}$$

and

$$\begin{aligned} m_k \delta\ddot{z} = &\left.\frac{\partial D\sin\beta}{\partial \dot{y}}\right|_e \delta\dot{y} + \left.\frac{\partial D\sin\beta}{\partial \dot{z}}\right|_e \delta\dot{z} + \left.\frac{\partial L\cos\beta}{\partial \dot{y}}\right|_e \delta\dot{y} \cdots \\ &+ \left.\frac{\partial L\cos\beta}{\partial \dot{z}}\right|_e \delta\dot{z} - \left.\frac{\partial F_{c,z}}{\partial y}\right|_e \delta y - \left.\frac{\partial F_{c,z}}{\partial z}\right|_e \delta z \end{aligned} \tag{2.38}$$

where $\delta y = y - y_e$ and $\delta z = z - z_e$ and $|_e$ represents calculation at the equilibrium. Carrying out the derivatives for the aerodynamic forces in Eq. (2.37) using Eq. (2.28), and noting in Figure 2.5 that $\alpha - \beta + \phi_k = \frac{\pi}{2}$ yields

$$\begin{aligned} m_k \delta\ddot{y} = &\frac{1}{2}\rho A \left[C_L U_{\infty,z}\cos\beta_e - C_D\left(\frac{U_{\infty,y}^2 + U_\infty^2}{U_\infty}\right) \cdots \right. \\ &\left. + U_{\infty,z}\left(\cos\beta_e \left.\frac{dC_D}{d\alpha}\right|_e - \sin\beta_e \left.\frac{dC_L}{d\alpha}\right|_e\right)\right]\delta\dot{y} \cdots \\ &+ \frac{1}{2}\rho A \left[C_L\left(\frac{U_{\infty,z}^2 + U_\infty^2}{U_\infty}\right) - C_D U_{\infty,z}\cos\beta_e \cdots \right. \\ &\left. + U_{\infty,y}\left(-\cos\beta_e \left.\frac{dC_D}{d\alpha}\right|_e + \sin\beta_e \left.\frac{dC_L}{d\alpha}\right|_e\right)\right]\delta\dot{z} \cdots \\ &- \left.\frac{\partial F_{c,y}}{\partial y}\right|_e \delta y - \left.\frac{\partial F_{c,y}}{\partial z}\right|_e \delta z \end{aligned} \tag{2.39}$$

Performing the same steps on Eq. (2.38) yields

$$\begin{aligned} m_k\delta\ddot{z} = &-\frac{1}{2}\rho A\left[C_L\left(\frac{U_{\infty,y}^2+U_\infty^2}{U_\infty}\right)+C_D U_{\infty,z}\cos\beta_e\cdots\right.\\ &\left.+U_{\infty,z}\left(\sin\beta_e\frac{dC_D}{d\alpha}\bigg|_e+\cos\beta_e\frac{dC_L}{d\alpha}\bigg|_e\right)\right]\delta\dot{y}\cdots\\ &-\frac{1}{2}\rho A\left[C_L U_{\infty,z}\cos\beta_e+C_D\left(\frac{U_{\infty,z}^2+U_\infty}{U_\infty}\right)\cdots\right.\\ &\left.-U_{\infty,y}\left(\sin\beta_e\frac{dC_D}{d\alpha}\bigg|_e+\cos\beta_e\frac{dC_L}{d\alpha}\bigg|_e\right)\right]\delta\dot{z}\cdots\\ &-\frac{\partial F_{c,z}}{\partial y}\bigg|_e\delta y-\frac{\partial F_{c,z}}{\partial z}\bigg|_e\delta z \end{aligned} \tag{2.40}$$

where, in Eqs. (2.39) and (2.40)

$$\frac{dC_L}{d\alpha}\bigg|_e=\frac{2\pi}{1+\frac{2}{eAR}},\ \frac{dC_D}{d\alpha}\bigg|_e=\left(\frac{dC_d}{d\alpha}+\frac{2C_L}{\pi eAR}\frac{dC_L}{d\alpha}\right)\bigg|_e \tag{2.41}$$

are obtained from Eqs. (2.17) and (2.18). To solve the spatial derivatives of $F_{c,y}$ and $F_{c,z}$, we proceed as follows. We first note from Eq. (2.22) that

$$\cosh\left(\frac{q}{a}\right)=-\frac{h}{a},\quad z_e=\cosh\left(\frac{y_e-q}{a}\right)+h \tag{2.42}$$

Upon differentiation and rearranging Eqs. (2.42) and (2.23),

$$\mathbf{A}\begin{bmatrix} da\\ dq\\ dh\end{bmatrix}=\mathbf{B}\begin{bmatrix}\delta y\\ \delta z\end{bmatrix} \tag{2.43}$$

where $\mathbf{A} \in \mathbb{R}_{3\times 3}$ and $\mathbf{B} \in \mathbb{R}_{3\times 2}$. The entries for $\mathbf{A}$ are

$$\begin{aligned}
a_{11} &= -\left[q\sinh\left(\frac{q}{a}\right)+h\right], \qquad a_{12} = a\sinh\left(\frac{q}{a}\right)\\
a_{21} &= \left(\frac{y_e-q}{a}\right)\sinh\left(\frac{y_e-q}{a}\right) - \cosh\left(\frac{y_e-q}{a}\right)\\
a_{22} &= \sinh\left(\frac{y_e-q}{a}\right)\\
a_{31} &= \frac{l_t}{a} - \frac{q}{a}\cosh\left(\frac{q}{a}\right) - \left(\frac{y_e-q}{a}\right)\cosh\left(\frac{y_e-q}{a}\right)\\
a_{32} &= \cosh\left(\frac{q}{a}\right) - \cosh\left(\frac{y_e-q}{a}\right)\\
a_{13} &= a, \qquad a_{23} = -1, \qquad a_{33} = 0
\end{aligned} \tag{2.44}$$

and the entries for $\mathbf{B}$ are

$$\begin{aligned}
&b_{11} = 0, \quad b_{12} = 0, \quad b_{21} = \sinh\left(\frac{y_e-q}{a}\right), \quad b_{22} = -1\\
&b_{31} = -\cosh\left(\frac{y_e-q}{a}\right), \qquad b_{32} = 0
\end{aligned} \tag{2.45}$$

From Eqs. (2.21) and (2.24) we have

$$dF_{z,1} = -dF_{z,2}, \quad dF_{y,1} = -dF_{y,2} \tag{2.46}$$

Now, for a small change in the catenary, the corresponding change in slope and tension forces at $(0,0)$ can be related as

$$d\left(\frac{dz}{dy}\right)\Big|_{(0,0)} = \frac{F_{z,1}+dF_{z,1}}{F_{y,1}+dF_{y,1}}, \tag{2.47}$$

which upon simplification yields

$$\begin{aligned}\frac{F_{z,1}+dF_{z,1}}{F_{y,1}+dF_{y,1}} &= \frac{F_{z,1}}{F_{y,1}} - \frac{1}{a}\cosh\left(\frac{-q}{a}\right)\begin{bmatrix}\frac{-q}{a} & 1 & 0\end{bmatrix}\begin{bmatrix} da \\ dq \\ dh \end{bmatrix} \\ &= \frac{F_{z,1}}{F_{y,1}} - \mu\mathbf{M}\mathbf{A}^{-1}\mathbf{B}\begin{bmatrix}\delta y \\ \delta z\end{bmatrix} \\ &= \frac{F_{z,1}}{F_{y,1}} - p\delta y - q\delta z \end{aligned} \tag{2.48}$$

Eq. (2.48) can be expressed as

$$\begin{bmatrix} F_{z,1} \\ -F_{y,1}\end{bmatrix}^T\begin{bmatrix} dF_{y,2} \\ dF_{z,2}\end{bmatrix} = -F_{y,1}^2\begin{bmatrix} p \\ q\end{bmatrix}^T\begin{bmatrix}\delta y \\ \delta z\end{bmatrix} \tag{2.49}$$

Taking a similar approach for (y_e, z_e) yields

$$\begin{bmatrix} -F_{z,2} \\ F_{y,2}\end{bmatrix}^T\begin{bmatrix} dF_{y,2} \\ dF_{z,2}\end{bmatrix} = -F_{y,2}^2\begin{bmatrix} u-\nu \\ v\end{bmatrix}^T\begin{bmatrix}\delta y \\ \delta z\end{bmatrix} \tag{2.50}$$

where,

$$\nu = \frac{1}{a}\cosh\left(\frac{y_e - q}{a}\right),\ \mathbf{N} = \begin{bmatrix}\frac{y_e-q}{a} & 1 & 0\end{bmatrix}, \tag{2.51}$$

and u and v are defined as

$$\nu\mathbf{N}\mathbf{A}^{-1}\mathbf{B}\left[\delta y \ \ \delta z\right]^T = u\delta y + v\delta z \tag{2.52}$$

Combining Eqs. (2.49) and (2.50) we get

$$\left[\partial F_{c,y} \ \ \partial F_{c,z}\right]^T = \left[\partial F_{y,2} \ \ \partial F_{z,2}\right]^T = \mathbf{Q}^{-1}\mathbf{U}\left[\partial y \ \ \partial z\right]^T \tag{2.53}$$

where

$$\mathbf{Q} = \begin{bmatrix} F_{z1} & -F_{y1} \\ -F_{z2} & F_{y2} \end{bmatrix}, \ \mathbf{U} = \begin{bmatrix} -pF_{y1}^2 & -qF_{y1}^2 \\ -(u-\nu)F_{y2}^2 & -vF_{y2}^2 \end{bmatrix}. \tag{2.54}$$

When assembled as a matrix equation, Eqs. (2.39) and (2.40) take the form

$$\begin{bmatrix} m_k & 0 \\ 0 & m_k \end{bmatrix} \begin{bmatrix} \delta\ddot{y} \\ \delta\ddot{z} \end{bmatrix} + \mathbf{C} \begin{bmatrix} \delta\dot{y} \\ \delta\dot{z} \end{bmatrix} + \mathbf{K} \begin{bmatrix} \delta y \\ \delta z \end{bmatrix} = 0 \tag{2.55}$$

The matrix $\mathbf{C}$ consists solely of terms from aerodynamic forces, and $\mathbf{K}$ consists of terms related to the tension in the tether. For stability, the eigenvalues of the matrix

$$\begin{bmatrix} \mathbf{0} & \mathbf{I}_{2\times 2} \\ -\mathbf{M}^{-1}\mathbf{K} & -\mathbf{M}^{-1}\mathbf{C} \end{bmatrix} \tag{2.56}$$

must have negative real parts. Solving for the eigenvalues of Eq.(2.56) analytically is tedious and hence we resort to numerical computations to generate a root-locus, shown in the next section.

Simulations and Observations

Before presenting the simulation results, the specific formulae for C_L and C_D developed for this model are given. We assume a square shaped wing span with one of the corners facing the head wind. For a square of side a, from Eq. (2.17) $AR = (\sqrt{2}a)^2/a^2 = 2$. The parameter ϵ is taken as 0.8 and $\alpha_{L,0}$ as -0.035rad ($\approx 2^\circ$) based on experimental data from various NACA airfoils presented in [2, 3, 7]. This yields

$$C_L = 2.793(\alpha + 0.035) \tag{2.57}$$

The profile drag C_d was obtained from [43], based on the range of Reynolds numbers expected for wind speeds varying from 10 m/s to 30 m/s. The resulting drag coefficient is

$$C_D = 0.1943\alpha^2 + 0.00625 + 0.199C_L^2 \tag{2.58}$$

Energy extraction through base actuation

For this simulation, we assume the parameter values of Table 2.1 and the parameter values specific to this simulation are $m_k = 3$kg, and $A = 25\text{m}^2$. These values are chosen different from those used for the stability investigation presented earlier just to show that considerable energy extraction is possible. We assume $U_{\infty,y} = 17$ m/s and $U_{\infty,z} = 0$ m/s. The initial conditions for this simulation are $\phi_i(0) = 1.3$rad, and $\dot{\phi}_i(0) = 0$rad/s for $i = 1, 2, \cdots, 10$. In the simulation, we allow the system to converge to equilibrium and subsequently at $t = 150$s we initiate a sinusoidal base actuation of amplitude 6 m and frequency 0.2Hz. Thus,

$$y_0(t) = \begin{cases} 0 & \text{for } t < 150 \text{ s} \\ 6\sin\left(0.4\pi(t-150)\right) & \text{for } t \geq 150 \text{ s} \end{cases} \tag{2.59}$$

Simultaneously, the angle of inclination ϕ_k is varied in synchronization with the base motion, with an amplitude of 6.5° but with a phase shift of 110°, as follows

$$\phi_k = \begin{cases} 75^\circ & \text{for } t < 150 \text{ s} \\ 81.11^\circ - 6.5^\circ \sin\left(0.4\pi(t-150) + 110^\circ\right) & \text{for } t \geq 150 \text{ s} \end{cases} \tag{2.60}$$

The amplitude and phase shift of ϕ_k actuation were chosen to provide significant energy extraction but were not optimized. From Eqs. (2.8) and (2.15), the above designed trajectory of ϕ_k can be

ideally achieved by designing the actuation force F_a as

$$F_a = \frac{I\ddot{\phi}_k + M_a}{2d} \tag{2.61}$$

This idealized F_a is used in this work. However, in practice, a feedback controller must be used to track a desired ϕ_k trajectory such as the one in Eq. (2.60). The response of the system is shown in Figure 2.9. The individual plots are self-explanatory.

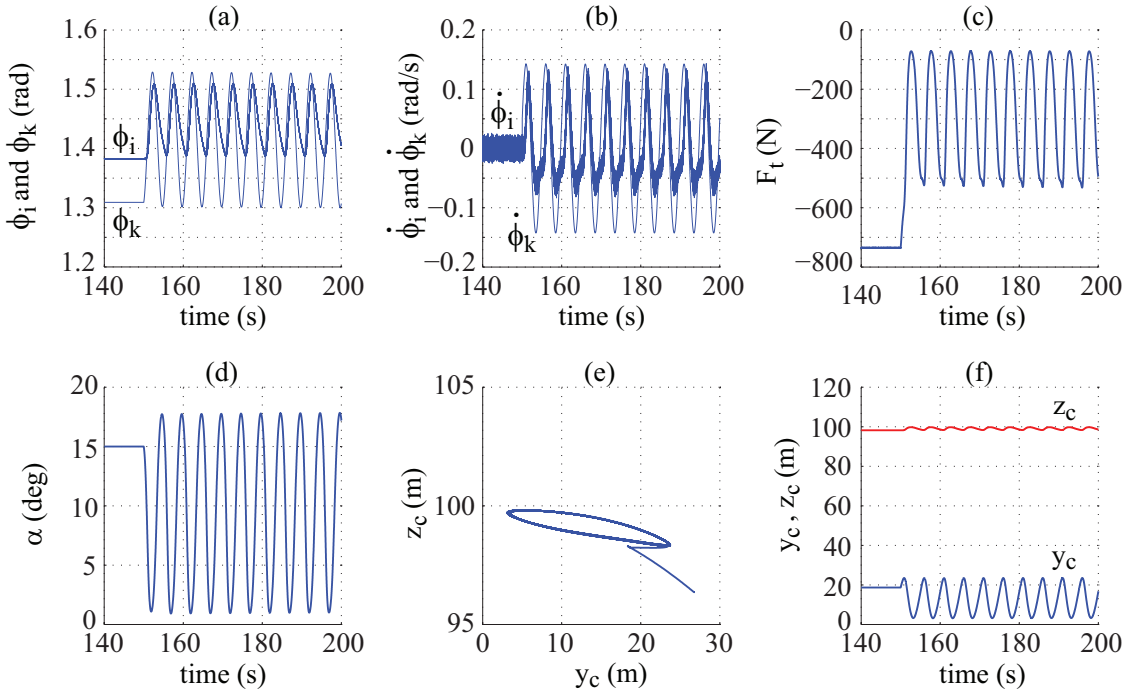

Figure 2.9: Tether-airfoil system simulation under base actuation

The energy extracted is obtained from the integral

$$E_{ex} = \int_0^t F_t\, \dot{y}_0 dt \tag{2.62}$$

and is plotted in Figure 2.10. A negative value of the integral indicates a net energy extraction.

Also, the slope of E_{ex} gives an indication of the power generated. As seen in Fig.2.10, the power generated is approximately 800W for the simulation shown. It is noted that the energy extraction can be maximized through selection of optimum design parameters or through control/actuation optimization.

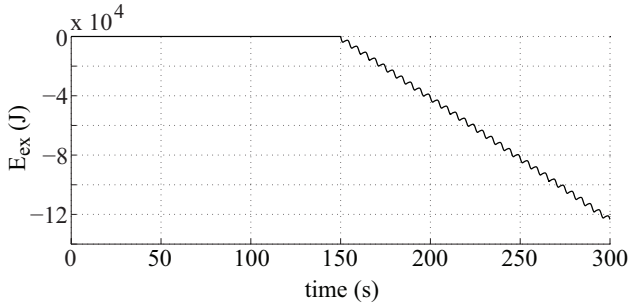

Figure 2.10: Wind energy extracted through base actuation

Stability conditions: straight tether assumption

Table 2.1 shows the parameters used in simulating the airfoil's operation. Our preliminary estimates of the total tether drag, assuming it to be a vertical cylinder, is ≤ 5N even with a conservative estimate of the tether diameter (assuming a tether made of Kevlar). Hence, we assert that the negligible tether drag assumption is plausible, [43]. Using the same numerical as in [7], a simulation is run for 300 seconds with the step wind change from $U_{y,i}$ to $U_{y,f}$ occurring at 200 seconds. The results of the simulation are shown in Figure 2.11. As shown in Figure 2.11(a), the average tether angle ϕ_i ranges from about 1.34 radians before the step change to about 1.45 radians after the step change. The tight bands of ϕ_i values indicate a high level of tension within the tether. Referring to Eq.(2.33) and Figure 2.11(e), there are two values of θ_e to consider, namely $\theta_e = \tan^{-1}(97.3/22.9) = 1.3399$ rads, and $\theta_e = \tan^{-1}(99.2/12.5) = 1.4455$ rads.

Table 2.1: Simulation parameters

Parameter	**Value**
l_t	100 m
m_t	0.5 kg
m_k	2 kg
A	2 m^2
I_O	2.5 $\mathrm{kg} \cdot \mathrm{m}^2$
ρ	1.3 $\mathrm{kg} \cdot \mathrm{m}^{-3}$
d	0.5 m
$U_{y,i}$	15 $\mathrm{m} \cdot \mathrm{s}^{-1}$
$U_{y,f}$	20 $\mathrm{m} \cdot \mathrm{s}^{-1}$
$n+1$	10

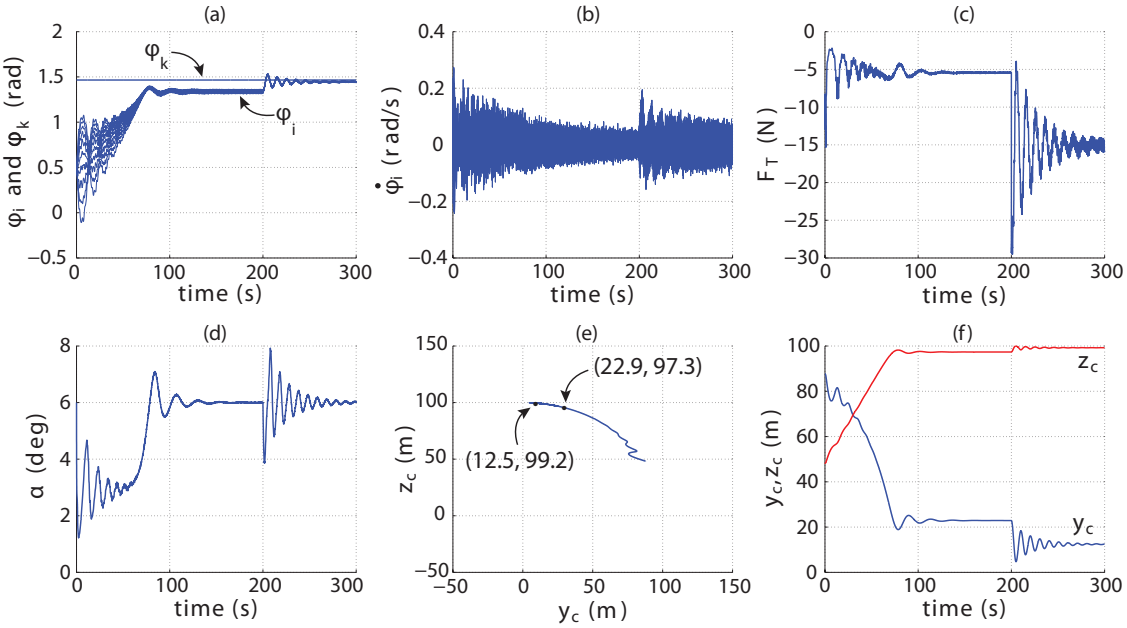

Figure 2.11: Response to step change in wind speed

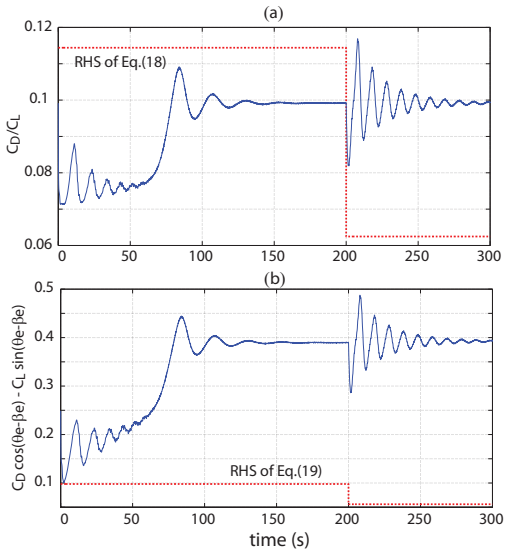

Figure 2.12: Verifying stability criteria from straight tether assumption

The calculated ratio and the simulated ratio of C_D to C_L are both shown in Figure 2.12(a). The calculated ratio is found using Eq. (2.33) and the values for θ_e mentioned above. The value of θ_e is assumed to change instantaneously with the step wind change. The simulated ratio is found using the simulated values of C_D and C_L at each time step. As shown in Figure 2.12(a), for the first 200 seconds of simulation, the first stability criterion defined by Eq. (2.33) is violated, yet the equilibrium is stable. However, once the wind speed is increased, the stability criterion is satisfied. The second stability criterion comes from Eq. (2.34) and is represented graphically in Figure 2.12(b). In this case, the second stability criterion is satisfied at all times. The above results show the validity of the straight tether assumption at higher wind speeds.

Stability conditions: catenary

As mentioned earlier, the catenary model represents a more accurate geometric configuration of the tether under steady state operating conditions.

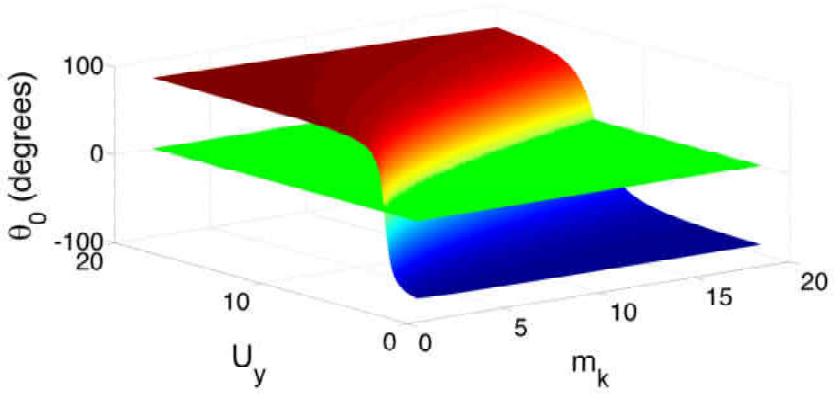

Figure 2.13: Equilibrium tether angles for varying U_y and m_k

Figure 2.13 graphically illustrates the equilibrium angle θ_0 for a range of wind speeds U_y and airfoil mass m_k. The angle θ_0 represents the angle made by the tether with the horizontal at the base $(0, 0)$. The plot confirms the expected result that as the mass increases and/or the wind speed reduces, the equilibrium point transitions from one with positive altitude to one with negative altitude. Recall that solving for the eigenvalues of Eq.(2.56) will provide insight to the stability of a given equilibrium point. We next generate the root locus plot where, in Figure 2.14(a) the wind speed U_y is held constant and the airfoil mass m_k is varied over a range. In Figure2.14(b), the airfoil mass m_k was chosen to be 2kg, and the wind speed U_y was varied. All of the eigenvalues shown in Figure 2.14 have negative real parts, thus indicating that the static equilibrium points are stable.

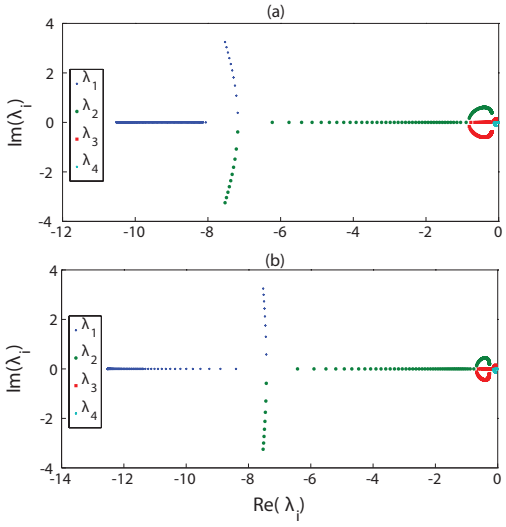

Figure 2.14: Root locus from catenary tether model (a) varying m_k and (b) varying U_y

Conclusion

A stability analysis for a tether-airfoil has been presented, and conditions for the existence of stable equilibria have been investigated. For a straight tether, an assumption that would be valid for high wind speeds, analytical conditions for stability were derived and confirmed through simulations. Since the tether length and weight can be substantial, the tether model was refined to that of a catenary. A statics based model of the catenary was augmented to the dynamic model of the airfoil, to perform a more realistic study of stability. For the latter case, stability of equilibrium points for varying wind speed and varying airfoil mass were verified numerically. Future work will include analyzing stability when the tether-airfoil system is used for harnessing wind energy. Also, a linearization approach, which gives necessary and sufficient conditions for stability, cannot be used to detect periodic orbits, such as crosswind flight.

At 10-12km tether lengths needed to access higher altitudes, a reeling action or a mobile base would be subject to large time delays and uncertainties between the base and the kite which would

result in numerous issues from a control and stability standpoint. Also, conditions vary greatly along the tether, so icing could potentially be an issue, and there is also the concern that the long tether lengths would interfere with aviation. Instead, we propose replacing the tethered airfoil with a tethered autogyro device.

CHAPTER 3: NON-TRADITIONAL WEDs: THE AUTOGYRO CONCEPT

Background and Introduction

Wind data from high altitudes shows that there is an abundance of wind power available and that its availability isn't restricted by geographical location. A study in [4] provides an insight to the magnitude of wind power available at altitudes of 7-16km, which is roughly 100 times that of the global energy demand. This abundance of energy is primarily attributed to the existence of jet streams [38]. It has prompted a renewed interest in airborne wind energy (AWE) systems.

Airborne wind energy devices in the form of airborne windmills were first proposed in the first half of the 1900s. Originally conceived to power communications aerostats, windmills were placed on the aircraft and were used to generate the power needed to run the communications equipment [27]. The concept of a rotorcraft placed permanently in the upper atmosphere was proposed by Fletcher [12]; the rotors were designed to generate electricity as well as provide lift to support the airframe. Stability analysis of the proposed system showed the need for an active control mechanism in order to maintain flight.

In recent years, alternative energy research has attracted attention and with it there has been a renewal of interest in airborne wind energy. Ockels [30] proposed the Laddermill concept; a device comprised of a series of kites that move a closed cable through a generator. Several variations on the Laddermill concept also exist in literature [45, 47, 46]. Current AWE device designs can be classified according to [14]:

- **Altitude**
    a) Low and medium
    b) >600m above ground
- **Generator Position**
    a) On ground
    b) On board
- **Device Weight**
    a) Lighter than air (LTA)
    b) Heavier than air (HTA)
- **Aerodynamics**
    a) Helicopter type
    b) Airfoil type (kite, wing, etc.)
    c) Aerostat type

In all these categories, most of recent and ongoing research are essentially in low and medium altitude range (typically less than 1km). However, jet streams occur at much higher altitudes (10-12km). Even though a large amount of energy is available at such high altitudes, even at lower altitudes of 4-5km there exists a vast amount of energy to be harvested.

In prior work [37, 8], we proposed using tethered airfoils to tap into the energy available in the wind at high altitudes. However, for high altitudes, the proposed method of generating power by reeling the kite in and out from a base point, or by using a moving base to harvest energy appear

impractical. At 10-12km (or 4-5km) tether lengths needed to access higher altitudes, a reeling action or a mobile base would be subject to large time delays and uncertainties between the base and the kite which would result in numerous issues from a control and stability standpoint. Also, conditions vary greatly along the tether, so icing could potentially be an issue, and there is also the concern that the long tether lengths would interfere with aviation. Instead, we propose replacing the tethered airfoil with a tethered autogyro device. In [38] the authors discussed a power generator based on the concept of the autogyro, however a thorough mathematical analysis is lacking in this work. The objective of the work in this thesis is to build a mathematical model of the autogyro based on first principles. In this regard, we revisit the theory of the autogyro that was first formally developed in the mid-1920s [17, 25] and then expanded upon in the mid-1930s [40]. In principle, an autogyro, also called a gyroplane, uses an unpowered rotor in a state of autorotation to develop lift. Autorotation is a flight state where the rotor is being turned by oncoming air flow moving through the rotor disk.

In this chapter, we first discuss the principles of the autogyro. Next, we summarize the blade element theory of the autogyro originally presented in [17]. Subsequently, we discuss a possible method of using an autogyro-based aircraft to extract power from high altitude winds. We then use this preliminary model to investigate the feasibility of using autogyro rotors as a viable method of generating wind power through simulations. Next, we discuss future work as a result of our findings. Finally, we draw conclusions on the theoretical application of the autogyro to airborne energy extraction.

The Principles of Autogyro

An autogyro, while similar to a helicopter, has different actuation architecture and added degrees of freedom. It is comprised of three or four blades that are free to spin about their common axis;

and each blade is additionally free to rotate (flap) up and down about a hinge at its root, which is normal to the spin axis. The motivation behind using the autogyro principle for energy extraction is primarily derived from the autogyro rotor being able to spin freely in wind fields and provide a substantial amount of life and torque. Since wind speeds at high altitudes are very large, an autogyro can potentially generate electricity while the lift is used to support the weight of the complete system, including the tether.

Blade Element Theory of the Autogyro

A schematic diagram of a single rotor autogyro with associated forces is shown in Fig.3.1. Mathematical modeling of the autogyro by Glauert [17] uses the Blade Element Theory. Fig.3.1(a) gives a side view of the rotor. The approach is used to derive the main components, namely the thrust force T, the longitudinal force H, and the rotor torque Q. The disk of rotation of the rotor makes an angle θ with the horizontal and it is translating with a forward speed V in still air, Fig.3.1(a). This initial work assumes that the coning (flapping) angle of a blade β is a periodic function of the blade's angular position ψ ($\dot{\psi} = \Omega$), but considers only the first harmonics, i.e.

$$\beta = \beta_0 - \beta_1 \cos(\psi - \phi_1) \tag{3.1}$$

This coning angle is due to the flapping DOF of each blade, as shown in Fig.3.1(b).

Thrust Force T

The resulting thrust force T is derived starting from a blade element located at a radial distance r along the blade, illustrated in Figs.3.2(a), (b) and (c). The elemental forces are then integrated over each blade span.

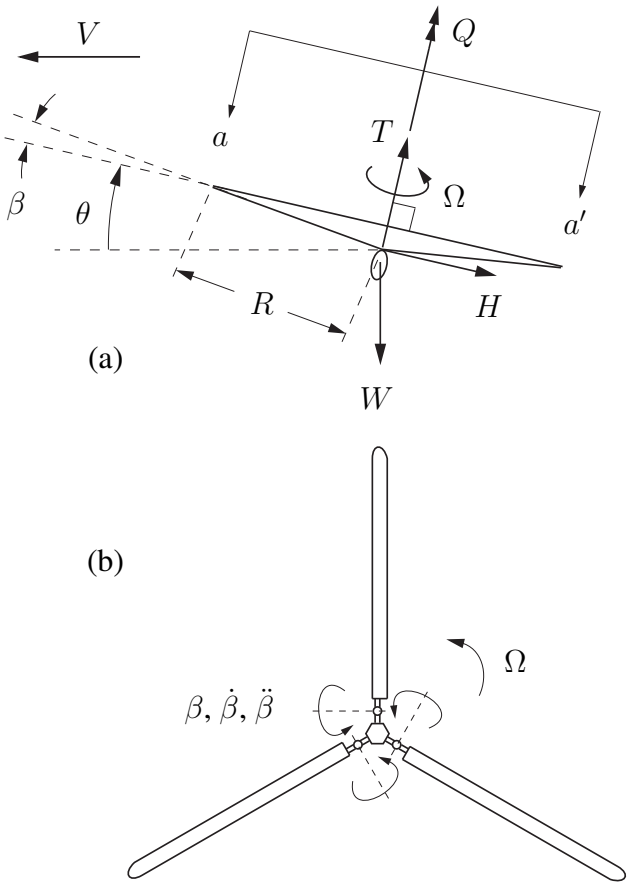

Figure 3.1: (a) Forces on an autogyro, (b) A three-bladed autogyro viewed from plane aa'

A similar approach is taken for determining the longitudinal force H and the aerodynamic torque Q. In the aforementioned studies, expressions of steady-state T, Q and H are derived under the following assumptions:

A1. The angles β (flapping angle) and ϕ_r (angle of attack of the blade element), shown in Figs.3.2(b) and (c), are small.

A2. *Interference/Induced Flow*: In the vicinity of the rotor, the rotor forces generate local induced velocities which alter the undisturbed flow [17, 40]. The net effect is modeled as an induced

axial velocity v

$$v = T/\left(2\pi R^2 \rho V'\right), \quad V' = ((V\sin\theta - v)^2 + V^2\cos^2\theta)^{1/2} \tag{3.2}$$

where v modifies the effective axial velocity of wind to

$$u = V\sin\theta - v \tag{3.3}$$

In [17], v is assumed constant over the entire span R.

A3. The lift coefficient of a blade element is proportional to $\alpha_r = \alpha + \phi_r$, *i.e.*, $C_L = k\alpha_r$, and the drag coefficient is constant, $C_D = \delta$.

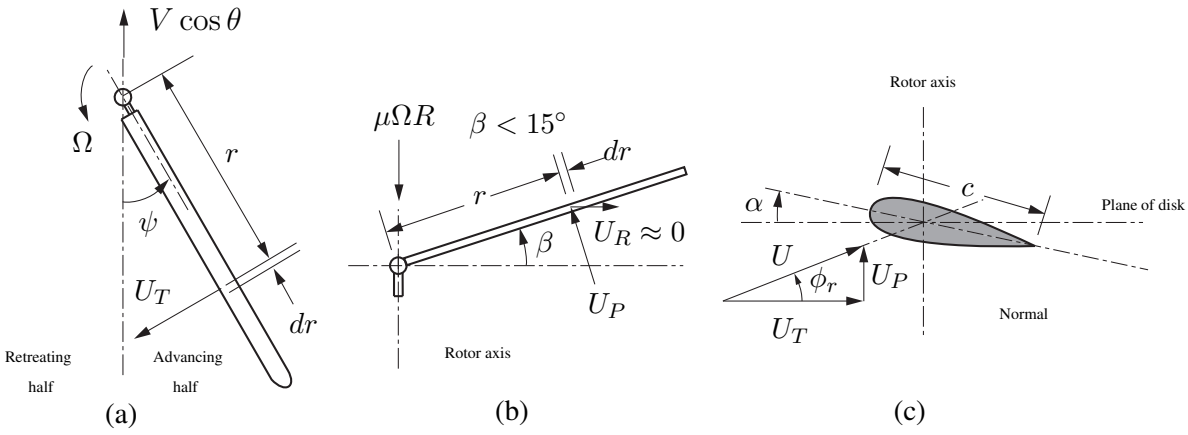

Figure 3.2: Velocities of a blade element: (a) view along the spin axis, (b) view of flapping motion, (c) cross-sectional view

Under the above conditions, the thrust is computed as

$$T = \frac{B}{2\pi}\int_0^{2\pi} d\psi \int_0^R \frac{1}{2}\rho c C_L U^2 dr \tag{3.4}$$

where B is the number of blades, c is the blade chord length (assumed constant), $C_L = k\alpha_r = k(\alpha + \phi_r)$ is the lift coefficient, and U is the resultant relative velocity of the wind at the element. In Eq.(3.4), the thrust component contributed by drag is assumed to be negligible. Assuming that the radial velocity $U_R \approx 0$, the net wind velocity U relative to a blade element is

$$\begin{aligned} U &= \sqrt{U_p^2 + U_T^2} \\ U_P &= U \sin\phi_r = u - r\dot{\beta} - (\beta + \chi)V\cos\theta\cos\psi \\ U_T &= U\cos\phi_r = \Omega r + V\cos\theta\sin\psi \end{aligned} \tag{3.5}$$

where u is defined in Eq.(3.3), β is assumed to be a function of ψ as in Eq.(3.1), and χ is a geometric property of the airfoil sections of each blade, [17]. The Eq.(3.5) can be expressed as

$$\begin{aligned} U\sin\phi_r &= \mu\Omega R - \Omega r\beta_1\sin(\psi - \psi_1) - (\beta_0 + \chi)V\cos\theta\cos\psi \\ U\cos\phi_r &= \Omega r + V\cos\theta\sin\psi \end{aligned} \tag{3.6}$$

For the autogyro, we define the following two speed ratios:

$$\lambda = \frac{V}{\Omega R}, \quad \mu = \frac{u}{\Omega R}. \tag{3.7}$$

The first speed ratio, λ, is the tip-speed ratio. The second, μ, represents the inflow ratio of wind passing through the rotor disk. Assuming ϕ_r to be small, as well as observing that the periodic terms appearing in U_T and U_P in Eq.(3.5) would cancel when the B equispaced blades are taken into consideration,

$$\sum_{i=1}^{B}\sin\left(\psi + \frac{2\pi}{B}(i-1)\right) = \sum_{i=1}^{B}\cos\left(\psi + \frac{2\pi}{B}(i-1)\right) = 0 \tag{3.8}$$

we obtain the approximation

$$\phi_r \approx \tan\phi_r = \frac{\mu R}{r} \tag{3.9}$$

Since the above approximations break down towards the root of each blade and over a wider span of the blades in the retreating half (see Fig.3.2(a)), the following two conditions are imposed under which the calculated force T will be representative of the physical phenomena.

A1. U_T must be positive over the outer half of the retreating blades, implying from Eq.(3.5), $V\cos\theta < 0.5\Omega R$.

A2. The outer half of each blade operates below a critical angle, *i.e.* $\alpha_r = \alpha + \phi_r < \alpha_{cr}$ for $0.5R \leq r \leq R$ and for all $\psi \in [0,\ 2\pi]$.

Under these conditions, the expression in Eq.(3.4) evaluates to

$$T = T_c \pi \rho \Omega^2 R^4, \quad T_c = \sigma\left(\alpha + \frac{3}{2}\mu\right) \tag{3.10}$$

where $\sigma = Bc/\pi R$ is the blade solidity.

Aerodynamic Torque Q

The average aerodynamic torque generated over one complete rotation for B blades, and using the assumptions listed above, is

$$Q = \frac{B}{2\pi}\int_0^{2\pi} d\psi \left[\int_0^R \frac{1}{2}\rho c\left(C_L U^2 \sin\phi_r - C_D U^2\right) r dr\right] \tag{3.11}$$

Upon carrying out the integration, and using Eqs.(3.8) and (3.10), Q reduces to

$$Q = Q_c \pi R^2 \rho \Omega^2 R^3, \quad Q_c = \frac{1}{4}\sigma\delta - \mu T_c \tag{3.12}$$

where $C_D = \delta$ is a constant drag coefficient assumed for low angles of attack. Under steady-state operation, let the autogyro provide a thrust force $T = W_d$, where $W_d > W$, with W being the total weight to be supported. Then, setting $Q = 0$ and noting that a sensible solution has $\mu > 0$, from Eqs.(3.10), (3.11), and (3.12) we find the following expressions for steady-state μ and spin speed Ω

$$\mu = \frac{1}{3}\left[\sqrt{\alpha^2 + \frac{3}{2}\delta} - \alpha\right], \quad \Omega = \sqrt{\frac{W_d}{Bc\rho R^3(\alpha + \frac{3}{2}\mu)}} \tag{3.13}$$

Longitudinal and Lateral Forces

The longitudal force is similarly obtained by integrating over blade elements. The final expression is $H = H_c \pi R^2 \rho \Omega^2 R^2$, where H_c is a function of σ, α, μ, λ, θ and geometric parameters of the blade. A lateral force Y is also generated (perpendicular to the plane of the paper in Fig.3.1(a)) due to differences in aerodynamic forces between the advancing half and the retreating half. This force is of secondary importance and the detailed derivation of Y and H can be found in [17]. Both derivations of Y and H involve the equation of motion of flapping of each blade, which has the general form

$$I_1\left(\ddot{\beta} + \Omega^2\beta\right) = TM_1 - G_1 - \Omega^2 J_1 \tag{3.14}$$

where, the subscipt (1) denotes values for a single blade, TM denotes the flapping moment due to thrust force, G_1, I_1 and J_1 are line integrals involving line density m (assumed constant) of the

blade and are dependent on the blade geometry. Specifically,

$$G_1 = \int_0^L mgrdl, \quad I_1 = \int_0^L mr^2 dl, \quad J_1 = \int_0^L mh(r)rdl \tag{3.15}$$

where, $h(r)$ is a geometric parameter and L is the length of each blade (Note: L is not necessarily equal to R).

Lift and Drag Formulation

The cummulative lift and drag forces generated by the autogyro are related to the thrust T and longitudinal force H through the relations

$$\begin{aligned} F_L &= (T\cos\theta - H\sin\theta) = k_L \pi R^2 \rho V^2 \\ F_D &= (T\sin\theta + H\cos\theta) = k_D \pi R^2 \rho V^2 \end{aligned} \tag{3.16}$$

where k_L, k_D are the lift and drag coefficients. They are related to the coefficient of thrust T_c and the coefficient of longitudinal force H_c through the relation

$$k_L = \frac{T_c \cos\theta - H_c \sin\theta}{\lambda^2} \tag{3.17}$$

$$k_D = \frac{T_c \sin\theta + H_c \sin\theta}{\lambda^2} \tag{3.18}$$

T_c is defined in Eq.(3.10) and λ is the tip-speed ratio defined in Eq.(3.7).

Autogyros for Energy Harvesting

For energy extraction, we consider V to be the steady horizontal wind speed instead of the steady aircraft speed in still air. Energy extraction using a generator effectively provides a load torque

Q_e and reduces the steady state angular velocity Ω. Incorporating Q_e in the analysis amounts to simply setting $Q = Q_e$ in Eq.(3.12) instead of setting $Q = 0$. This results in

$$1.5W_dR\mu^2 + (W_dR\alpha - 1.5Q_e)\,\mu - (Q_e\alpha + 0.25W_dR\delta) = 0 \tag{3.19}$$

which is solved for μ, while the steady-state Ω retains the same expression in Eq.(3.13).

Simulation Results

The steady-state model of the autogyro discussed above was used to compute the lift and drag coefficients, the lift and drag forces, and the relative velocity of the wind for autogyro operation, all as a function of the angle of incidence θ. The parameter values used are similar to those in [40], for which experimental validation was done. The rotor was assumed to have four blades and each blade was assumed to have a length of 17.5 ft and weigh 3% of the total weight of the aircraft. Other parameter values of the simulation are provided in Table 3.1. The value for the density of air was chosen in order to simulate high altitude operation.

Table 3.1: Simulation parameters

Parameter	**Value**	**Description**
B	4	Number of blades
R	17.5	Blade radius (ft)
W	1500	Total weight of autogyro (lbs.)
c	2.75	Blade chord (ft)
σ	$\frac{Bc}{\pi R}$	Rotor solidity
δ	0.006	Mean airfoil drag coefficient
α	0.035	Blade pitch angle (radians)
ρ	0.0008	Air density at 10km altitude ($\mathrm{slugs/ft^3}$)

US units were chosen for comparing results with published results. The following sequence can be used to carry-out the steady-state calculations:

1. Choose a target thrust force $W_d > W$ and a given load torque Q_e.

2. Choose a suitable range of values of $\tau = \lambda \cos\theta$.

3. Solve for μ from Eq.(3.19), and Ω from Eq.(3.13).

4. Solve for T_c and H_c. T_c is given in Eq.(3.10) and H_c can be found from [17].

5. From Eqs.(3.2), (3.3), (3.7) and (3.10) we can show that:

$$\lambda \sin\theta = \mu + \frac{\frac{1}{2}T_c}{\sqrt{\mu^2 + \lambda^2 \cos^2\theta}} \tag{3.20}$$

   Solve for $\lambda \sin\theta$ for each value of $\lambda \cos\theta$.

6. Solve for λ, θ, and solve for V.

7. Solve for k_L, k_D and F_L and F_D.

To validate the model against results given in [17], an initial set of simulations was done for $Q_e = 0$. This can be considered as pure autogyro mode of operation where there is no load torque. The results are shown in Figs.3.3 (a), (b), (c). For a target lift force of $W = 1500$ lb, the target thrust force of $W_d = 2000$ lb was chosen. Figure 3.3(a) verifies the condition $V\cos\theta < 0.5\Omega R$, illustrating that the condition is violated only for a small range of incidence angles $\theta < 5^\circ$. Figure 3.3(b) indicates that the target lift force of $W = 1500$lbs will be achievable for $\theta \leq 40^\circ$. Figure 3.3(c) plots the steady-state relative velocity of the wind that will generate the thrust W_d for a desired angle of incidence θ.

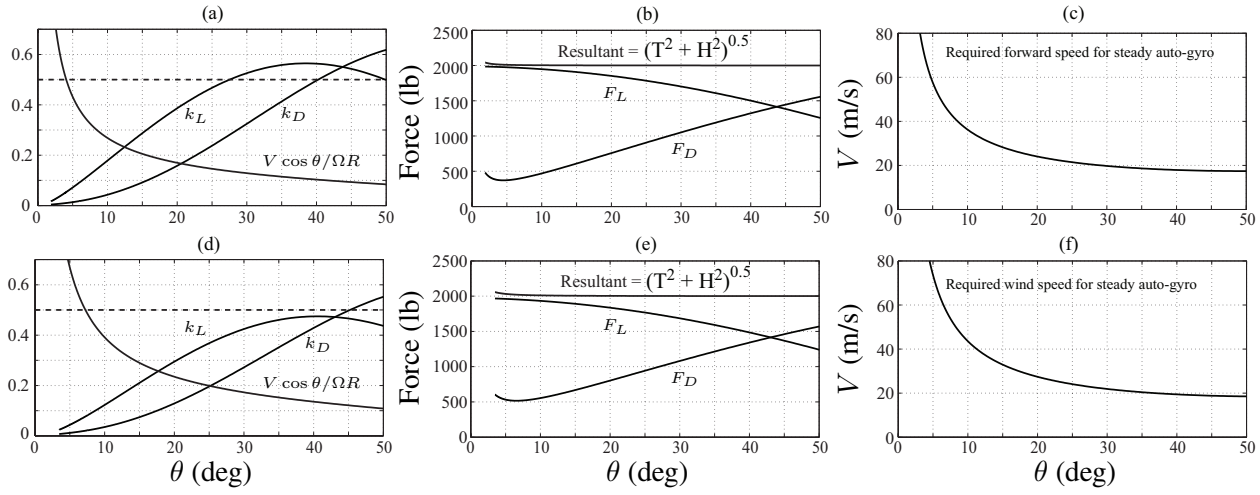

Figure 3.3: Steady-state operation of a single autogyro with varying angles of incidence. Subfigures (a), (b), and (c) correspond to $Q_e = 0$, subfigures (d), (e), and (f) correspond to $Q_e = 1000$ lb·ft.

In the investigation above, 88% of the lift supports the weight of the aircraft (the blades weigh only 12% of the total weight). For an inertially fixed autogyro in a wind field, the lift will be reduced since the autogyro will drive a generator. In addition to the weight of the aircraft, the autogyro rotors will have to support the weight as well as the force of drag on a tether. Preliminary calculations, performed with a 5 mm diameter K-49 Kevlar cable [14] indicates that this force will be much less than the weight W.

The effect of energy extraction is next studied by simulating with various values of Q_e. Results with $Q_e = 1000$lb.ft are shown in Figs.3.3(d), (e), (f). As expected, power extraction results in (i) reduced value of k_L, (ii) violation of the condition $V\cos\theta < 0.5\Omega R$ over a greater range of θ, and (iii) increase in the required wind velocity to generate the same W_d. From the results, it is evident that an effective lift force is generated with $20^\circ \leq \theta \leq 40^\circ$, and higher values of θ is better suited for lowering V.

Next we investigate the validity of the results against underlying assumptions of this theory. As mentioned earlier, the theory is considered valid under two conditions, namely

A1. U_T must be positive over the outer half of the retreating blades, implying from Eq.(3.5), $V\cos\theta < 0.5\Omega R$.

A2. The outer half of each blade operates below a critical angle, *i.e.* $\alpha_r = \alpha + \phi_r < \alpha_{cr}$ for $0.5R \leq r \leq R$ and for all $\psi \in [0,\ 2\pi]$.

The first condition, checked using Figs.3.3 (a) and (d) for $Q_e = 0$ and $Q_e = 1000$ lb.ft, is not too restrictive. The main constraint on the model's accuracy appears to be the second condition. To verify the validity of this condition, the small angle assumption on ϕ_r was removed and the complete expression for ϕ_r, namely

$$\tan\phi_r = \frac{\Omega R\mu - \Omega r\beta_1 \sin(\psi - \phi_1) - [\beta_0 + \chi(r)]\, V\cos\theta\cos\psi}{\Omega r + V\cos\theta\sin\psi} \tag{3.21}$$

was maximized over one full rotation of a blade $\psi \in [0, 2\pi]$. The maximum ϕ_r was used to calculate the maximum angle of attack using the relation $\alpha_r = \alpha + \phi_r$, as a function of $r \in [0,\ R]$. The maxima were plotted for generator torques $Q_e = 0$ and $Q_e = 1000$ lb·ft; the results are shown in Figs.3.4(a) and (b). For the targeted range of incidence angle $\theta \in [20^\circ, 40^\circ]$, it can be seen that while stall angles of $\alpha_{cr} \geq 9^\circ$ would be sufficient when $Q_e = 0$, the stall angle requirement increases to $\alpha_{cr} \geq 11^\circ$ when $Q_e = 1000$. This is expected since power extraction leads to a load torque that reduces Ω. Finally, using the expression in Eq.(3.13) for average Ω, the power extraction from the autogyro was calculated for a range of Q_e values. The results are shown in Fig.3.5. Figure 3.5(a) shows the mechanical power extracted and Figure 3.5(b) shows the steady-state rotor speed needed to maintain sufficient lift as a function of generator torque Q_e.

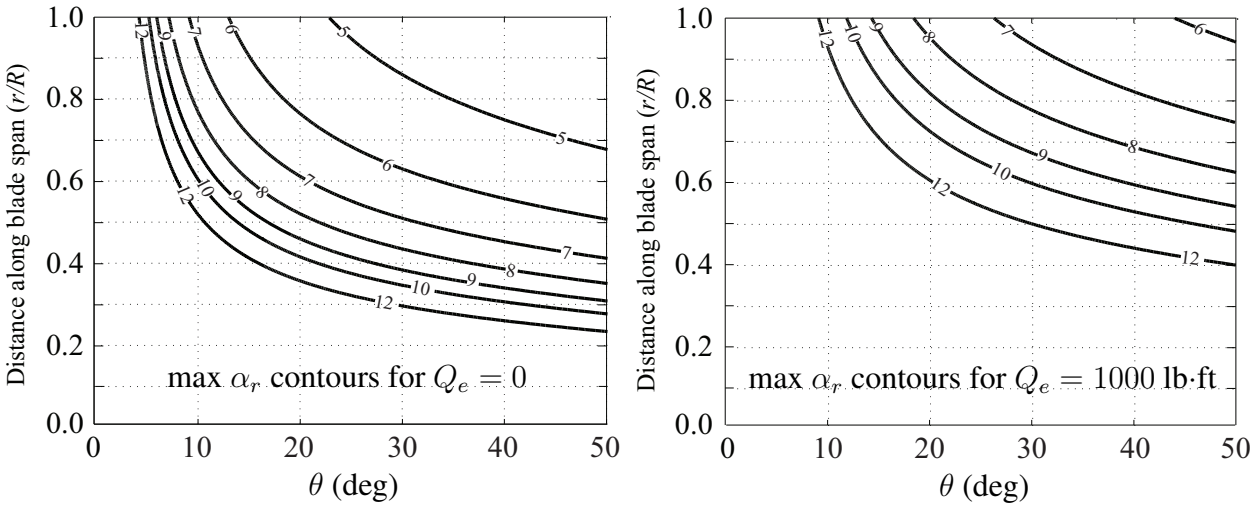

Figure 3.4: Maximum angle of attack α_r along the blade span over one complete rotation

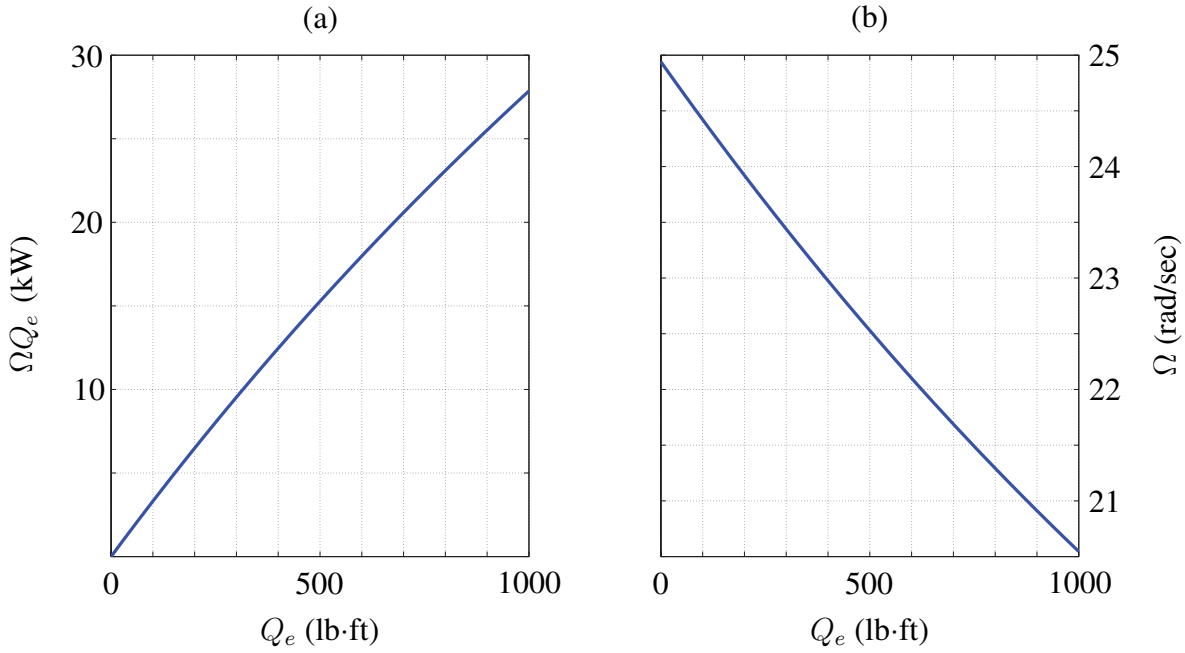

Figure 3.5: (a) Power extracted, (b) steady-state Ω needed to maintain required lift

Model Refinement and Future Work

The analysis presented is a good start, but there are assumptions in the underlying theory which can be relaxed. The first work on autogyro modeling [17] uses the blade element theory approach [15] to derive the thrust force T, the longitudinal force H, and the rotor torque Q. [25] extended this work by relaxing one of the main assumptions, that the squares and higher powers of the ratio of the forward speed to the tip speed τ are negligible. To this end, [25, 40] show that terms of the order of τ^4 can be incorporated in formulations of T, H, and Q if the Fourier expansion of β in terms of ψ includes second-order harmonics, *i.e.*,

$$\beta = \beta_0 - \beta_1 \cos(\psi - \phi_1) - \beta_2 \cos\left(2(\psi - \phi_2)\right) \tag{3.22}$$

where ϕ_1 and ϕ_2 are arbitrary constants. The extension in [25] showed a lift-to-drag ratio higher than that predicted in [17].

Wheatley, [40], extended the work in [17, 25] by considering blades with pitch varying along their span. This was an effort to validate experimental data obtained from the Pitcairn-Cierva autogyro, one of the first functional autogyros [6] The work also incorporated a detailed analysis of the forces in the retreating half of the rotor, Figure 3.2(a), where the blade velocities are reversed. A variant of the autogyro design, better known as the gyroplane, was also studied in [41]. In contrast to the autogyro, where each blade can flap independently, a gyroplane has an even number of blades; the opposite blades are rigidly connected and are allowed to feather, *i.e.*, freely rotate about their span axis. Although the gyroplane is structurally different from the autogyro, both have additional d.o.f. when compared to wind turbines and analytical results in [41] indicate that they have similar overall lift coefficients and lift-to-drag ratios. Other extensions include [42], which models the effect of twisting of blades due to aerodynamic forces, and [16] which refines the analysis in the

retreating half for larger angles of attack and higher speeds.

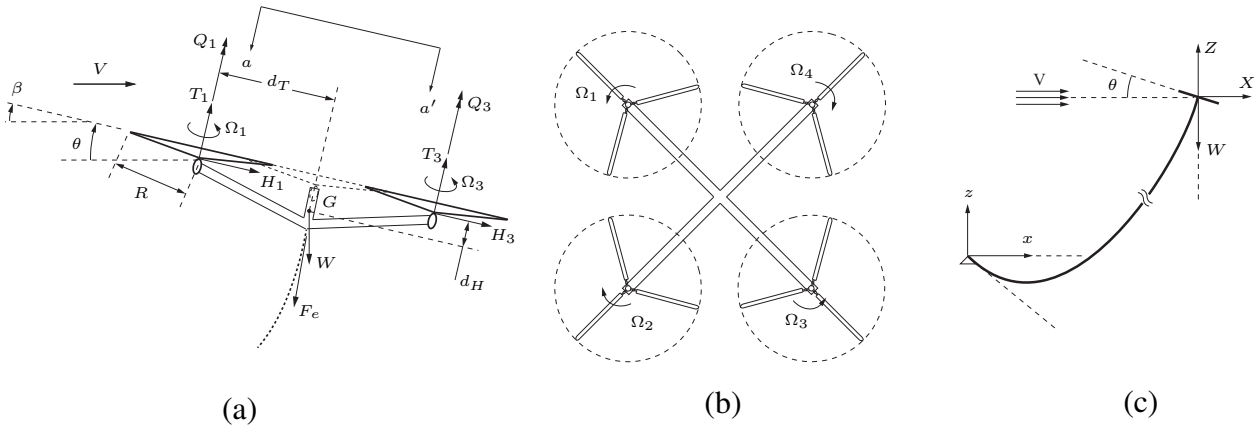

Figure 3.6: Concept of an autogyro-based quadrotor for energy harvesting (a) forces on a tethered autogyro quadrotor, (b) view of the quadrotor from plane aa', (c) global view of simplified autogyro-based AWED

An interesting area of potential research with this concept would be maneuverability and atitude control of the entire power generation system. In Figure 3.6, we describe a potential configuration of the autogyro rotors in the form of a quadropter. The quadropter configuration poses an interesting controls problem from the standpoint of transitioning from powered flight to an autogyro mode, as well as performing various positioning and orientation maneuvers. Our future work will include addressing this problems using theoretical analysis, computer simulations, and physical experiments.

Conclusion

We have provided some preliminary results which support the potential feasibility of using an autogyro-based tethered device for high altitude wind energy harvesting. A model of a single autogyro was developed based on past work by Glauert [17] where the main focus was aviation, rather

than energy harvesting. For addressing the latter, the effect of wind energy extraction was modeled as an additional braking torque. Steady-state conditions were computed to estimate the operating incidence angles and prevailing wind speeds needed for steady autogyro operation while extracting power. While initial impressions indicate that such a device could work, additional research needs to be carried out in order to further validate the concept. In the following two chapters, experimental analysis of the autogyro rotor will be described and the results of the experiments provided.

Before starting on the experimentation, the research leading up to this thesis was purely theoretical. It became apparent that physical data was needed to further validate the concept, and therefore an initiative to start building an experimental framework was undertaken. A large amount of time was dedicated to the design and development of the autogyro rotor itself, which is described in more detail in Chapter 5. Due to the effort required to develop an acceptable rotor prototype, the experiments presented in the following chapters represent an initial effort in the formulation of an experimental framework which will be expanded upon in future research to help validate static and dynamic models of the autogyro based AWED system.

CHAPTER 4: EXPERIMENTAL METHODOLOGY

As inferred in Chapters 1 and 3, in order to further validate the autogyro based AWED concept, experimental data is needed to characterize the performance of an autogyro rotor based upon a specified airfoil profile and geometry. The objective of the experiments carried out for this thesis was to determine multiple aerodynamic parameters of the autogyro rotor. Of particular interest, the relationship between wind speed V_w, the angle of incidence θ, and the rotational speed Ω was sought, as well as data regarding the thrust force T and the lift and drag forces, F_L and F_D.

Wind Tunnel Characterization

Before starting the data collection process, it is important to first perform characterization experiments on the equipment to be used. A plan view of the wind tunnel available for testing the autogyro rotor is shown in Figure 4.1. The wind tunnel is a puller type, meaning that the wind tunnel's fan is positioned downstream of the test section, and its speed is adjusted by opening and closing an aperture between the test section and the fan housing. The further the aperture is opened, the slower the wind speed inside the tunnel, and vice versa. Therefore, in order to set a precedent for experimental repeatability and ease of setup, the relationship between the aperture opening and the resulting wind speed needs to be established. There are multiple ways of measuring wind speed within a wind tunnel, perhaps the most common being the pitot tube. While this method is highly accurate and repeatable, the wind tunnel is only equipped with pitot tubes used to measure static pressure (*i.e.* the pitot tubes terminate at the wall of the tunnel, rather than inside the flow field). In order to measure the wind speed at the center of the tunnel, a pitot tube that extends from the wall up into the flow needs to be fitted.

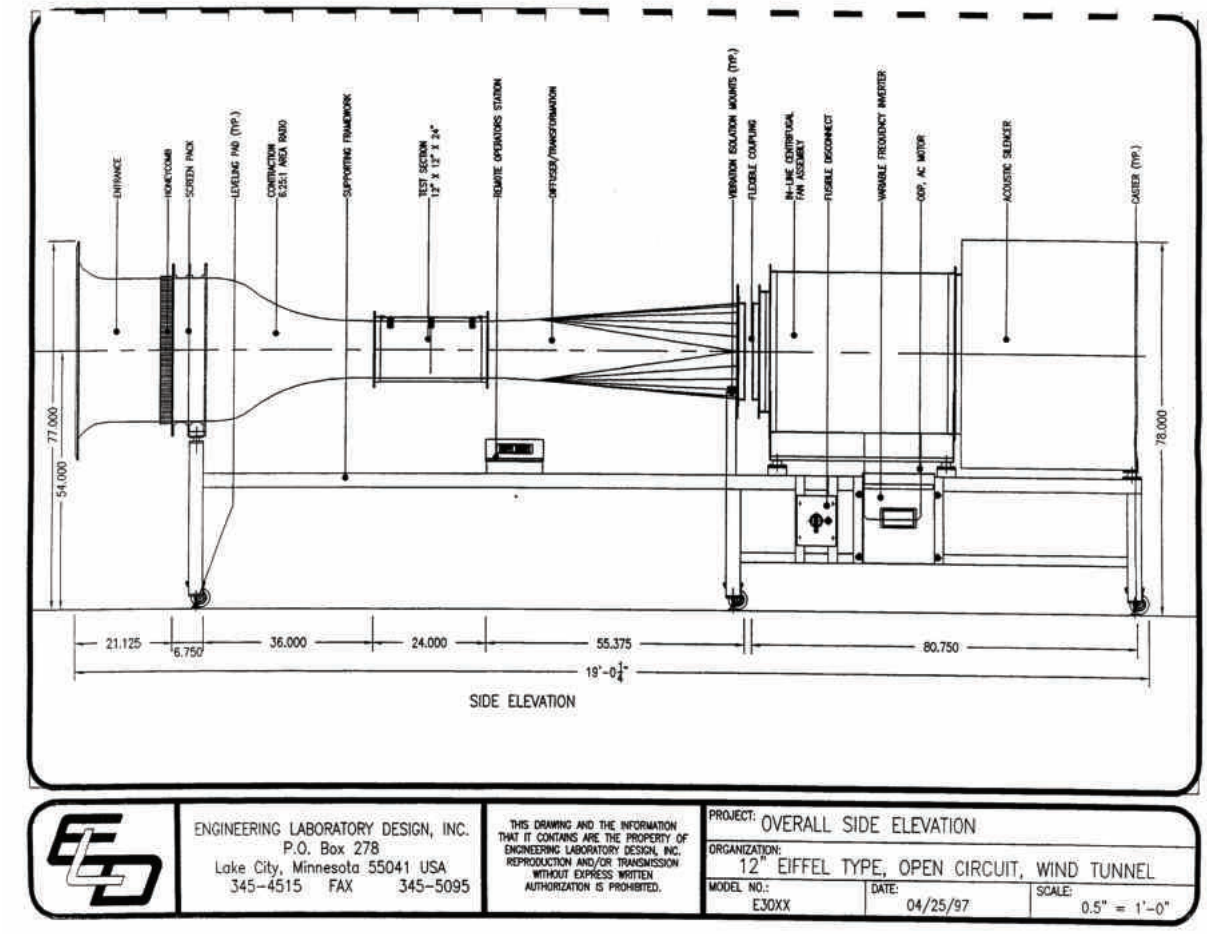

Figure 4.1: Side elevation view of wind tunnel used in experiments

However, the wind tunnel provides no pressure taps for such a pitot tube to be fitted, and modification of the wind tunnel is not allowed, so an alternate solution is required. Apart from pitot tubes, there are several other common devices for measuring wind speeds including hot wire anemometers, ultrasonic wind speed sensors, and handheld airflow meters. To choose the best solution for characterizing the wind tunnel, the three prospective devices were compared against the following requirements:

1. **Cost:** device cannot be prohibitively expensive

2. **Size:** device must fit within the wind tunnel test section without completely blocking the flow

3. **Accuracy:** device must provide accurate wind speed readings

4. **Durability:** device must be able to withstand minor bumps

A summary of how the devices compared to one another is presented in Table 4.1. Within each category, the performance of each device relative to the other two is ranked from 1 (worst) to 3 (best).

Table 4.1: Relative performance summary table

Device	Cost	Size	Accuracy	Durability
Hot wire	2	3	2	1
Ultrasonic	1	1	3	3
Handheld	3	3	2	3

The device chosen for use is the device with the high cumulative score across the four categories. A detailed points breadkdown of the scoring shown in Table 4.1 is shown below:

1. Hot wire anemometer (example device: OMEGA Engineering HHF2005HW)

   a) **Cost:** at time of writing, device cost is $645 (points awarded: 2)

   b) **Size:** hot wire probe is 0.5" in diameter and can be easily inserted into the tunnel through accessory ports (points awarded: 3)

   c) **Accuracy:** $\pm(10\% + lsd)$ of full scale (points awarded: 2)

   d) **Durability:** hot wire is extremely thin and fragile (points awarded: 1)

2. Ultrasonic wind speed sensor (example device: Vaisala WMT700)

a) **Cost:** at time of writing, device cost is $700 (points awarded: 2)

b) **Size:** large dimensions $(348 \times 250 \times 285)$mm nearly exceed wind tunnel test section size (points awarded: 1)

c) **Accuracy:** $\pm 2\%$ of reading (points awarded: 3)

d) **Durability:** designed for use on small boats and all weather conditions (points awarded: 3)

3. Handheld airflow meter (example device: OMEGA Engineering HHF92A)

a) **Cost:** at time of writing, device cost is $169 (points awarded: 3)

b) **Size:** device can be easily inserted into flow field via a side access port to the test section (points awarded: 3)

c) **Accuracy:** $\pm 3\%$ of full scale (points awarded: 2)

d) **Durability:** constructed from high-impact plastic (points awarded: 3)

Therefore, with a combined score of 11 points, the device that will be used to measure the wind speed in the tunnel is the handheld airfoil meter. The handheld airfoil meter selected is the OMEGA Engineering digital anemometer, model number HHF92A. A stock photo of the device is shown in Figure 4.2.

The device fully satisfies the four criteria mentioned above and also includes a feature which can display the minimum, maximum, and average air velocity measurements. The air flow measurement specifications of the HHF92A are presented in Table 4.2. The device has an accuracy of $\pm 3\%$ of the full scale.

Figure 4.2: Omega Engineering HHF92A handheld flow meter

Table 4.2: HHF92A air flow meter specifications

Range	**Resolution**
80 to 6900 ft/min	1 ft/min
0.4 to 35 m/sec	0.01 m/sec
0.9 to 78 mph	0.1 mph
0.8 to 68 knots	0.1 knots
1.4 to 126 km/hr	0.1 km/hr

Wind tunnel characterization procedure

The following procedure will be used to carry out the wind tunnel characterization experiment:

1. Fully close the wind tunnel aperture.

2. Engage the fan motor and allow the wind tunnel to achieve steady-state. The tunnel is assumed to be at steady-state once any sounds that can be related to start up transients die out.

3. Insert the handheld meter into the tunnel, positioning the weather vane portion in the center of the test section.

4. Use the min/max/avg function of the meter to record the average wind speed over 10 seconds.

5. Open the aperture by 0.5" and repeat the data gathering procedure. The experiment is concluded once the aperture is fully open.

Once the data gathering procedures are concluded, the data is imported into MATLAB for processing. The `cftool` package within the Curve Fitting Toolbox is then used to fit a regression curve to the data. The results of this, along with documentation of the experimental procedure are presented in the following chapter.

Angular Velocity Experiment

Due to the expected values for aerodynamic torque being low, it was deemed necessary to use a non-contact type, rather than a contact type, tachometer to measure the rotor speed. Furthermore, due to the low overall weight of the rotor, any additional mass added to the rotor or the rotor shaft would only serve to obfuscate the lift force signal. It was therefore determined that a non-contact type tachometer, located externally to the rotor and rotor shaft assembly would be the best solution. A non-contact type tachometer is formed by extending the principles of an optical encoder, which uses a light beam to measure the angular position of a shaft. An optical encoder is typically disc shaped, with alternating areas of where the light attempting to pass through the disc is either blocked or allowed through, as shown in Figure 4.3. By placing the light detector on the side of the disc opposite that of the light source and by setting the detector to trigger on either the *falling edge* or the *rising edge*, one can ascertain the position of the shaft and the direction of its rotation.

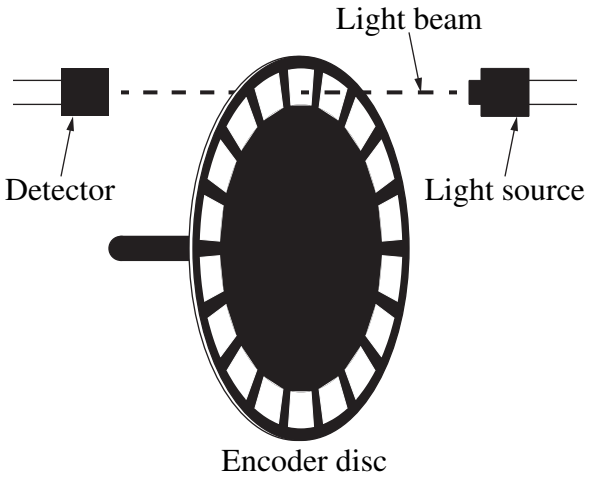

Figure 4.3: An optical encoder disc

The optical encoder can be converted to a tachometer by the finding the time between falling or rising edges, which results in a frequency. Knowing the frequency, the rotational speed can then be obtained.

As shown in Figure 4.3, the three basic parts of the tachometer are (1) the encoder disc, (2) the light source, and (3) the detector. The autogyro rotor was chosen to be the encoder disc, since the blades conveniently form areas where light can pass through or be blocked while the rotor is spinning. The light source and detector were chosen to be an infrared LED and a phototransistor, respectively. Operating within the infrared spectrum was chosen because IR LEDs emit light at wavelengths which are close to the peak spectral response of silicon-based phototransistors [33], thus ensuring strong signals from the phototransistor.

From basic circuits theory, a transistor can be thought of a switch [1] that turns "on" or "off" based on voltages applied to it. A phototransistor uses the photoelectric effect to generate this voltage. A transistor typically has three pins: the base, the collector, and the emitter. For the purposes

of being used as a photdetector, there are two basic circuit types[1]: the common-emitter amplifier circuit, and the common-collector amplifier circuit. The common-emitter amplifier circuit, Figure 4.4(a), generates an output which transitions from a high state to a low state when IR light is detected by the phototransitor. The output voltage is read at the terminal of the collector.

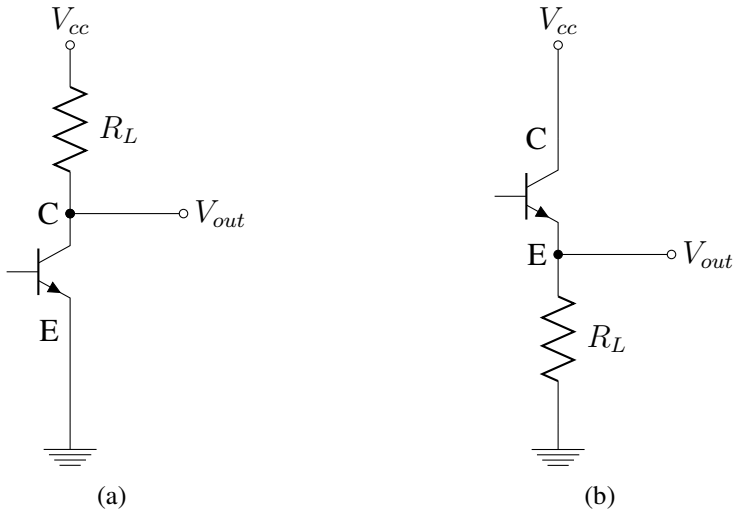

Figure 4.4: (a) The common-emitter amplifier, (b) the common-collector amplifier

On the other hand, the common-collector amplifier circuit, Figure 4.4(b), generates an output which transistions from a low state to a high state when IR light is detected by the phototransistor. The output voltage is read at the terminal of the emitter.

In both circuits, the phototransistor can be operated in either an active mode or a switch mode [1]. While in the active mode, the phototransistor output voltage is proportional to the amount of light received by the component until it reaches its saturation point. This mode of operation is not desirable for the purposes of a tachometer. If configured in switch mode, the phototransistor will

[1]It should be noted that the circuit types are for npn-type transistors, which are typical to phototransistors. If a pnp-type phototransistor is used, the voltage output will be exactly opposite that which was described for an npn-type phototransistor [1].

either be “off” or “on” (saturated) in response to the light. This mode of operation in useful for the purposes of a tachometer since the output voltage is more digital in nature. By adjusting the load resistor R_L in the circuit, the desired mode of operation can be set. The required value of the resistor for the desired mode can be determined using the following relations:

$$\begin{aligned} M_{active} &: V_{cc} > R_L i_{cc} \\ M_{switch} &: V_{cc} < R_L i_{cc} \end{aligned} \tag{4.1}$$

where M_{active} and M_{switch} denote the mode of operation (active or switch, respectively) and i_{cc} is the current across the resistor R_L. Typically, a resistor value of $5\text{k}\Omega$ or higher is adequate to operate in the switch mode. The “on” level voltage should be equal to the supply voltage and the “off” level voltage should be less than $1V$ [39].

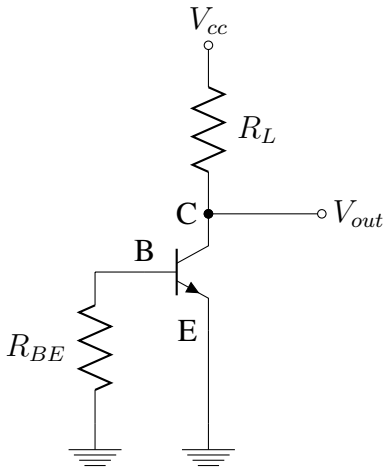

Figure 4.5: Common-emitter amplifier circuit with base-emitter connection

To further reduce the “off” level voltage and provide a more digital output, a high value base-emitter resistor R_{BE} can be incorporated into the circuit design, as shown in Figure 4.5. The addition of resistor R_{BE} prevents low light levels from triggering the phototransistor to the “on”

state. A complete circuit diagram for the non-contact tachometer is shown in Figure 4.6.

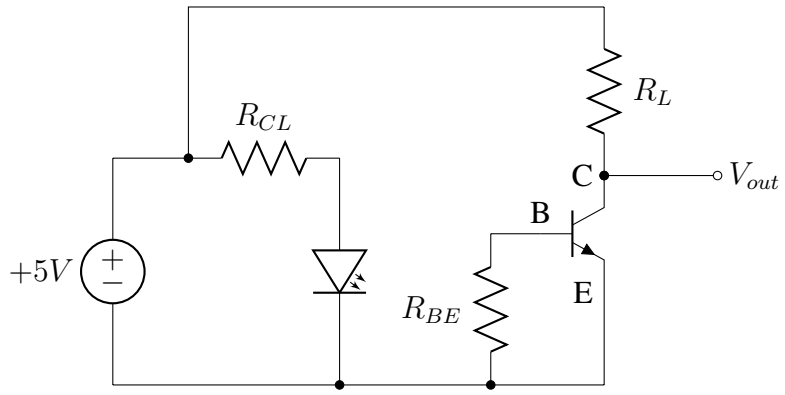

Figure 4.6: IR non-contact tachometer circuit diagram

The IR light source is an IR LED wired with a current limiting resistor R_{CL} to prevent burn-out due to the source current exceeding the maximum current rating of the LED. The phototransistor is wired parallel to the LED in the common-emitter configuration with a base-emitter resistor. When the rotor blade passes between the IR LED and the phototransistor, the voltage output level will transition from a high state to a low state, and the frequency of successively transitions is used to determine the angular rotation speed of the rotor.

Acquisition of phototransistor signals

The voltage signal generated by the phototransistor need to be captured by a computer for post-processing. To do this, a data acquisition (DAQ) system is used. The system consists of a DAQ box and DAQ software. There are many different DAQ boxes available from a multitude of manufacturers with a variety of connections and capabilities. Similarly, a great number of DAQ software packages are available. In order to reduce the likelihood of incompatibilities, a DAQ box from National Instruments was chosen, specifically the NI-USB 6008, shown in Figure 4.7.

Figure 4.7: National Instruments NI-USB 6008 DAQ box

National Instruments is one of the largest manufacturers of DAQ systems for academia, and they provide excellent driver support for their numerous hardware offerings. In choosing the appropriate DAQ, the constraint that needed to be satisfied was sampling speed. According to the Nyquist Sampling Theorem [11], in order to completely sample a signal, the sampling frequency needs to be at least twice as fast as the frequency of the signal to be signaled. Using simple dimensional analysis, we can determine the minimum sampling speeds the DAQ needs to have in order to successfully gather data. Assuming a worst-case scenario in which the three-bladed rotor spins at 10000 RPM:

$$10000\left(\frac{\text{revolutions}}{\text{minute}}\right)\times\frac{1}{60}\left(\frac{\text{minute}}{\text{second}}\right)\times 3\left(\frac{\text{samples}}{\text{revolution}}\right)\quad\Rightarrow\quad 500\,\frac{\text{samples}}{\text{second}}\tag{4.2}$$

Therefore, the DAQ must be able to sample at least 1000 samples per second in order to completely capture the signal in the worst-case scenario. According to the National Instruments website, at the time of writing, the NI-USB 6008 DAQ has a sufficiently high enough sampling speed. The basic specifications of the NI-USB 6008 DAQ box are outlined in Table 4.3 [23].

Table 4.3: Basic pertinent specifications for the NI-USB 6008 DAQ box

Specification	Parameter
Measurement Type	Voltage
Analog Input Resolution	12 bits
Analog Sample Rate	10 kS/s
Maximum Voltage Range	$\pm 10V$

With the DAQ box specified, we are left with choosing between two options for the DAQ software: LabVIEW or MATLAB. It was decided that MATLAB is the best option for several reasons. First, MATLAB is a familiar piece of software that won't pose any learning curves to using it. Second, MATLAB is very extensible and configurable. For the DAQ specified, MATLAB can be configured to use the manufacturer's drivers and also provides a Data Acquisition Toolbox which contains software tools to hook into the DAQ and capture data directly to the MATLAB workspace. The capability of capturing data directly to the workspace is very powerful since it eliminates the two step process of capturing data first in LabVIEW and then importing it into MATLAB for post-processing.

Angular velocity experiment test stand

A schematic experiment test stand is shown in Figure 4.8. The stand consists of two major components:

1. **Cantilevered beam assembly** which consists of the following subassemblies

   a) Riser – positions the rotor in the middle of the flow field and provides a sturdy support

   b) Cantilivered beam – positions the rotor away from the riser in order to reduce aerodynamic effects

c) Bearing block – allows the rotor to freely rotate and change its angle of incidence θ with respect to the flow field

2. **Sensor tower assembly** which consists of the following subassemblies

a) IR LED assembly – PCB containing IR LED and current limiting resistor

b) Phototransistor assembly – PCB containing phototransistor and load resistors

c) Adjustment post – allows positioning and clearance to accommodate various angles of incidence

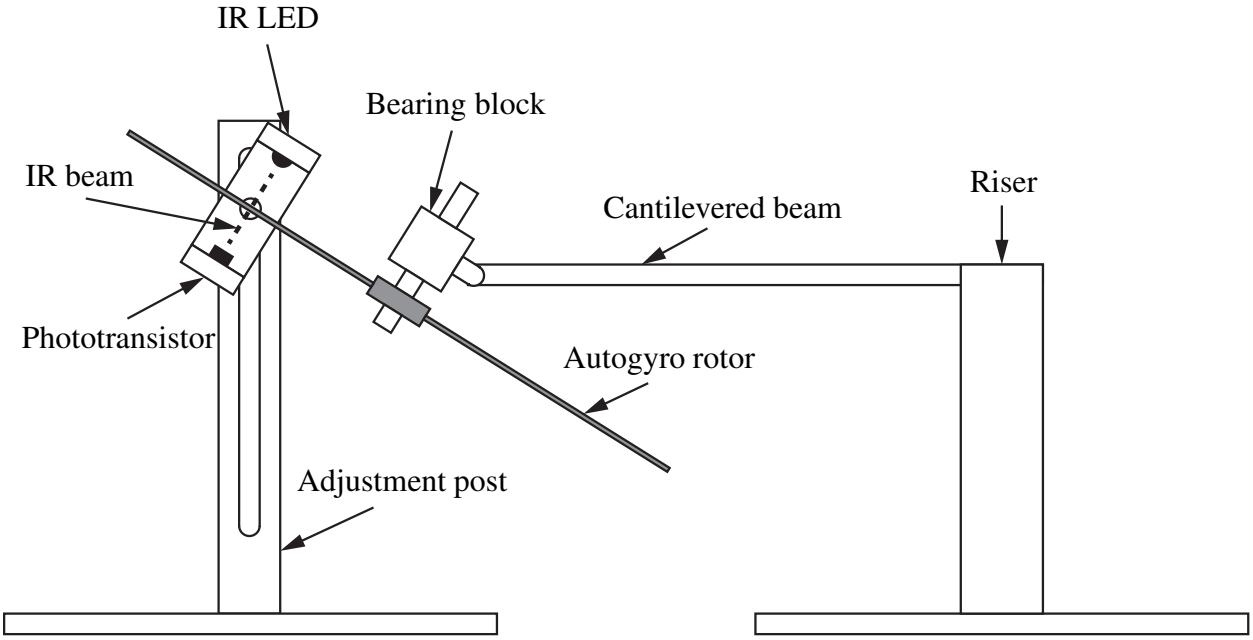

Figure 4.8: Angular velocity experiment test stand schematic

One of the important design criteria for this particular test stand is to design it in such a way that the phenomenon of *dynamic aeroelastic flutter*, or simply *flutter*, is avoided. Flutter is a dynamic instability of an elastic structure in a fluid flow and is caused by positive feedback between the elastic structure's deflection and the force exterted on it by the fluid flow [19]. Unless designed

otherwise, flutter can be a very destructive event, since the system begins to oscillate at one of its resonant frequencies. A famous example of flutter leading to catastrophic failure of a structure is the collapse of the Tacoma Narrows Bridge in late 1940. Due to the complex geometry of the cantilevered beam assembly, the length of beam which eliminates the threat of a flutter instability occuring for wind speeds which fall into the testing range (8-20 m/s) is determined through testing, rather than through theorectical calculations.

Angular velocity experimental procedure

The following procedure will be used to carry out the angular velocity experiment.

1. Position and secure the cantilevered beam and sensor tower assemblies in the wind tunnel.
2. Set desired angle of insidence θ and wind speed V_w.
3. Engage wind tunnel and allow it to reach steady-state.
4. Measure the exact wind speed V_w using Steps 3 and 4 from the wind tunnel characterization experiment.
5. Use MATLAB script `tachometer.m` to gather rotor angular velocity data.
6. Repeat previous steps for multiple angles of incidence and wind speeds.

The code for `tachometer.m` is available in Appendix A.

Thrust Force Experiment

A useful parameter to know about the autogyro rotor is the amount of thrust is produces, as the thrust is the primary component of the lift produced in the prescribed range of incidence angle of $20^\circ \leq \theta \leq 40^\circ$ (refer to Chapter 3). Since the mass of the autogyro rotor to be used is very low, accurately measuring the thrust force produced using a load cell or a cantilevered beam with strain gauges would be exceedingly difficult due to the high probability of unacceptable signal-to-noise ratios, oscillations, etc. Instead, another method of measurement was chosen.

The method chosen was very simple; the autogyro rotor would be allowed to levitate and its angle of incidence θ with the oncoming air would be decreased until the force of gravity $m_a g$ is equal to the lift force F_L. This critical angle on incidence θ_{crit} can be visually determined by observing the point at which the rotor starts to drop, or "lose altitude", in the wind tunnel. After determining the angle of θ_{crit}, the values of the thrust force T, lift force F_L, and the drag force F_D can be calculated.

Thrust force experiment test stand

As discussed earlier, due to the low mass and the expected low magnitude of forces to be generated by the autogyro rotor used for testing, a non-contact method of measuring position is desired. The setup consists of a polished and lubricated metal rod used to constrain the motion of the autogyro rotor to a chosen axis, and to make it possible to measure the critical angle of incidence θ_{crit}. A schematic of the setup used in experimentation is shown in Figure 4.9. The angle of the rod is slowly changed towards the vertical until the rotor moves from its initial configuration to its displaced configuration. At this point, $\theta = \theta_{crit}$ and $F_L = m_a g$. While the forces of friction cannot be entirely eliminated from the experimental setup, steps were taken to minimize the effects of

these forces. The rod was both polished to a smooth finish and lubricated with light oil, thereby reducing friction since the rotor rides on a thin film of oil rather than on bare metal.

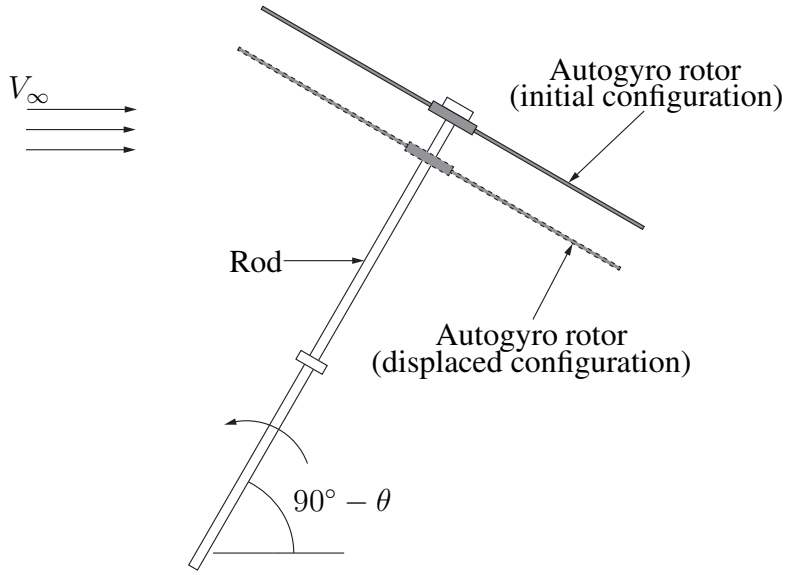

Figure 4.9: Non-contact position sensing experimental setup

Furthermore, the inside diameter of the rotor hub was also sanded to smooth in order to further reduce the influences of friction on the data gathered.

Using a free body diagram of the rotor in the displaced configuration, it is very simple to calculate the thrust force T, and by extension the lift and drag forces, F_L and F_D. Assuming a static equilibrium, we can then sum forces in the x-, y-, and y'-directions to find the relationship between all of the aerodynamic forces.

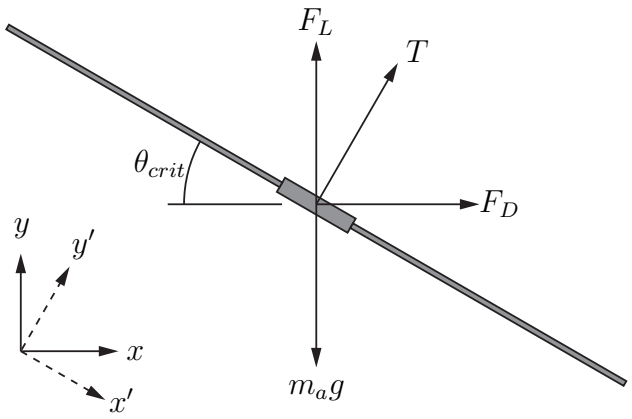

Figure 4.10: Displaced configuration free body diagram

After solving, we are left with the following expressions

$$T = \frac{m_a g}{\cos \theta_{crit}} \tag{4.3}$$

$$F_L = T \cos \theta_{crit} = m_a g \tag{4.4}$$

$$F_D = T \sin \theta_{crit} = m_a g \tan \theta_{crit} \tag{4.5}$$

Therefore, by measuring the critical angle of incidence θ_{crit}, the current wind speed V_w, and finding the weight of the autogyro rotor $m_a g$, we can find the thrust force T, the lift force F_L, and the drag force F_D at that wind speed.

Thrust force experimental procedure

The following procedure will be used to carry out the thrust force experiment.

1. Position the rod with the autogyro rotor attached inside the wind tunnel.

2. Open the wind tunnel aperture to its maximum separation and engage the wind tunnel blower motor.

3. Record the steady-state wind speed V_w.

4. Allow the rotor to spin up and reach steady state. Once the rotor is at steady state, it will be rotating while making contact with the upper shaft collar on the rod. This is considered the initial configuration of the autogyro rotor.

5. Slowly reduce the angle of incidence θ by bringing the rod towards the vertical.

6. When the autogyro is no longer making contact with the upper shaft collar, it is considered to be in its displaced configuration. Record the angle of incidence θ at which this configuarion is achieved.

7. Repeat the previous steps for multiple wind speeds.

8. After data collection is completed, use the MATLAB script `thrust_determination.m` to process the data.

The code for `thrust_determination.m` is available in Appendix A.

Conclusion

In this chapter, we discussed the design of the experiments performed for this thesis. First, we discussed the necessity to characterize the wind tunnel which will be used as the experimental test bed along with the technique to be used. Several options options for wind speed sensing were presented and a logical argument leading to the selection of the best option was provided. Finally, an experimental procedure to characterize the wind tunnel was presented. Next, a detailed discussion

about the development of a non-contact type tachometer was given. This discussion encompassed the design of the device from both a mechanical and electrical engineering standpoint. A detailed description of the circuity and the DAQ system was given in order to theoretically validate the design approach. Finally, the experimental procedure for acquiring the autogyro rotor's rotational velocity was given. The final experimental setup described was that of the thrust force determination rig. A detailed description of the physics used in designing the setup was shown, and equations for determining the desired aerodynamic parameters were derived. Finally, an experimental procedure for the thrust determination experimen was given. In the following chapter, we provide the experimental results from each of the experimental setups.

[

CHAPTER 5: EXPERIMENTAL RESULTS

This chapter contains all of the experimental data gathered from the experiments outlined and described in Chapter 4, as well as a discussion on the methods and reasoning used in processing the acquired data. Furthermore, this chapter describes in detail the autogyro rotor's airfoil and the reason why its particular profile was chosen over others.

Wind Tunnel Characterization

As discussed previously, before starting to collect aerodynamic data from the autogyro rotor, it is important to first characterize the wind tunnel which is to be used. This is done to get a good sense of the wind speed range available for use in experimentation as well as a safety precaution; excessively high wind speeds could damage equipment or blow it out of position and potentially damage the experiment or the wind tunnel itself.

Setting up the experiment

Photographs from the setup of this experiment are shown in Figure 5.1. Figure 5.1(a) shows the wind tunnel in its entirety. From left to right, we have the intake plenum, the test section, the aperture, and finally the puller assembly. Figure 5.1(b) shows the adjustment screw with which the wind speed is changed. The screw moves the wind tunnel puller assembly back and forth, closing or opening the gap of the aperture, thereby lower or increasing the wind speed. Figure 5.1(c) shows the HHF92A flow meter being used to record wind speed data from the wind tunnel. It should be noted that this is just a representative photograph.

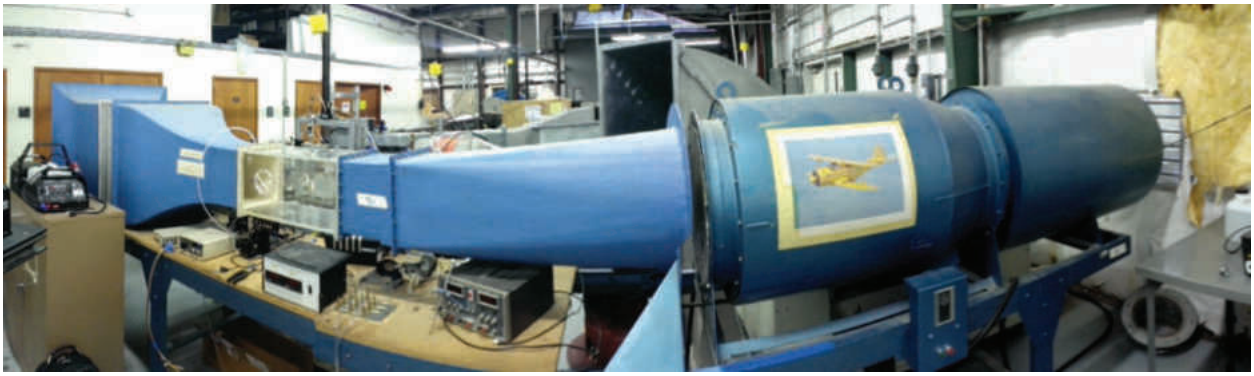

(a) Wind tunnel

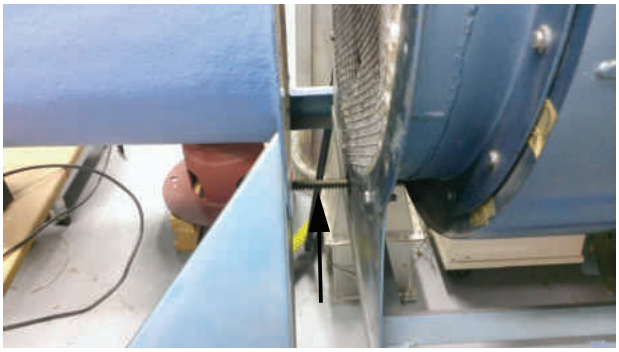

(b) Adjustment screw

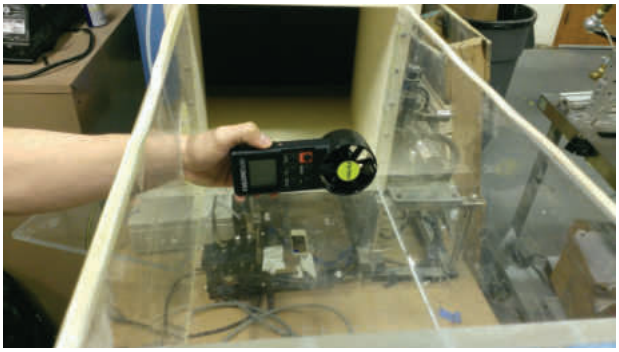

(c) Taking measurements

Figure 5.1: Wind tunnel characterization experiment photographs

During testing, the flow meter is inserted through a hole in the side of the wind tunnel test section and is positioned such that the wind vane portion of the meter is in the middle of the test section, oriented square to the flow field. It is important to plug the hole as effectively as possible in order to ensure that air escaping through the hole is kept to a minimum.

The following procedure was used to carry out the wind tunnel characterization experiment:

1. Fully close the wind tunnel aperture.

2. Engage the fan motor and allow the wind tunnel to achieve steady-state. The tunnel is assumed to be at steady-state once any sounds that can be related to start up transients die out.

3. Insert the handheld meter into the tunnel, positioning the weather vane portion in the center of the test section.

4. Use the min/max/avg function of the meter to record the average wind speed over 10 seconds.

5. Open the aperture by 0.5" and repeat the data gathering procedure. The experiment is concluded once the aperture is fully open.

Experimental data

The data from the characterization experiment was recorded and processed using MATLAB. Table 5.1 shows the raw data from the experiment.

Table 5.1: Wind tunnel characterization experiment data table

Separation (in.)	**Measurement** (m/s)
0.5	42.25
1.0	32.30
1.5	27.70
2.0	23.80
2.5	22.08
3.0	19.97
3.5	18.90
4.0	17.22
4.5	15.91
5.0	14.86
5.5	13.84
6.0	13.19
6.5	12.04
7.0	10.57
7.5	10.00
8.0	9.56
8.5	9.01

Each measurement carries an error of $\pm 3\%$ of the full scale, as per the HHF92A data sheet. After importing the raw data into MATLAB, `cftool`, from the MATLAB Curve Fitting Toolbox, was used to apply two different regression curves to the data. The functions chosen were a power fit and a rational function fit, or

$$\begin{aligned} \hat{f}_{power}(x) &= ax^b \\ \hat{f}_{rational}(x) &= \frac{a}{x+b} \end{aligned} \tag{5.1}$$

The rationale for choosing the power function was based on the assumption that the wind tunnel's speed follows *Bernoulli's principle*. From basic fluid mechanics, Bernoulli's principle states that, for an inviscid flow, an increase in the speed of a fluid is followed by a simultaneous decrease in fluid pressure or a decrease in the potential energy of the fluid [13]. Expressed mathematically,

$$\frac{1}{2}\rho v^2 + \rho g z + p = constant \tag{5.2}$$

Consider the control volume around the test section of the wind tunnel as shown in Figure 5.2.

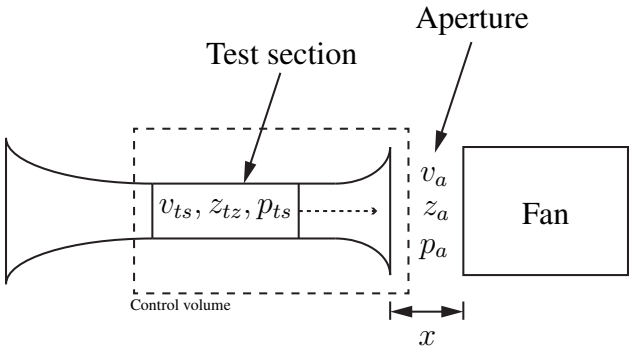

Figure 5.2: Control volume around wind tunnel test section

Following the streamline (dashed arrow) shown, we see that the potential energy of the flow is the same in the test section and at the aperture (*i.e.* $\rho g z_{ts} = \rho g z_a$). Therefore, the velocity in the test

section is

$$\frac{1}{2}\rho v_{ts}^2 + p_{ts} = \frac{1}{2}\rho v_a^2 + p_a \quad \Rightarrow \quad v_{ts} = \sqrt{v_a^2 + \frac{2(p_a - p_{ts})}{\rho}} \tag{5.3}$$

Intuitively, we see that the pressure at the aperture p_a is a function of the aperture separation distance x, so it stands to reason that

$$v_{ts} \propto p_a(x)^{1/2}, \quad p_a(x) \sim \frac{1}{x} \quad \Rightarrow \quad v_{ts} \propto \frac{1}{x^{1/2}} \tag{5.4}$$

meaning that we can expect a power function approximation to follow the recorded data reasonably well. From Eqs. (5.1) and (5.3), we see that the parameter a for the power approximation function is comprised of v_a^2, p_{ts}, and ρ.

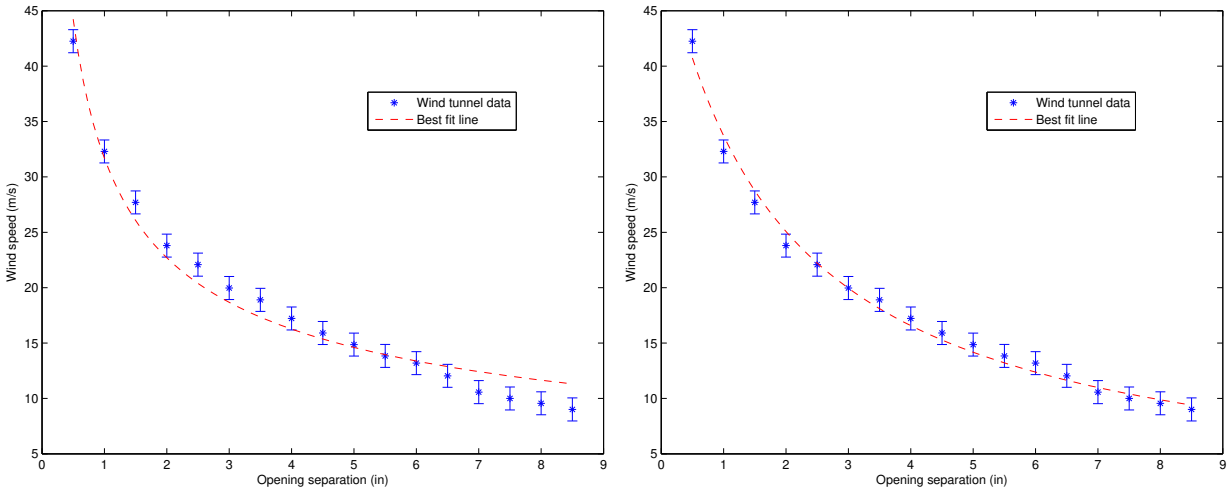

(a) Using a fit line of the form $\hat{f}(x) = ax^b$

(b) Using a fit line of the form $\hat{f}(x) = \frac{a}{x+b}$

Figure 5.3: Wind tunnel characterization data

Of immediate concern is that the parameter a seems to depend on v_a^2, which itself depends on $p_a(x)$. This means that the power function approximation is not necessarily the best, as shown in

Figure 5.3(a). Initially, the approximating function follows the data quite well, but then quickly starts to diverge. Towards the maximum aperture separation distance, the approximating function greatly overestimates the actual wind speed. The rational appromixation function was found to most accurately follow the recorded data. While the reason for this is not immediately apparent, it is possible that the rational function better approximates the interaction between v_a^2 and $p_a(x)$, as well as more complicated fluid mechanics effects such as changes in aperture pressure as a result of vortex shedding around the edge of the aperture, for example. The resulting rational function fit is shown in Figure 5.3(b). Table 5.2 summarizes the fit parameters of the two approximating functions as well as certain statstical properties of each fit.

Table 5.2: Approximating function paramters

Function	**a**	**b**	**R^2-value**
Power	31.69	-0.4812	0.9736
Rational	97.8	1.901	0.9917

As shown for the power approximating function, the exponent (parameter b) value found by MATLAB's `cftool` is very close to the value of $-\frac{1}{2}$, as predicted analytically by Bernoulli's principle, Eq. (5.4). As shown in the R^2-value column, and visually in Figure 5.3, it is confirmed that the rational approximating function is a better fit than the power approximating function.

The Experimental Autogyro Rotor

Before testing of the aerodynamic properties of the autogyro could commence, it was necessary to design and develop an autogyro rotor that was suitable for testing within a small scale, wind tunnel environment. A variety of manufacturing options were considered, but ultimately the decision was made to manufacture the rotor assemblies using *3D printing technology*. Three-dimensional print-

ing is an additive process, rather than a subtractive process like CNC machining where material is removed, since successive layers of material are deposited on a base layer, thereby building up a 3D finished product out of very thin "slices". Three-dimensional printing was chosen for a variety of reasons including:

1. **Cost effectiveness:** 3D printing, compared to more traditional techniques like CNC maching, is very affordable. A high-resolution, custom printed part can cost several orders of magnitude less than a part made using CNC. Additionally, since 3D printing is an additive process, material waste is significantly less.

2. **Time effectiveness:** 3D printing carries a slight edge in time of manufacture over CNC machining.

3. **Durability:** the various thermoplastics used in 3D printing are sufficiently strong enough to withstand wind tunnel testing. However, they are also weak enough to not cause damage to expensive testing components such as the wind tunnel, and various sensors and computers used in the data gathering process in the event of a catastrophic structural failure of the rotor.

Rotor assembly and blade geometry

As shown in Figure 5.4(a), the autogyro rotor assembly consists of two parts: the rotor hub and the flapping blades. The blades are attached to the hub with small diameter (0-80) UNC machine screws which provide hinges on which the blades flap. At the root of each blade there is a feature which constricts the blades to flap within a $\pm 10^{\circ}$ arc. Figure 5.4(b) shows a 3D printed prototype of the rotor used in wind tunnel testing. The blade tips are painted black in order to make them optically opaque in the IR spectrum; the IR spectrum is used in the rotor angular velocity experiment and any IR light leaking through the blades can degrade the quality of the data gathered.

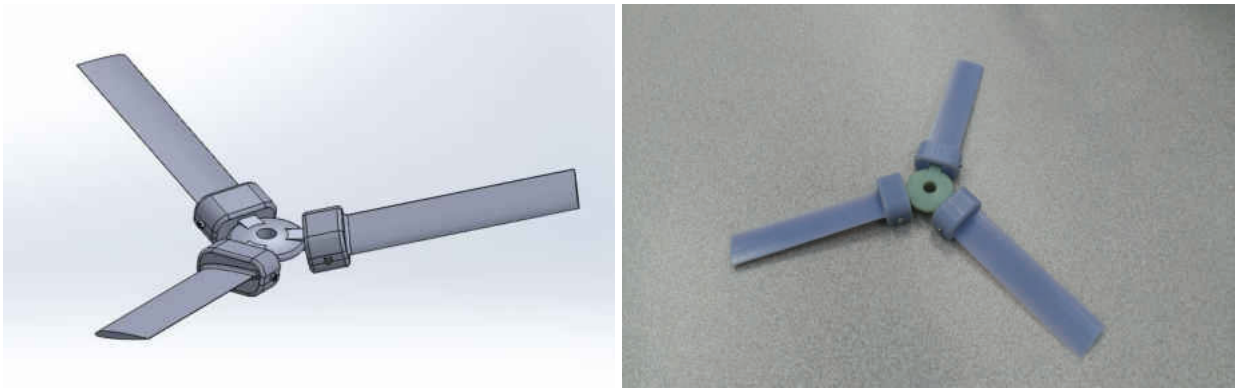

(a) 3D CAD model (b) 3D printed autogyro rotor

Figure 5.4: The experimental autogyro rotor

The airfoil profile chosen for the autogyro rotor was the NACA 23012 profile, shown in Figure 5.5. The coordinates for this airfoil section are freely available on the Internet from multiple sources [49, 48]. This profile was chosen over others since it develops a high maximum lift and has a low profile drag, in addition to possessing aerodynamic characteristics which are generally superior to those of other commonly used sections of small or medium camber and medium thickness [24].

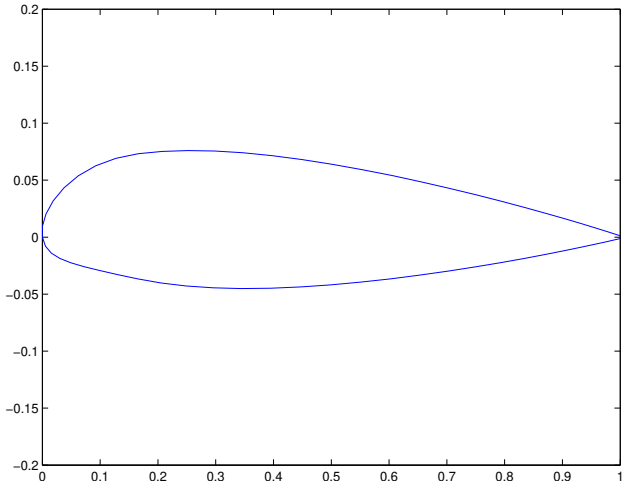

Figure 5.5: NACA 23012 airfoil profile

Table 5.3 shows the physical parameters of the printed autogryo rotor. These parameters influence the aerodynamic performance of the rotor, so it is crucial that the values are correctly calculated or measured.

Table 5.3: 3D printed autogyro rotor physical parameters

Parameter	**Value**
B	3
R	76.2 mm
W ($m_a g$)	0.226 N
c	19.1 mm
σ	0.239
δ	0.007
α	10°

The value of δ was obtained from the average profile drag over a range of Reynolds numbers as given in [24].

Angular Velocity Experiment

The angular velocity experiment was performed using the 3D printed autogyro rotor and the cantilevered beam test stand, as described in Chapter 5. The purpose of this experiment was to determine the relationship between the wind speed V_w, the angle of incidence θ, and the resulting rotor speed Ω.

Setting up the experiment

Photographs from the setup of this experiment are shown in Figure 5.6. Figure 5.6(a) shows a side profile view of all the equipment used in this experiment. A top down view is shown Figure 5.6(b).

The two assemblies are held in place inside the wind tunnel using a metallic adhesive tape. At sufficiently high wind speeds, the assemblies can be moved by the force of the oncoming flow and potential damage to the wind tunnel of the experimental setup can result.

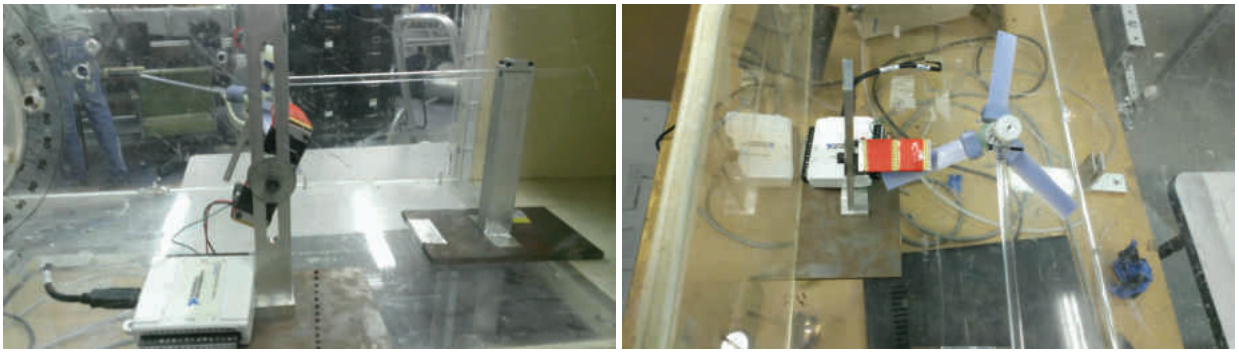

(a) Side profile view of entire setup

(b) Top view of entire setup

Figure 5.6: Angular velocity experiment photographs

The following procedure was used to carry out the angular velocity experiment:

1. Position and secure the cantilevered beam and sensor tower assemblies in the wind tunnel.
2. Set desired angle of insidence θ and wind speed V_w.
3. Engage wind tunnel and allow it to reach steady-state.
4. Measure the exact wind speed V_w using Steps 3 and 4 from the wind tunnel characterization experiment.
5. Use MATLAB script `tachometer.m` to gather rotor angular velocity data.
6. Repeat previous steps to multiple angles of incidence and wind speeds.
7. Condition and process data using `data_conditioning.m`.

The code for `tachometer.m` and `data_conditioning.m` is available in Appendix A.

Experimental data

The raw data caputured by `tachometer.m` is presented in Figure 5.7(a). Each "blip" represents a blade crossing in front of the photodiode and a break in the IR light beam. Since the rotor has three blades, every third pulse is considered one revolution. To find where the pulses occur in time, it is useful to automate the process since the number of pulses to count grows large as rotor speeds increase. To do this, the MATLAB `diff()` command was used. According to the MATLAB documentation files [21], `Y = diff(X)` calculates the differences between adjacent elements of $\vec{x}$ along the first array dimension whose size does no equal 1. If $\vec{x}$ is a vector of length m, then `Y = diff(X)` returns a vector of length $m-1$. The elements of $\vec{Y}$ are the differences between adjacent elements of $\vec{x}$, *i.e.*

$$\vec{Y} = \left[\vec{x}(2) - \vec{x}(1) \quad \vec{x}(3) - \vec{x}(2) \cdots \vec{x}(m) - \vec{x}(m-1)\right] \tag{5.5}$$

In a sense, what the `diff()` command is doing is calculating the approximate derivative of the data vector. To find where the pulses occur, we simply need to find the indices of the data vector after passing it through `diff()` where the value of the approximate derivative is positive.

If the data presented in Figure 5.7(a) is observed carefully, there is some noise at the low signal voltage and some artifacting at the high signal voltage. To eliminate these, it is desired to transform the raw signal to a *TTL signal*. A TTL, or transistor-transistor logic, signal can be thought of as a binary signal; either high or low. To perform this transformation, simple thresholding was used. If the signal is below a certain threshold value, it is sent to a prescribed low value, and vice versa. The result of this data conditioning procedure is shown in Figure 5.7(b). The difference between the raw and the conditioned data is slight, but it greatly aids in the second step of data processing, counting the pulses, by decreasing the liklihood of false positives being registered on account of signal noise. This second step is performed by another MATLAB function, `nnz()`.

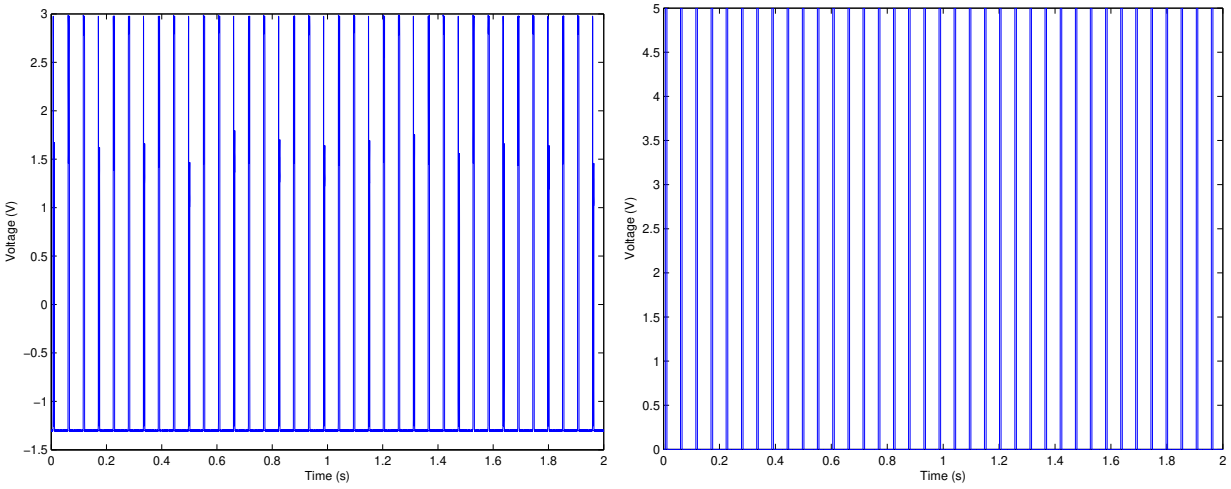

(a) Data prior to conditioning

(b) Data after conditioning

Figure 5.7: Sample `tachometer.m` data

According to the MATLAB documentation files [22], the command `n = nnz(X)` returns the number of nonzero elements of a matrix $\mathbf{X}$. The MATLAB script `data_conditioning.m` (refer to Appendix A) uses these two MATLAB commands to determine where in time the pulses have occured. The `diff()` command is nested within the `nnz()` command, along with some additional thresholding logic, in order to find all the occurences in the data vector where a positive change in slope has occured. The occurences, and their associated times, are then used to find the rotational velocity of the rotor. After determining the velocity of the rotor, the results are plotted and a line of best fit was determined using MATLAB's `cftool`, see Figure 5.8. The best fit line for all the cases presented is linear, *i.e.*

$$\hat{\Omega} = p_1 V_w + p_2 \tag{5.6}$$

Table 5.4 shows the values of the paramters m and b, as well as the R^2-value for each fit.

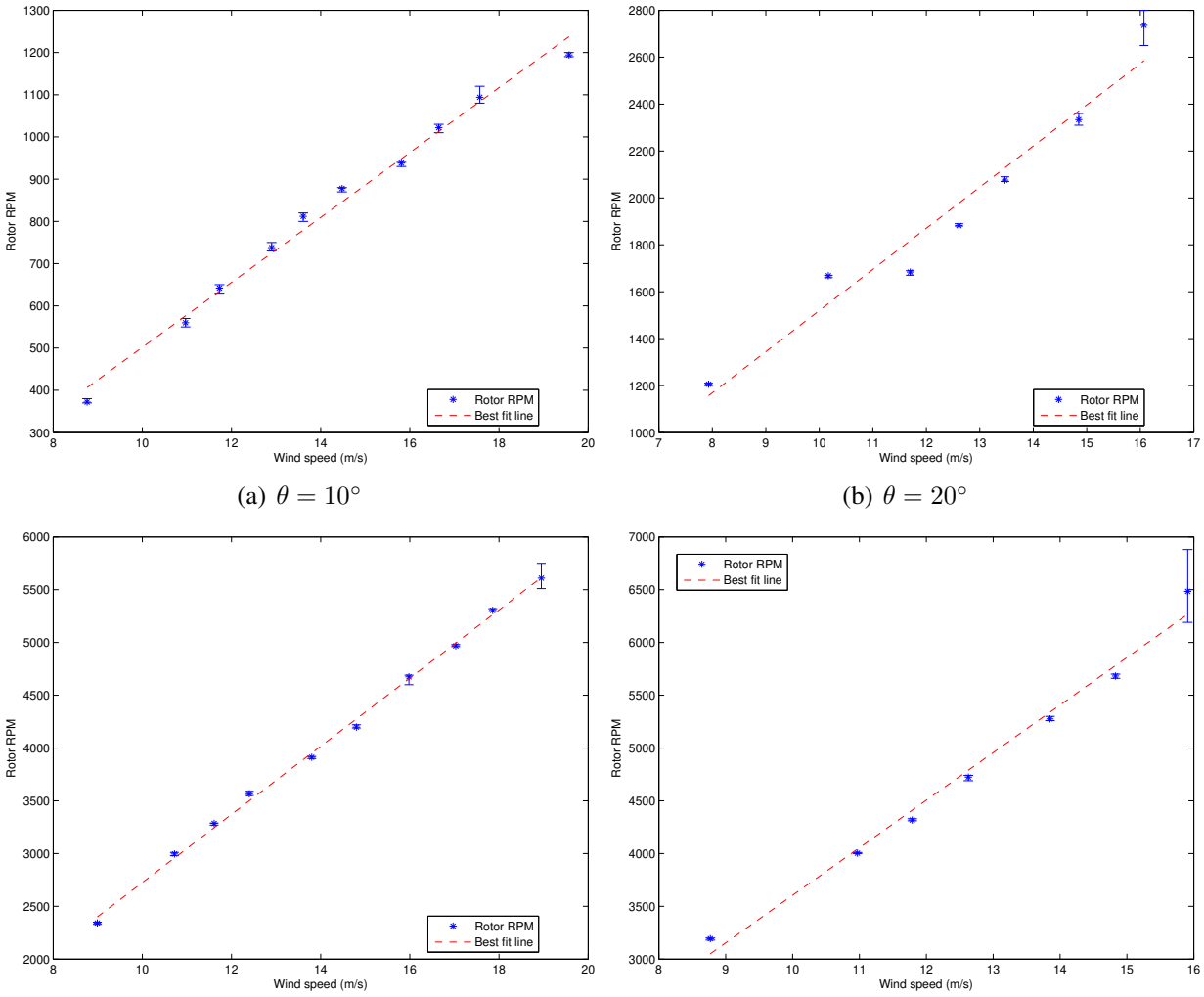

(a) $\theta = 10°$ (b) $\theta = 20°$

(c) $\theta = 30°$ (d) $\theta = 40°$

Figure 5.8: Rotor speed data as a function of angle of incidence θ and wind speed V_w

Table 5.4: Rotor speed best fit line parameters

Angle θ	$\mathbf{p_1}$	$\mathbf{p_2}$	$\mathbf{R^2}$**-value**	$\mathbf{V_{w,min}}$ (m/s)
10°	76.89	-267.2	0.9897	3.48
20°	175.4	-234.1	0.9526	1.33
30°	322.8	-502.5	0.9979	1.57
40°	450.6	-901.5	0.9869	2.00

Additionally, Table 5.4 outlines a rough estimate of the mininum wind speed required for the rotor to start turning for a given angle of incidence θ. This value was obtained as

$$V_{w,min} \approx \left| \frac{p_2}{p_1} \right| \tag{5.7}$$

The resulting minimum required wind speeds are plotted in Figure 5.9.

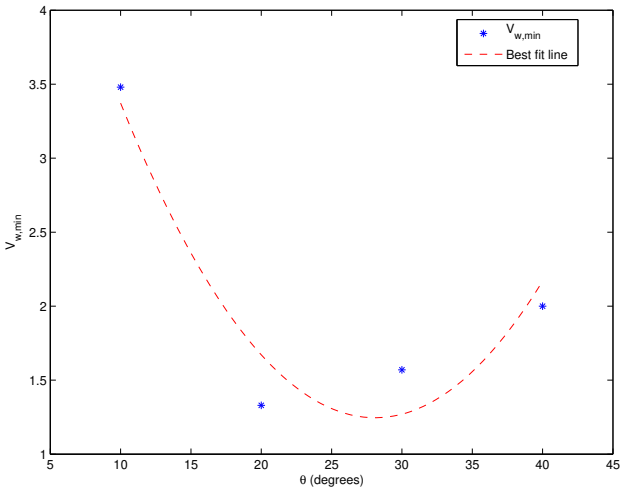

Figure 5.9: Minimum required wind speed

The data has a quadratic polynomial as a line of best fit. As calculated by `cftool`, the equation is of the form

$$\hat{V}_{w,min} = 0.0065\Omega^2 - 0.3651\Omega + 6.3730 \tag{5.8}$$

and it carries an R^2-value of 0.9176. If we solve Eq. (5.8) for its minimum by differentiating once and solving for Ω, we find that the minimum of the approximating function occurs at $\theta = 28.1°$. This value of θ serves as a rough estimate of the angle of incidence which corresponds to the lowest required wind speed needed to impart a sufficiently large amount of aerodynamic torque

on the rotor and have it start autorotating. If we combine the individual lines of best fit shown in Figure 5.8, we can generate a surface that visually illustrates the relationship between V_w, θ, and Ω, as shown in Figure 5.10.

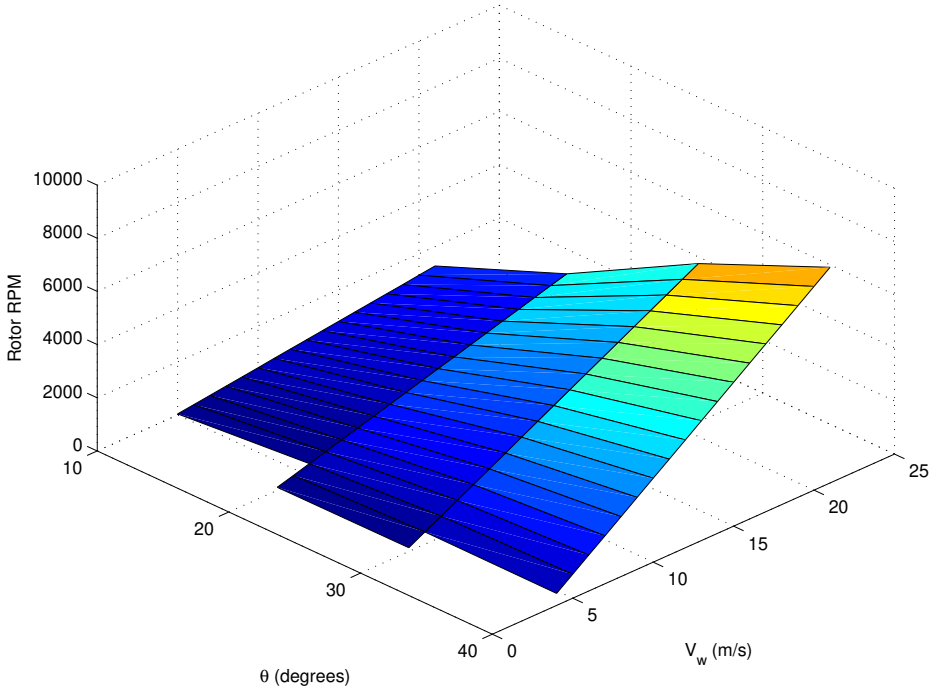

Figure 5.10: Rotor RPM surface as a function of V_w and θ

Using the MATLAB function `fit()`, we can find a surface of best fit for the data. A MATLAB m-file `RPM_surface_fit.m` was written to make use of the `fit` function. The approximating equation for the surface was found to be

$$\hat{\Omega}(V_w, \theta) = -107.5 - 4.313\theta - 60.71V_w - 0.348\theta^2 + 12.69\theta V_w \tag{5.9}$$

The fitted surface is shown in Figure 5.11, and carries an R^2-value of 0.9984. The benefit of Eq. (5.9) is that is can be used as part of a lookup table for an actual implementation of an autogyro-based aircraft, like the one shown in Figure 3.6. It should be noted, however, that this equation can

only be safely used for a rotor with the parameters outlined in Table 5.3. Any change in the rotor parameters would require testing to confirm whether or not Eq. (5.9) holds.

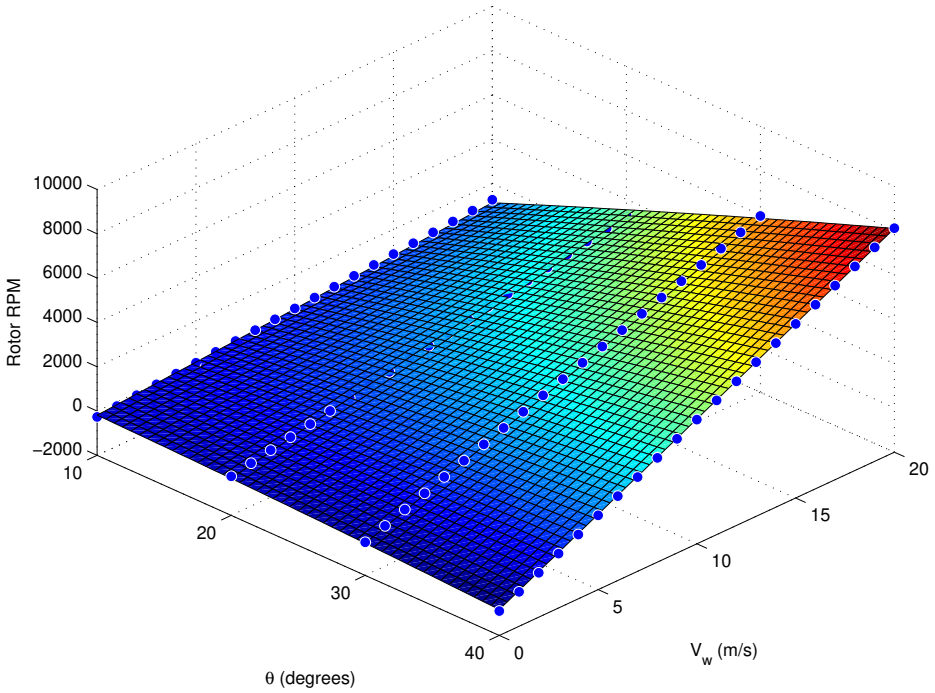

Figure 5.11: Rotor RPM fitted surface with data points from Figure 5.10

The Dangers of Aerodynamic Flutter Instabilities

As mentioned in Chapter 4, aerodynamic flutter can be a potentially destructive, positive feedback phenomemon. Flutter was unintentionally encountered while the use of the cantilevered beam for measuring aerodynamic forces was being explored. An initial proof of concept was proposed to see whether the rotor has enough lift capacity to generate a visually noticable amount of displacement from rest at the free end of the cantilevered beam.

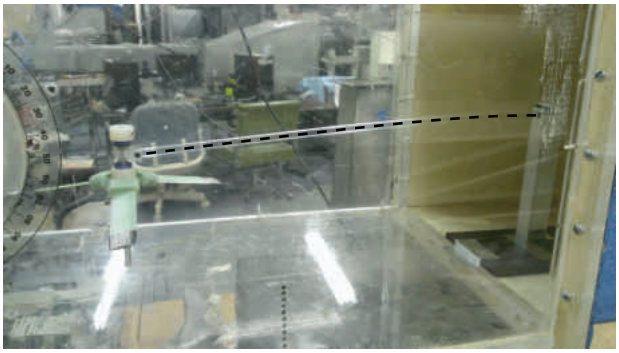

(a) Initial droop (cantilevered beam dashed for added clarity)

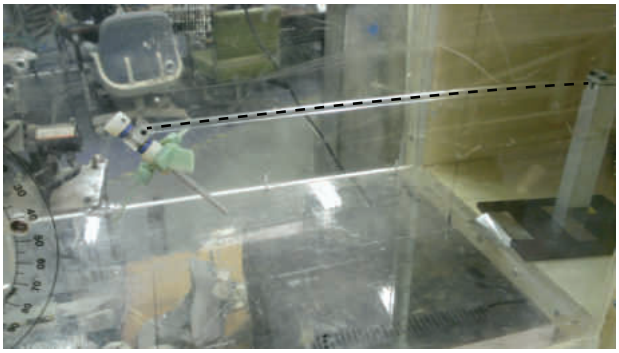

(b) After flutter instability (cantilevered beam dashed for added clarity)

(c) Remnants of the autogyro rotor

Figure 5.12: Pre- and post-aerodynamic flutter instability occurrence

The thinking was that if the displacement amount is visible, then strain gauge rosettes could be used to calculate the force at the free end of the beam from a strain measurement at the fixed end. Due to the combined weight of the rotor, rotor shaft, and bearing block, there was a sizeable initial droop in the beam, as shown in Figure 5.12(a). Soon after the wind tunnel was engaged and the rotor started spinning, the beam started oscillating wildly. It is hypothesized that the initial conditions of the beam, the wind speed setting of the wind tunnel, and the aerodynamic properties of the entire cantilevered beam assembly lead to the beam assembly hitting an unstable aerodynamic

flutter mode. Due to the violence of the oscillations, the bearing block started to rotate about its hinge and it was only a matter of time before the disk of rotation of the rotor interfered with the cantilevered beam. After the impact with the beam, the rotor blades suffered irreparable damage, Figure 5.12(b) and (c).

Thrust Force Experiment

The thrust force experiment was performed using the 3D printed autogyro rotor and the axis of motion constraining rod test stand, as described in Chaper 4. The purpose of this experiment was the determine the relationship between the wind speed V_w, the angle of incidence θ, and the resulting thrust force T, along with the lift force F_L and drag force F_D.

Setting up the experiment

The setup procedure for this experiment was very simple. The wind tunnel provides a cutout at the bottom of the test section which is typically used for mounting a load cell for characterizing airfoils. By simply removing the load cell and installing the rod with the autogyro rotor mounted, the experiment can be correctly positioned within the wind tunnel. A photograph of the test stand mounted in the wind tunnel is shown in Figure 5.13. The following procedure will be used to carry out the thrust force experiment.

1. Position the rod with the autogyro rotor attached inside the wind tunnel.
2. Open the wind tunnel aperture to its maximum separation and engage the wind tunnel blower motor.
3. Record the steady-state wind speed V_w.

4. Allow the rotor to spin up and reach steady state. Once the rotor is at steady state, it will be rotating while making contact with the upper shaft collar on the rod. This is considered the initial configuration of the autogyro rotor.

5. Slowly reduce the angle of incidence θ by bringing the rod towards the vertical.

6. When the autogyro is no longer making contact with the upper shaft collar, it is considered to be in its displaced configuration. Record the angle of incidence θ at which this configuarion is achieved.

7. Repeat the previous steps for multiple wind speeds.

8. After data collection is completed, use the MATLAB script `thrust_determination.m` to process the data.

The code for `thrust_determination.m` is available in Appendix A.

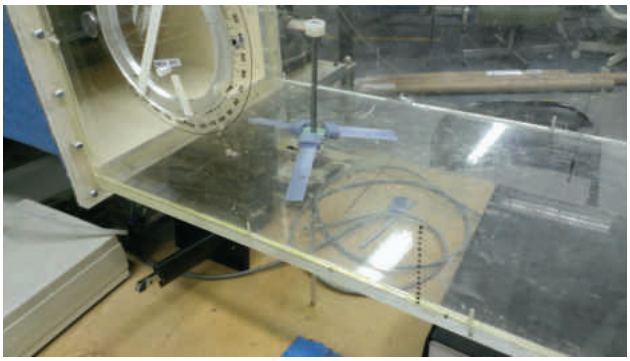

Figure 5.13: Thrust determination experiment photograph

Experimental data

The raw data captured during the experiment is presented in Figure 5.14. It shows the correlation between the wind speed V_w and the ensuing critical angle of incidence θ_{crit}. Intuitively, as the wind speeds increase, θ_{crit} tends towards zero since the inflow ratio μ is sufficiently high enough to maintain the autorotation state. At lower wind speeds, θ_{crit} must be larger in order to ensure that μ is large enough.

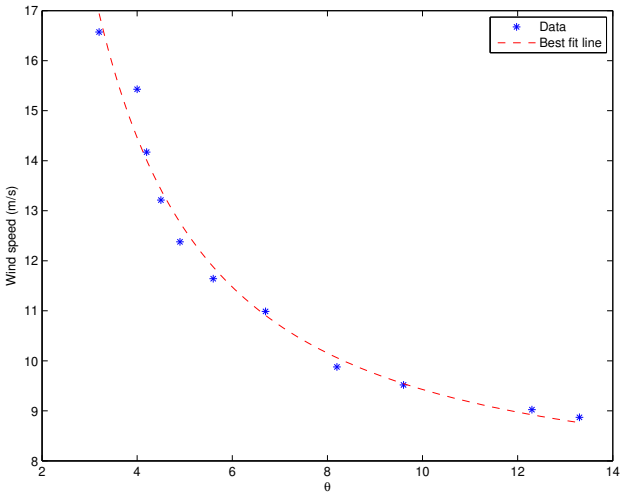

Figure 5.14: Thrust determination experiment raw data

Using MATLAB's `cftool`, a line of best fit was determined for the data set. It was found that a two term power function of the form shown in Eq. (5.10) provided the best fit. It is of the form

$$\hat{V}_w = 45.63\theta^{-1.34} + 7.341 \tag{5.10}$$

The best fit line carries an R^2-value of 0.9797. The raw data presented is summarized in Table A.1 in Appendix A. Using Eqs. (4.3)-(4.5), the MATLAB script `thrust_determination.m`, the weight parameter $m_a g$ listed in Table 5.3, and the data in Table A.1, the thrust force T, lift force

F_L, and drag force F_D are calculated. The results are presented in Figure 5.15.

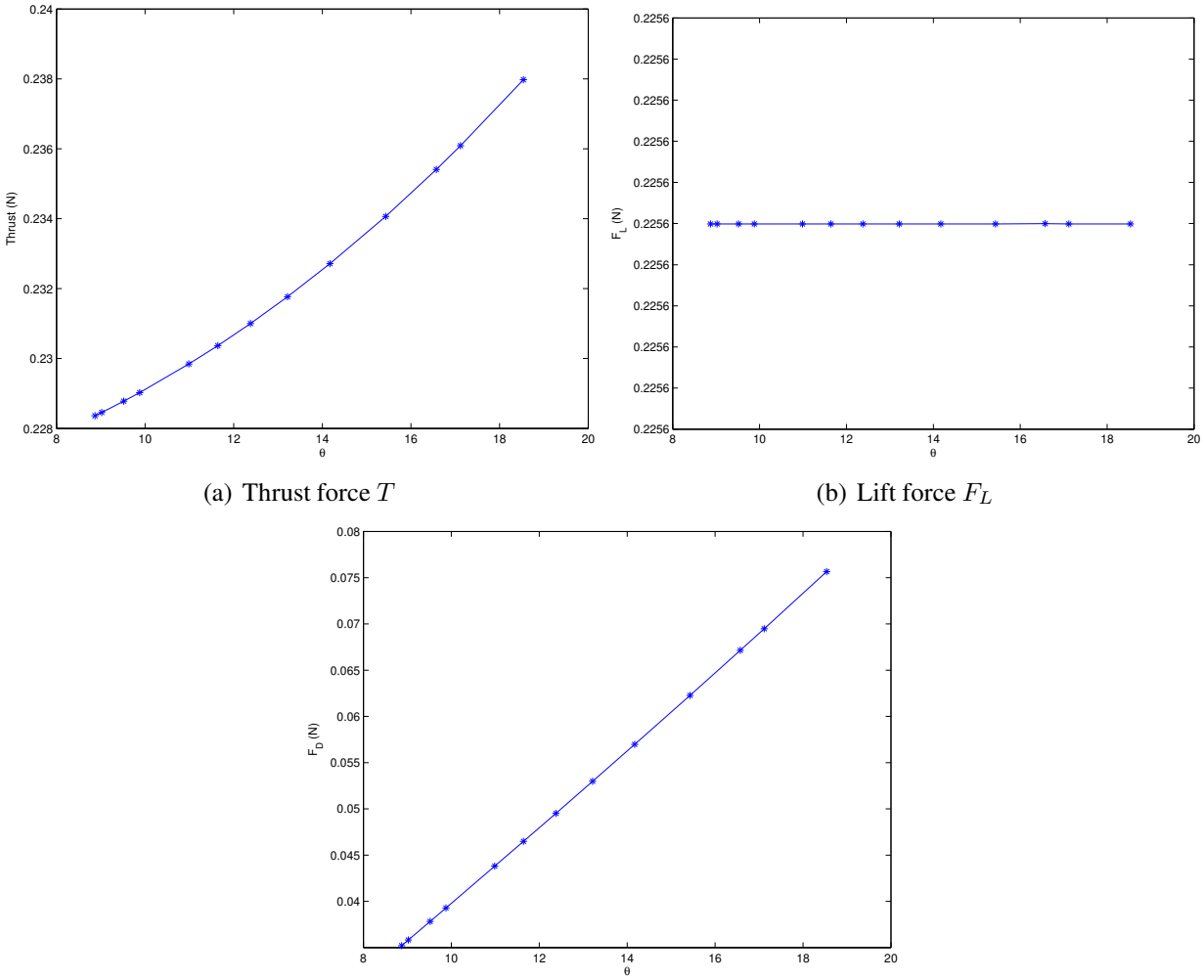

(a) Thrust force T

(b) Lift force F_L

(c) Drag force F_D

Figure 5.15: Aerodynamic characterization data

Limit cycle-like behavior at high wind speeds

An interesting observation was made during the experimentation procedure. When the wind speeds were sufficiently high ($>$14 m/s), the autogyro began exhibiting limit cycle-like behavior. A limit cycle is a closed trajectory in the phase space with the property that at least one other trajectory

spirals into it as time $t \to \pm\infty$ [20]. A classic example of a system exhibiting is the van der Pol oscillator. The van der Pol oscillator is expressed mathematically as

$$\frac{d^2x}{dt^2} - \gamma\left(1 - x^2\right)\frac{dx}{dt} + x = 0 \tag{5.11}$$

In state space, Eq. (5.11) can be written as

$$\begin{bmatrix} \dot{x} \\ \dot{y} \end{bmatrix} = \begin{bmatrix} y \\ \gamma\left(1 - x^2\right)y - x \end{bmatrix} \tag{5.12}$$

Plotting the behavior of the oscillator in the state space for various initial conditions shown the limit cycle present for the system, Figure 5.16.

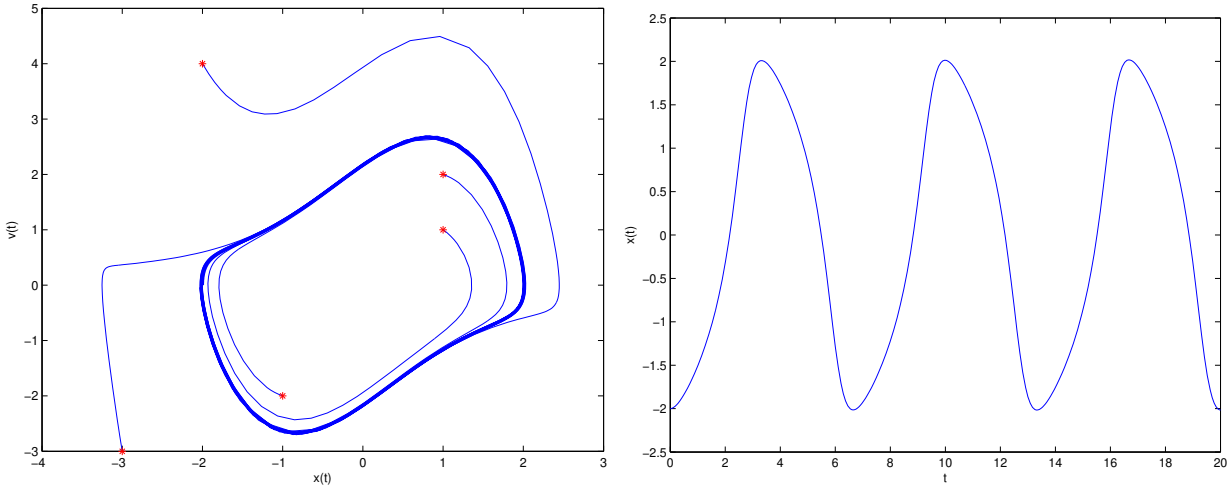

(a) Stable limit cycle with $\gamma = 1$ (limit cycle in bold)

(b) Displacement for $(x_0(t), v_0(t)) = (-2, 0)$

Figure 5.16: Behavior of the van der Pol oscillator

It is not certain whether the behavior exhibited by the autogyro was a true limit cycle, hence it was deemed limit cycle-like. The oscillatory motion of the autogyro along the rod was recorded and images representative of the motion are shown in Figure 5.17.

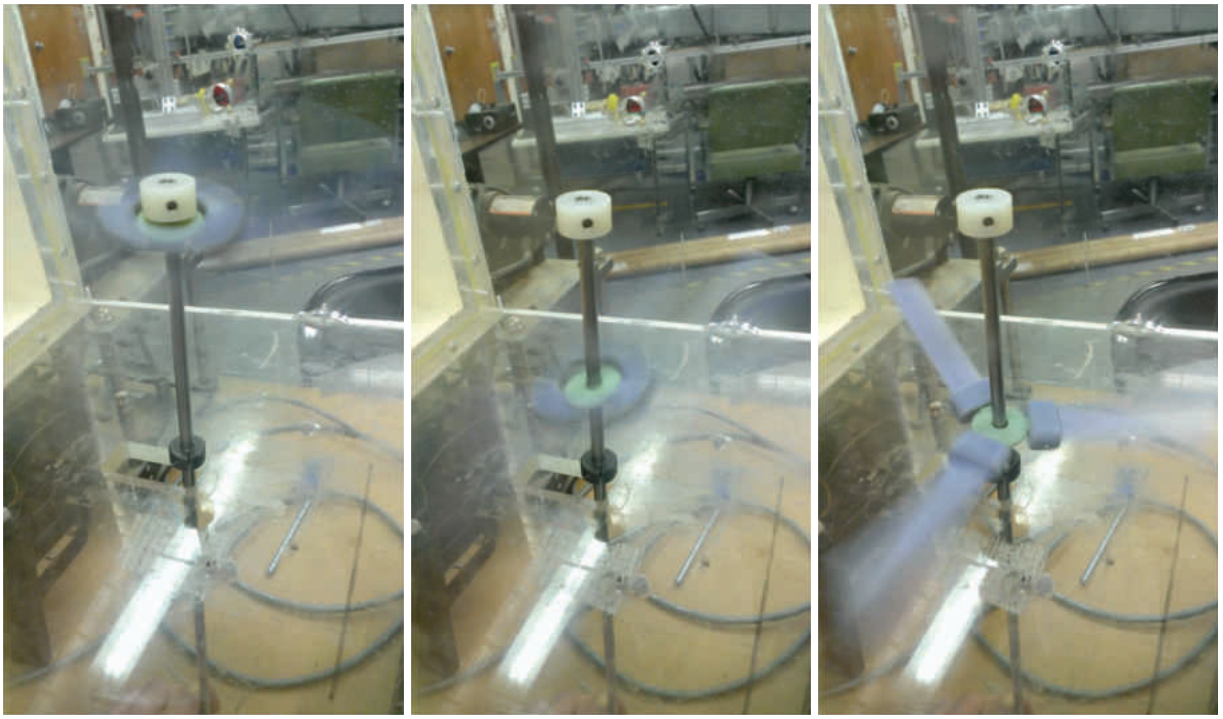

(a) $T = k_1 m_a g \cos\theta, k_1 > 1$ (b) $T = k_2 m_a g \cos\theta, k_2 < 1$ (c) $T = 0$

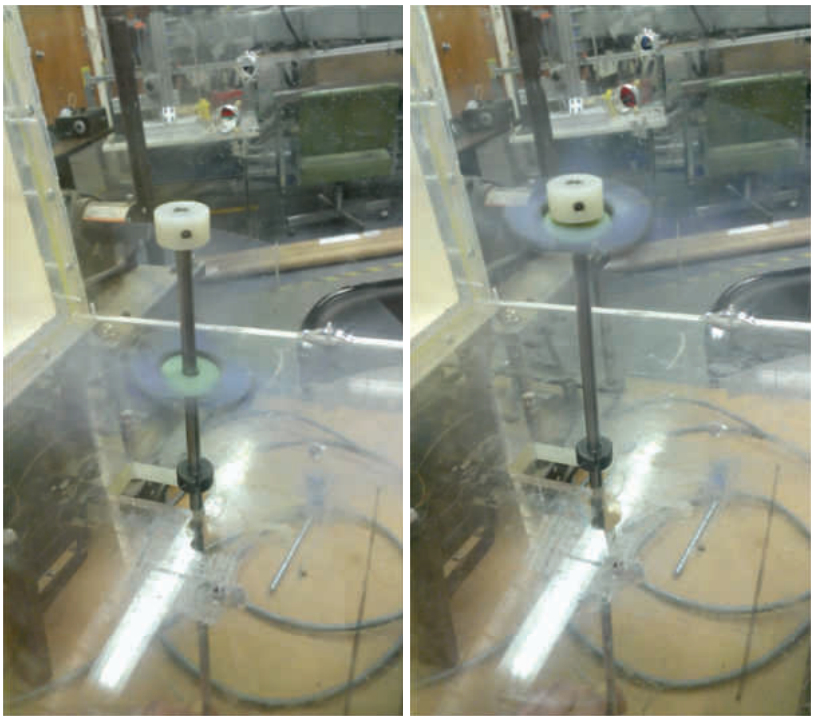

(d) $T = k_3 m_a g \cos\theta, k_1 > k_3 > 1$ (e) $T = k_1 m_a g \cos\theta, k_1 > 1$

Figure 5.17: Limit cycle-like behavior of the autogyro rotor

While the exact cause of the limit cycle-like behavior is not exactly known, a reasonable hypothesis is the following:

1. The rotor enters a state of autorotation and travels along the rod until it comes into contact with the upper shaft collar. At this point, $T > m_a g \cos\theta$.

2. As the rotor spins while making contact with the upper shaft collar, kinetic energy is slowly being dissipated as heat via the force of friction. As a result, the angular velocity Ω, and therefore thrust, decreases. At this point, $T \to m_a g \cos\theta$.

3. After enough kinetic energy has been disspated, the rotor is no longer spinning fast enough to produce sufficient thrust to keep it aloft. As a result, the rotor begins to travel down the rod. At this point, $T < m_a g \cos\theta$.

4. After the rod travels all the way down the rod, it comes to rest on the bottom shaft collar. At this point, $T = 0$.

5. The oncoming wind starts to turn the rotor, and the rotor's angular velocity increases. After it's spinning fast enough, the rotor begins to travel upwards along the rod. At this point, $T > m_a g \cos\theta$.

6. At this point, the cycle repeats.

Conclusion

In this chapter, we discussed the results of the experiments outlined in Chapter 4 and several observations that were made during the course of experimentation. First, wind speed data was taken from the wind tunnel and a mathematical characterization was found. It was determined that while sufficiently accurate, the speed of the wind tunnel did not rely wholly upon the separation

of the test section from the blower motor, but that additional, more subtle aerodynamics effects are at play. However, the mathematical characterization was deemed sufficiently accurate for the purposes of the experiments performed. Key findings of the experiments include a relationship between the wind speed V_w, the angle of incidence θ, and the resulting rotational velocity Ω. It was found that a a roughly linear relationship exists between V_w and Ω for fixed values of θ. The individual results were then merged into a surface and an approximating surface was fit to give the rotational velocity $\Omega = \Omega(V_w, \theta)$. Additionally, a relationship between the thrust force T, the angle of incidence θ, and the wind speed V_w was found. An interesting result in the form of limit cycle-like behavior was also uncovered. The phenomenon was documented and a possible explanation of the cause was provided. Additional research is required in order to better understand this oscillatory behavior.

CHAPTER 6: CONCLUSIONS

This thesis outlined the initial experimental initiative to get a firmer grasp on the dynamic properties of the autogyro rotor with the end goal of developing an airborne wind energy device based upon the autogyro phenomenon. The research leading up to the formation of the autogyro AWED concept was first presented, starting with tethered airfoils for wind energy extraction followed by a theoretical study of autorotation to establish viability of this approach. In the second half of the thesis, the experimental methodology and results were presented

Summary of Experiments and Results

Initial efforts involved fabrication of a flapping-blade autogyro rotor using 3D printing technology, followed by the development of the various test stands and an investigation into appropriate senors and data acquisition methods. Multiple characterization and data gathering experiments were conducted. Specifically, the performance of the wind tunnel available for testing was characterized, the relationship between the wind speed V_w, the angle of incidence θ, and the rotational velocity Ω of the autogyro rotor was determined, and a relationship between the thrust force T, wind speed V_w, and critical angle of incidence θ_{crit} was found. During the course of experimentation, a limit cycle-like behavior was discovered for when wind speeds were high and θ_{crit} was small. The exact physics of the phenomenon are unknown, but a hypothesis of the underlying cause and effect was proposed.

Recommendations for Future Research

While gathering data, several improvements were determined that could potentially increase the value and accuracy of the data gathered from the experimental setups. One of the primary improvements which can be done in order to improve this research is a shift away from small-scale testing closer towards larger scale testing. A drawback of testing small-scale devices withing a powerful wind tunnel like the one used to conduct this research is the degredation of signal to noise ratios as well as an unrealistic response of the system to driving forces (in this case, the force imparted onto the system by the oncoming air). There are two main factors of this unrealistic response:

1. The experimental autogyro rotor used in this effort, being very light in comparison to the force of the oncoming air, was overpowered by the wind and hence some performance characteristics intrinsic to the autogyro effect could be lost.

2. Since the 3D printed autogyro rotor is small (a consequence of the contraints imposed by the available testing facilities), the blades act more like a thin plate rather than an airfoil. Therefore, any advantages gained by using an airfoil section are partially lost due to the magnitude of the aerodynamic forces that can be attributed to them being negligible in comparison to those brought about by the thin plate forces.

Both of the above issues can potentially be solved by finding (or building) a larger test facility. The wind tunnel available for testing had a test section are of 12"$\times$12". If the area were much larger, a larger autogyro rotor model could be used. Since the rotor is larger, the magnitude of the force imparted on it by the oncoming air is relatively smaller and therefore hereto unmeasured performance characteristics can be discovered. Also, as the autogyro model is increased in size, the aerodynamics effects of a proper airfoil section will become more apparent. Another possible addition for experimentation with a larger autogyro rotor could be the inclusion of a generator. This

would allow testing the concept of using the autogyro for energy harvesting purposes. Performing the energy extraction tests could lead to a better understanding of the energy conversion efficiency surface, similar to that of wind turbines. As a result, a pseudo-Betz limit for the autogyro could be experimentally derived. Finally, with a larger wind tunnel, the *minimum* wind speeds that are possible to be generated could be lower, allowing for experimentation in flight regimes where stall is imminent. Furthermore, startup transients can be investigated.

Another improvement would be the fusion of the test setups into one in order to attempt to relate the two datasets presented in this thesis. By incorporating a tachometer into the thrust determination experimental setup, a deeper insight into the relationship between the rotational speed Ω and the thrust force T can be found. Additionally, the limit cycle-like behavior observed can be investigated further to see if there is a deeper relationship between the thrust force and rotational velocity. A further improvement would be the implementation of a sensor which is capable of measuring the flapping angle β of the blades over the course of one revolution. The harmonic motion of the flapping is important to the overall dynamics of the autogyro, but we were unable to measure it with our current experimental setups.

A final addition to the scope of this research would be the derivation and verification of a dynamic model of the autogyro. The research presented in this thesis is of a highly dynamic nature and the models presented in literature are only valid at steady-state. A dynamical description of the autogyro could lead to computer simulations of various items of interest, such as the performance of the rotor while it's being used for energy harvesting mode, its response to changes in wind speed, and ultimately, a full-system simulation of the quadrotor-based autogyro AWED. The experimental results could be used to further validate the dynamic model, and results from the simulations could ultimately tested on a full-scale representation of the overall system.

APPENDIX A: MATLAB SOURCE CODE

Tachometer Data Acquisition Code

```
%% TACHOMETER CODE (tachometer.m)

close all
clear data time data_save
clc

% Using the Data Acquisition Toolbox with NI DAQmx drivers
% Get list of devices
devices = daq.getDevices;

% Create a DAQ session s
s = daq.createSession('ni');

% NI USB-6008 DAQ box has the name Dev1
% Create an analog input on A0 channel in session s
% And set the scan rate (sample rate) at 10000 samples/sec
s.addAnalogInputChannel('Dev2', 0, 'Voltage');
samplingRate = 10000;
s.Rate = samplingRate;

% Set iteration number and sampling time duration
% Define storage vectors for data and time
iterations = 5;
duration = 2;
data_save = zeros(iterations, duration*samplingRate);
time_save = zeros(iterations, duration*samplingRate);
```

```
for i = 1:iterations

    % Set the input scan type and duration
    data = s.inputSingleScan;
    s.DurationInSeconds = duration;

    %Focus MATLAB's attention on DAQ session s
    %Create a foreground task to log data and time into a vector
    s;
    [data,time] = s.startForeground;
    data_save(i,:) = data(:);
    time_save(i,:) = time(:);

    figure
    plot(time,data)

    clear data time

end

% Count pulses from each sampling interval
% Use the nnz() and diff() commands to accomplish this
pulses = zeros(1,iterations);

for i = 1:iterations

    % Apply a 10% buffer to the minimum of the data vector
    % This is to remove any potential false positives for pulses
    % This method works by first finding any changes in the data vector
    % greater than one (i.e. it finds the peaks) using the diff() command,
    % then it sums the number of non-zero elements of the resulting vector
```

```
    % using nnz(), thus giving the total number of pulses
    pulses(i) = nnz(diff(data_save(i,:)+0.10*abs(min(data_save(i,:)))>1)>0)...
        ;

end

% Find the minimum, average, and maximum values of the pulses vector
minimum = min(pulses);
maximum = max(pulses);
average = mean(pulses);

% Calculate minimum, maximum, and average RPM values
% Calculate RPM by finding pulse frequency and multiplying by 20 (one
% revolution per 3 pulses, multiplied by 60 seconds)
RPM_min = ((minimum/duration)/3)*60;
RPM_max = ((maximum/duration)/3)*60;
RPM_avg = ((average/duration)/3)*60;

% Convert RPM values to rad/sec
Omega_min = RPM_min*(pi/180)/60;
Omega_max = RPM_max*(pi/180)/60;
Omega_avg = RPM_avg*(pi/180)/60;

% Prompt user to input wind speed and angle of incidence
% These values are used for filename generation and TSR calculations
prompt = 'Input Wind Speed (m/s): ';
windspeed = input(prompt);

prompt2 = 'Input Angle (degrees): ';
theta = input(prompt2);
```

```
% Radius of rotor disc, in meters
R = 0.0762;

% Calculate the tip-speed ratio
TSR_min = windspeed/(Omega_max*R);
TSR_max = windspeed/(Omega_max*R);
TSR_avg = windspeed/(Omega_avg*R);

filename = ['windspeed_',num2str(windspeed*100),'_theta_',num2str(theta),'...
    .mat'];
save(filename,'time_save','data_save','RPM_min','RPM_max','RPM_avg','...
    TSR_min','TSR_max','TSR_avg')
```

Tachometer Data Conditioning Code

```
%% DATA CONDITIONING CODE (data_conditioning.m)

close all
clear all
clc

% Transform the original tachometer data to a TTL-like signal
for i = 1:5
    temp = data_save(i,:);
    for j = 1:length(temp)
        if (temp(j) < -1.28)
            temp(j) = 0;
        else
            temp(j) = 5;
        end
    end

    figure(i)
    plot(time_save(i,:),temp)

    % Use nnz() and diff() to find pulse locations
    pulses(i) = nnz(diff(temp(:)>1)>0);
end

% Set time duration to frequency calculations
duration = 2;
```

```
% Find statistical information about the pulses
minimum = min(pulses);
maximum = max(pulses);
average = mean(pulses);

% Calculate RPMs from pulse information
RPM_min1 = ((minimum/duration)/3)*60;
RPM_max1 = ((maximum/duration)/3)*60;
RPM_avg1 = ((average/duration)/3)*60;

% Print information to the workspace
fprintf('Minimum RPM: %.1f\n', RPM_min1);
fprintf('Average RPM: %.1f\n', RPM_avg1);
fprintf('Maximum RPM: %.1f\n', RPM_max1);
```

Data Plotting Code

```
%% DATA PLOTTING CODE (data_plot.m)

clear all
close all
clc

% Plot wind tunnel characterization data (power fit)
figure
load('wind_tunnel_characterization.mat');
errorbar(separation,speed,E,'*');
hold on
x = linspace(min(separation),max(separation));
a = 31.69;
b = -0.4812;
plot(x,a.*x.^b,'--r');
xlabel('Opening separation (in)')
ylabel('Wind speed (m/s)')
legend('Wind tunnel data','Best fit line','Location','best')

print -depsc tunnel_characterization_power.eps

% Plot wind tunnel characterization data (rational fit)
figure
load('wind_tunnel_characterization.mat');
errorbar(separation,speed,E,'*');
hold on
x = linspace(min(separation),max(separation));
```

```
p1 = 97.8;
q1 = 1.901;
plot(x,p1./(x+q1),'--r');
xlabel('Opening separation (in)')
ylabel('Wind speed (m/s)')
legend('Wind tunnel data','Best fit line','Location','best')

print -depsc tunnel_characterization_rational.eps

% Plot theta = 10 data (linear polynomial fit)
clear all
figure
load('theta_10_data.mat')
errorbar(Vw,Wavg,Wavg-Wmin,Wmax-Wavg,'*');
hold on
x = linspace(min(Vw),max(Vw));
p1 = 76.89;
p2 = -267.2;
plot(x,p1.*x+p2,'--r')
xlabel('Wind speed (m/s)')
ylabel('Rotor RPM')
legend('Rotor RPM','Best fit line','Location','best')

print -depsc theta_10_data.eps

% Plot theta = 20 data
clear all
figure
load('theta_20_data.mat')
errorbar(Vw,Wavg,Wavg-Wmin,Wmax-Wavg,'*');
hold on
```

```
x = linspace(min(Vw),max(Vw));
p1 = 175.4;
p2 = -234.1;
plot(x,p1.*x+p2,'--r')
xlabel('Wind speed (m/s)')
ylabel('Rotor RPM')
legend('Rotor RPM','Best fit line','Location','best')

print -depsc theta_20_data.eps

% Plot theta = 30 data
clear all
figure
load('theta_30_data.mat')
errorbar(Vw,Wavg,Wavg-Wmin,Wmax-Wavg,'*');
hold on
x = linspace(min(Vw),max(Vw));
p1 = 322.8;
p2 = -502.5;
plot(x,p1.*x+p2,'--r')
xlabel('Wind speed (m/s)')
ylabel('Rotor RPM')
legend('Rotor RPM','Best fit line','Location','best')

print -depsc theta_30_data.eps

% Plot theta = 40 data
clear all
figure
load('theta_40_data.mat')
errorbar(Vw,Wavg,Wavg-Wmin,Wmax-Wavg,'*');
```

```
hold on
x = linspace(min(Vw),max(Vw));
p1 = 450.6;
p2 = -901.5;
plot(x,p1.*x+p2,'--r')
xlabel('Wind speed (m/s)')
ylabel('Rotor RPM')
legend('Rotor RPM','Best fit line','Location','best')

print -depsc theta_40_data.eps
```

RPM Surface Fitting Code

```
%% RPM DATA SURFACE FITTING CODE (RPM_surface_fit.m)

close all
clear all
clc

% Define a matrix containing all the fitted RPM data
% This data is obtained by evaluating the linear fit functions
% x = [10:10:40] (range of theta)
% y = [0:1:20] (range of Vw)
z = [-267.2 -234.1  -502.5  -901.5;
-190.31 -58.7   -179.7  -450.9;
-113.42 116.7   143.1   -0.3;
-36.53  292.1   465.9   450.3;
40.36   467.5   788.7   900.9;
117.25  642.9   1111.5  1351.5;
194.14  818.3   1434.3  1802.1;
271.03  993.7   1757.1  2252.7;
347.92  1169.1  2079.9  2703.3;
424.81  1344.5  2402.7  3153.9;
501.7   1519.9  2725.5  3604.5;
578.59  1695.3  3048.3  4055.1;
655.48  1870.7  3371.1  4505.7;
732.37  2046.1  3693.9  4956.3;
809.26  2221.5  4016.7  5406.9;
886.15  2396.9  4339.5  5857.5;
963.04  2572.3  4662.3  6308.1;
```

```
1039.93 2747.7  4985.1  6758.7;
1116.82 2923.1  5307.9  7209.3;
1193.71 3098.5  5630.7  7659.9;
1270.6  3273.9  5953.5  8110.5];

% Prepare the data for the fit() function
% Data must be in <nx1> vector format
[J,I] = size(z);

Xout = [];
Yout = [];
Zout = [];

counter = 1;

for i = 1:I
    for j = 1:J
        Xout(counter) = 10*i;
        Yout(counter) = j-1;
        Zout(counter) = z(j,i);
        counter = counter + 1;
    end
end

x = Xout';
y = Yout';
z = Zout';

% Use the fit() command to fit a polynomial surface using the 'polynm' fit
% n = 2 (order of fit in theta)
% m = 1 (order of fit in Vw)
```

```
[sf,gof] = fit([x,y],z,'poly21');

% Plot the original data and the fitted surface
plot(sf,[x,y],z)
xlabel('\theta (degrees)')
ylabel('V_w (m/s)')
zlabel('Rotor RPM')
```

Thrust Determination Code

```
% THRUST DETERMINATION CODE (thrust_determination.m)

clear
clc

% Read in data
Data = csvread('Required autorotation angle.csv',0,0,[0 0 12 2]);

% Redistribute the values from "Data" into separate variables
WindSpeed = Data(:,1);
Theta = Data(:,2);

% Mass of the rotor
m = 23/1000;
% Gravitational Constant
g = 9.81;

% Calculate the THRUST and display the results
for i = 1:length(Theta)
    Thrust(i) = (m*g)/sind(90-Theta(i));

    % Determine Lift and Drag from the value obtained for Thrust
    Lift(i) = Thrust(i)*cosd(Theta(i));
    Drag(i) = Thrust(i)*cosd(90-Theta(i));
    LTDR(i) = Lift(i)/Drag(i);

    fprintf('For theta = %f \n', Theta(i));
```

```
    fprintf('     Thrust = %f', Thrust(i));
    fprintf('     Lift = %f', Lift(i));
    fprintf('     Drag = %f', Drag(i));
    fprintf('     Lift to Drag Ratio = %f \n', LTDR(i));
end

% Plot the results
subplot(4,1,1);
plot(Theta,Thrust,'-*')
xlabel('\theta');
ylabel('Thrust (N)');

subplot(4,1,2);
plot(Theta,Lift,'-*')
xlabel('\theta');
ylabel('F_L (N)');

subplot(4,1,3);
plot(Theta,Drag,'-*')
xlabel('\theta');
ylabel('F_D (N)');

subplot(4,1,4);
plot(Theta,LTDR,'-*')
xlabel('\theta');
ylabel('F_L/F_D');

print -depsc 'ThrustLiftDrag.eps';
```

Contents of 'Required autorotation angle.csv'

Table A.1:

Separation	$\mathbf{V_w}$	θ
9.125	8.870	13.3
8.9375	9.023	12.3
8.375	9.517	9.6
8	9.878	8.2
7	10.988	6.7
6.5	11.641	5.6
6	12.378	4.9
5.5	13.214	4.5
5	14.172	4.2
4.4375	15.430	4.0
4	16.573	3.2
3.8125	17.117	2.4
3.375	18.537	1.5

APPENDIX B: NOMENCLATURE

Tethered Airfoil Nomenclature

Symbol	Units	Description
m_k	kg	Mass of the airfoil
l_t, m_t	m, kg	Length and mass of the tether, respectively
l_e, m_e	m, kg	Length and mass of each tether element, respectively
ϕ_k	rad	Inclination of the airfoil with the horizontal
ϕ_i	rad	Inclination of the i^{th} tether element with the horizontal
y_n, z_n		y and z position coordinates of n^{th} tether element, respectively
$U_{\infty,i}$	$m \cdot s^{-1}$	Free stream air velocity component in i-direction
$U_{rel,i}$	$m \cdot s^{-1}$	Relative wind velocity in i-direction
L, D	N	Lift and drag forces acting on the airfoil
F_c	N	Force of tether on the airfoil
ρ	$kg \cdot m^{-3}$	Free stream air density
C_L, C_D		Coefficients of lift and drag, respectively
A	m^2	Airfoil area
α	rad	Angle of attack
$\alpha_{L,0}$	rad	Angle of attack for zero lift
ϵ		Span effectiveness factor
AR		Aspect ratio
b, s	m, m^2	Wing span and wing area, respectively
C_d		Profile drag coefficient
T, V	J	Kinetic and potential energy of the system
$\mathcal{L}$		Lagrangian
W		Virtual work done by external non-potential forces and torques

Symbol	Units	Description
τ_i		Generalized force corresponding to generalized coordinate ϕ_i
τ_k		Generalized force corresponding to generalized coordinate ϕ_k
y_c, z_c		Coordinates of the center of mass of the airfoil
y_0		Position of base
F_b		Generalized force corresponding to generalized coordinate y_0
I_O	$kg \cdot m^2$	Moment of inertia for straight tether case
M_a	$N \cdot m$	Torque due to offset of L and D from mass center
F_a	N	Actuation force for changing airfoil inclination
d	m	Distance of actuation force from airfoil center
$_e$		(subscript) Values at equilibrium

Autogyro Nomenclature

Symbol	Units	Description
B		Number of blades
c	m	Blade chord
H	N	Longitudinal force
k_L, k_D		Lift and drag coefficients of a blade element
Q	$N \cdot m$	Aerodynamic torque
R	m	Blade radius
T	N	Thrust force
V	$m \cdot s^{-1}$	Velocity of the aircraft or wind
W	N	Total system weight
X	N	Effective drag force
Y	N	Lateral force
Z	N	Effective lift force
α	rad	Blade pitch angle
β	$rad \cdot s^{-1}$	Angular rotation of blade about hinge
β_0, β_1, ϕ_1		Fourier series parameters of flapping motion
θ	rad	Angle of incidence of the autogyro rotor
λ		Tip speed ratio
μ		Axial flow ratio
ρ	$kg \cdot m^{-3}$	Density of air
σ		Blade solidity
ψ	rad	Angular position of blade
Ω	$rad \cdot s^{-1}$	Angular velocity of rotor about its shaft

LIST OF REFERENCES

[1] Charles K. Alexander and Matthew N. O. Sadiku. *Fundamentals of Electric Circuits*. McGraw-Hill, 5th edition, 2012.

[2] J. D. Anderson Jr. *Fundamentals of Aerodynamics*. McGraw-Hill, 2010.

[3] J. D. Anderson Jr. *Introduction to Flight*. McGraw-Hill, 2011.

[4] C. L. Archer and K. Caldiera. Global assessment of high-altitude wind power. In *Energies*, volume 2, pages 307–319, 2009.

[5] M. Canale, L. Fagiano, and M. Milanese. High altitude wind energy generation using controlled power kites. *IEEE Transactions on Control Systems Technology*, 18 (2):279–293, 2010.

[6] B. H. Charnov. *From Autogyro to Gyroplane: The Amazing Survival of an Aviation Technology*. Praeger Publishers, 2003.

[7] T. Das, R. Mukherjee, , R. Sridhar, and A. Hellum. Two dimensional modeling and simulation of a tethered airfoil system for harnessing wind energy. *ASME Dynamic Systems and Control Conference*, 2011.

[8] Tuhin Das, Ranjan Mukherjee, Rahulram Sridhar, and A. Hellum. Two-dimensional modeling and simulation of a tethered airfoil system for harnessing wind energy. In *ASME Dynamic Systems and Control Conference*, 2011.

[9] I. Durre, R. S. Vose, and D. B. Wuertz. Overview of the integrated global radiosonde archive. *Journal of Climate*, 19(1):53–68, 2006.

[10] D. Elliot, M. Schwartz, S. Haymes, D. Heimiller, G. Scott, M. Brower, E. Hale, and B. Phelps. New wind energy resource potential estimates for the united states. Technical Report NREL Report No. PR-5500-50439, National Renewable Energy Laboratory, 2011.

[11] Arie Feuer and Graham Goodwin. *Sampling in Digital Signal Processing and Control*. Systems and Control: Foundations and Applications. Birkhauser Boston, 1 edition, 1996.

[12] C. A. J. Fletcher. On the rotary wing concept for jet stream electricity generation. In *Journal of Energy*, 1979.

[13] Robert W. Fox, Philip J. Pritchart, and Alan T. McDonald. *Introduction to Fluid Mechanics*. Wiley, 7 edition, 2008.

[14] M. Garcia-Sanz and C. H. Houpis. *Wind Energy Systems: Control Engineering Design*. CRC Press, 2012.

[15] A. Gessow and G. C. Myers. *Aerodynamics of the Helicopter*. Macmillan Company, 1952.

[16] Alfred Gessow and Almer D. Crim. An extension of lifting rotor theory to cover operation at large angles of attack and high inflow conditions. Technical report, National Advisory Committee for Aeronautics, 1952.

[17] H. Glauert. A general theory of the autogyro. Technical report, Aeronautical Research Council, 1926.

[18] B. K. Hodge. *Alternative Energy Systems and Applications*. John Wiley & Sons, Inc., 2009.

[19] Dewey H. Hodges and G. Alvin Pierce. *Introduction to Structural Dynamics and Aeroelasticity*. Cambridge Aerospace Series (Book 15). Cambridge University Press, 2011.

[20] William J. Palm III. *System Dynamics*. McGraw Hill, 2 edition, 2010.

[21] The MathWorks Inc. diff - differences and approximate derivatives.

[22] The MathWorks Inc. nnz - number of nonzero matrix elements.

[23] National Instruments. Low-cost, bus-powered multifunction daq for usb.

[24] Eastman N. Jacobs and William C. Clay. Characteristics of the n.a.c.a 23012 airfoil from tests in the full-scale and variable-density tunnels. Technical Report 530, National Advisory Committee for Aeronautics, 1936.

[25] C. N. H. Lock. Further development of autogyro theory, part i. Technical report, Aeronautical Research Council, 1927.

[26] M.L. Loyd. Crosswind kite power. *Journal of Energy*, 4 (3):106–111, 1980.

[27] M. S. Manalis. Airborne windmills: Energy source for communication aerostats. In *AIAA Lighter Than Air Technology Conference*, 1975.

[28] M.S. Manalis. Airborne windmills and communication aerostats. *Journal of Aircraft*, 13(7):543–544, 1976.

[29] L. Meirovitch. *Methods of Analytical Dynamics*. McGraw-Hill, 1970.

[30] W. J. Ockels. Laddermill, a novel concept to exploit the energy in the airspace. In *Aircraft Design*, 2001.

[31] W.J. Ockels. Laddermill, a novel concept to exploit the energy in the airspace. *Aircraft Design*, 4(81-97), 2001.

[32] U.S Department of Energy. Caithness shepherds flat. *Loan Programs Office*, 2010.

[33] EGG Optoelectronics. Typical applications for phototransistors and ireds.

[34] CleanEnergy Action Project. Alta wind energy center. *Fundamentals of Renewable Energy Case Study in Wind Power*, August 2013.

[35] CleanEnergy Action Project. Roscoe wind complex. *Fundamentals of Renewable Energy Case Study in Wind Power*, 2013.

[36] Sigitas Rimkus and Tuhin Das. An application of the autogyro theory to airborne wind energy extraction. In *ASME Dynamic Systems and Control Conference*, 2013.

[37] Sigitas Rimkus, Tuhin Das, and Ranjan Mukherjee. Stability analysis of a tethered airfoil. In *American Controls Conference*, 2013.

[38] B. W. Roberts, D. H. Shepard, K. Caldiera, M. E. Cannon, D. G. Eccles, A. J. Grenier, and J. F. Freidin. Harnessing high-altitude wind power. In *IEEE Transactions on Energy Conversion*, volume 22, pages 136–144, 2007.

[39] Fairchild Semiconductor. Design fundamentals for phototransistor circuits.

[40] John B. Wheatley. An aerodynamic analysis of the autogiro rotor with a comparison between calculated and experimental results. 487, National Advisory Committee for Aeronautics, 1934.

[41] John B. Wheatley. The aerodynamic analysis of the gyroplane rotating-wing system. Technical Report 492, National Advisory Committee for Aeronautics, 1934.

[42] John B. Wheatley. An analytical and experimental study of the effect of periodic blade twist on the thrust, torque, and flapping motion of an autogyro rotor. Technical Report 591, National Advisory Committee for Aeronautics, 1937.

[43] F.M. White. *Fluid Mechanics*. McGraw-Hill, 2002.

[44] P. Willams, B. Lansdorp, and W. Ockels. Optimal cross-wind towing and power generation with tethered kites. *AIAA Journal of Guidance, Control and Dynamics*, 31, 2008.

[45] P. Williams, B. Lansdorp, and W. J. Ockels. Modeling and control of a kite on a variable length inelastic tether. In *AIAA Modeling and Simulation Technologies Conference and Exhibit*, 2007.

[46] P. Williams, B. Lansdorp, and W. J. Ockels. Nonlinear control and estimation of a tethered kite in changing wind conditions. In *AIAA Journal of Guidance, Control, and Dynamics*, 2008.

[47] P. Williams, B. Lansdorp, and W. J. Ockels. Optimal cross-wind towing and power generation with tethered kites. In *AIAA Journal of Guidance, Control, and Dynamics*, 2008.

[48] www.airfoildb.com. Naca 23012.

[49] www.airfoiltools.com. Naca 23012 airfoil.